Universiteit Leiden
The Netherlands

Spin-triplet supercurrents of odd and even parity in nanostructured devices

Lahabi, K.

Citation
Lahabi, K. (2018, December 4). *Spin-triplet supercurrents of odd and even parity in nanostructured devices*. *Casimir PhD Series*. Retrieved from https://hdl.handle.net/1887/68031

Version:	Not Applicable (or Unknown)
License:	Licence agreement concerning inclusion of doctoral thesis in the Institutional Repository of the University of Leiden
Downloaded from:	https://hdl.handle.net/1887/68031

Note: To cite this publication please use the final published version (if applicable).

Cover Page

Universiteit Leiden

Leiden University Repository

The handle http://hdl.handle.net/1887/68031 holds various files of this Leiden University dissertation.

Author: Lahabi, K.
Title: Spin-triplet supercurrents of odd and even parity in nanostructured devices
Issue Date: 2018-12-04

SPIN-TRIPLET SUPERCURRENTS OF ODD AND EVEN PARITY IN NANOSTRUCTURED DEVICES

Proefschrift

ter verkrijging van
de graad van Doctor aan de Universiteit Leiden,
op gezag van Rector Magnificus prof.mr. C.J.J.M. Stolker,
volgens besluit van het College voor Promoties
te verdedigen op dinsdag 4 december 2018
klokke 11.15 uur

door

Kaveh Lahabi
Geboren te Shiraz, Iran, 1987

Promoter:

Prof. dr. J. Aarts	Universiteit Leiden

Promotiecommissie:

Prof. dr. ir. A. Brinkman	Universiteit Twente
Prof. dr. M. Eschrig	Royal Holloway, University of London
Prof. dr. Y. Maeno	Kyoto University
Prof. dr. E. R. Eliel	Universiteit Leiden
Prof. dr. ir. T. H. Oosterkamp	Universiteit Leiden

Casimir PhD series, Delft-Leiden 2018-45
ISBN 978-90-8593-375-5

An electronic version of this thesis can be found at
https://openaccess.leidenuniv.nl/.

Cover design: Kaveh Lahabi
Copyright © 2018 Kaveh Lahabi

About the cover: Supercurrents have a wave-like nature, similar to that of light. The cover shows an artistic impression of this while also making reference to our superconducting devices, the disk-shaped Josephson junction and the ring.

Contents

1 Introduction **3**
References . . . 9

2 Pairing symmetry **11**
2.1 General symmetry classes . . . 11
2.2 Pairing symmetry of Sr_2RuO_4 . . . 15
2.2.1 Sr_2RuO_4: basic properties . . . 15
2.2.2 d-vector formalism . . . 17
2.2.3 Possible symmetries for Sr_2RuO_4 . . . 20
References . . . 25

3 Spin-triplet Cooper pairs in magnetic hybrids **29**
3.1 Proximity Effect . . . 29
3.1.1 Spin-active interfaces . . . 31
3.1.2 Long-range triplet correlations . . . 33
3.1.3 Josephson effect . . . 35
3.1.4 Long-range triplet supercurrents . . . 37
3.2 Micromagnetic Simulations . . . 41
3.2.1 Micromagnetic Theory . . . 41
3.2.2 Simulations . . . 42
3.2.3 Multilayer Planar Junctions . . . 44
3.3 CrO_2 nanowires . . . 47
3.3.1 magnetic patterns . . . 47
3.3.2 Generating long-range triplets with magnetic pattern . . . 51
References . . . 53

4 Controlling the path of spin-triplet currents in a magnetic multilayer **59**
4.1 Introduction . . . 60
4.2 Results . . . 61
4.2.1 Micromagnetic simulations . . . 61
4.2.2 Supercurrent calculations . . . 62

4.2.3 Basic transport properties 63
4.2.4 Superconducting quantum interferometry. 63
4.2.5 Magnetotransport with in-plane fields 66
4.3 Discussion 68
4.4 Methods 69
4.4.1 Device fabrication 69
4.4.2 Magnetotransport measurements 69
4.4.3 Micromagnetic simulations 70
4.4.4 Control experiment 70
4.5 Supplementary Information 71
4.5.1 Supplementary Figures 71
4.5.2 Supplementary Note 1: Transport in the virgin state 74
4.5.3 Supplementary Note 2: Numerical simulations of the critical current 74
4.5.4 Supplementary Note 3: Fourier analysis of supercurrent density profiles. 76
References 77

5 Generating Spin-Triplet Supercurrents with a Ferromagnetic Vortex 81
5.1 Motivation 82
5.1.1 Formation of 0-π triplet channels: S/F'/F/F"/S 82
5.2 Generating spin-triplet supercurrents with a ferromagnetic vortex . . . 86
5.2.1 Basic transport and ground state interference 86
5.2.2 Magnetotransport with in-plane fields 87
5.2.3 Emergence of 0 & π channels in the vortex 89
5.2.4 Interference patterns from a displaced vortex 89
5.2.5 Summary & Outlook 93
References 95

6 Little-Parks effect and half-quantum fluxoid in Sr_2RuO_4 microrings 97
6.1 Introduction 98
6.2 Results and Discussion 101
References 106

7 Spontaneous emergence of Josephson junctions in Sr_2RuO_4 111
7.1 General Introduction 112
7.2 Introduction 114

7.3 Results 115
7.3.1 Basic transport properties 115
7.3.2 Insights from order parameter simulations 116
7.3.3 Critical current oscillations 118
7.3.4 Rings with an extrinsic phase & T_c oscillations 120
7.3.5 Anomalous current-voltage & in-plane fields 124
7.4 Discussion 126
7.4.1 Mechanisms for oscillatory $I_c(H)$ 126
7.4.2 Josephson energy of a chiral domain wall 128
7.5 Summary & Outlook 134
7.6 Supplementary Figures 135
References 137

Summary **141**

Samenvatting **145**

Acknowledgements **149**

List of Publications **151**

Curriculum Vitae **153**

1

INTRODUCTION

CONVENTIONAL ELECTRONICS relies on the motion of individual electrons in a conducting material. This type of charge transport is characterised by electron scattering, a dissipative process which results in finite electrical resistance. Good conductors such as gold or silver are characterized by fewer scattering events, and therefore smaller resistance. But what about superconductors? These are electronic systems with exactly zero electrical resistance below a critical temperature (T_c). This is however not the only (or the most profound) distinguishing quality of superconductors, compared to other electronic systems (e.g. normal metals or semiconductors), superconductors follow a fundamentally different set of rules. In fact, one can argue that in some respects superconductors have more in common with the vegetable cauliflower than they do with a good conductor like gold.

Elementary particles can be classified into two main categories based on their intrinsic angular momentum, or "spin". Those with half-integer spins ($1/2, 3/2$, etc.) are called Fermions while the ones with integer spins ($0, 1, 2$, etc.) are known as Bosons. The difference between these two classes however does not end with spin, they also follow entirely different distributions. In a system of fermions, each particle acts as an individual object with a unique quantum state which, in principle, can be distinguished from the rest[1]. In contrast, an indefinite number of bosons can share a single quantum state, and form a "condensate" of indistinguishable particles.

[1] In practice however, this can only be realised if there are a finite number of discrete states.

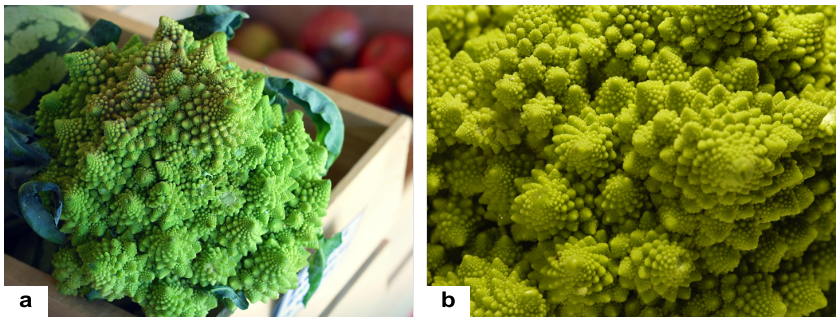

Figure 1.1: The Roman cauliflower (Romanesco). Without the help of the items in the background in **a**, it is practically impossible to guess the actual length scale in **b**. The self-similar construction of the buds makes their actual size irrelevant.

Superconductivity occurs by the condensation of pairs of electrons into a macroscopic quantum state. The paired electrons are called Cooper pairs[2] and, unlike electrons, which are spin 1/2 fermions, they are Bosonic in nature. This means that all paired electrons can share a single quantum state. As an interesting consequence, the wavefunction of a pair of electrons (referred to as the order parameter) can now elegantly describe the entire superconducting condensate, and vice versa. In this sense, a superconductor is rather analogous to the Romanesco cauliflower (shown in Figure 1.1), where the structure of each bud is indistinguishable from the ones it is made of.

In Figure 1.1 **a**, the Romanesco head is shown together with a number of other objects, while in Figure 1.1 **b** the buds appear by themselves. What is stricking here is that the lack of reference objects has made it almost impossible to guess the actual length scale in **b**. One way to interpret this is that (at least to a large extent) the size of the system has lost its significance. If the sole function of a photograph is to help us identify objects, in the case of Romaneso the image can cover anywhere between a few microns to a few metres; and still produce the same result. This reasoning can also be applied to superconductivity, which is a macroscopic quantum phenomenon. In almost all other physical systems, the individual quantum states begin to smear out by increasing the number of interacting particles. As a result, all the intriguing aspects of quantum mechanics are typically observed in systems with no more than a few atoms. Superconductors and superfluids on the other hand, do not suffer this drawback, making them ideal platforms for exploring various quantum phenomena.

In analogy to Figure 1.1, whether we probe a single Cooper pair or a macroscopic

[2] named after Leon Cooper who developed the first microscopic theory of superconductivity with John Bardeen and John Robert Schrieffer (the BCS theory) in 1957 [1].

superconductor, there is only one order parameter with the same set of quantum characteristics. This however does not imply that the size of a superconducting system has no significance. Quite the contrary, as we will discuss throughout this thesis, mesoscopic systems can offer considerably better control over superconductivity, and are far more practical for device applications. Apart from their technological implications, mesoscopic systems can also be used to identify, and in certain cases even create, some of the rarest and most exotic quantum states in nature. Such insights are crucial to our understanding of the mechanisms involved in some of the most controversial phenomena of modern Physics.

The behaviour of any quantum system is determined by its wavefunction. In superconductors, this corresponds to the pairing function of the electrons that form the Cooper pair. A superconductor can therefore be characterized by the type of symmetry that describes its pairing function. It is well established by the exclusion principle that fermions, such as electrons, can only be paired with each other if their combined wavefunction is antisymmetric i.e. can be represented by an *odd function* $f(-x) = -f(x)$. One way to satisfy this condition would be if the pairing occurred between electrons with opposite spins.This turns out to be the case in the overwhelming majority of all currently known superconductors (and superfluids). There is however no reason for this to be the only stable configuration. Cooper pairs can also form by electrons of equal spin.

Besides spin, a wavefunction has two other components that determine its pairing symmetry. These are space and time which, for practical reasons, are commonly represented in the form of momentum and frequency, respectively. Equal-spin pairing is allowed, as long as one of the two other components (but not both) corresponds to an odd function. The phenomenon is known as triplet superconductivity, and is the main subject of this thesis. There are two general categories of triplet superconductors based on their pairing symmetry: odd-momentum with even-frequency, and even-momentum with odd-frequency. It appears that both categories are extremely rare in nature. At present, we know only a handful of materials with odd-momentum triplet pairing, and odd-frequency triplet correlations have only been "generated" in carefully engineered superconductor-ferromagnet (S-F) hybrid systems. On the other hand, triplet Cooper pairs have become an ingredient in a multitude of newly emerging fields of condensed matter physics, with a growing number of applications in quantum computing, spintronics and superconducting electronics. This calls for a deeper understanding of the physics behind triplet superconductivity, and developing the means for its control so it can be utilized in upcoming device applications.

The research presented in this thesis extends into both categories of triplet superconductors. This involves both implementing S-F hybrids as the platform to explore odd-frequency triplet correlations, and investigating the unusual characteristics of strontium ruthenate Sr_2RuO_4, a leading candidate for odd-momentum triplet pair-

ing. In each case we use *mesoscopic structures* as the principal tool to gain new insights into some of the most subtle and yet distinct characteristics of triplets, which otherwise would be very challenging to observe. Moreover, combining well-defined geometries with the substantial role of confinement in defining the free energy of a system makes mesoscopic structures the means to not merely observe, but gain effective control over the unique aspects of triplet pairing.

In S-F hybrids we control the odd-frequency triplet correlations by utilizing the shape of the ferromagnet to create a well-defined micromagnetic configuration. As triplet correlations are highly sensitive to the spin-texture the ferromagnet (or rather the exchange field gradient), micromagnetics can provide the means to control their amplitude, phase and even the location of their current path in the ferromagnet. The potential of such degree of control over superconductivity, and its implications in superconducting electronics are profound. A notable example of this is presented here in the form of a possible new type of non-volatile superconducting memory element, developed by combining the unique characteristics of triplet correlations with the controllable micromagnetic configuration of a disk-shaped Josephson junction.

As for Sr_2RuO_4, there are two main aspects to the use of mesoscopic structures in our studies. The first is related to the observation of an unusual state known as the half-quantum vortex (HQV). In the context of Sr_2RuO_4, the HQV is a result of equal-spin triplet pairing, and is also expected to be a host to the highly sought-after Majorana zero-modes[3] [3]. Unlike the ordinary (full-quantum) vortex, the HQV is accompanied by a spin current whose free energy grows logarithmically with the dimensions of system. Consequently, the HQV states become energetically less favourable, and unlikely to stabilise in macroscopic (bulk) systems. One solution to this is to reduce the size of the system; so that the spin current associated with the HQV can be contained within the geometrical boundaries of the system which, in our case is a micron-sized ring and is designed for field-dependent transport measurements.

Interestingly however, the significance of mesoscopic structures for Sr_2RuO_4 goes well beyond the HQV. Unlike the ordinary superconductor, which is described by a single macroscopic quantum state, Sr_2RuO_4 is expected to have a twofold degenerate ground state; with different directions of orbital angular momentum for the condensate [4]. This breaking of time-reversal symmetry is associated with the so-called "chiral" superconducting states. Here, chirality refers to the direction-dependent phase of the superconducting order parameter. As the orbital phase can either wind clockwise or anticlockwise, there are two distinct chiral states (e.g. left or right) available to the order parameter. An interesting consequence of these degenerate

[3] also referred to as Majorana Fermions: a class of particles which, unlike protons and electrons, are their own antiparticles. While evidently rare in nature, in the past two decades Majorana Fermions have enjoyed substantial popularity for their potential in fault-tolerant quantum computing. More details on the topic can be found in [2].

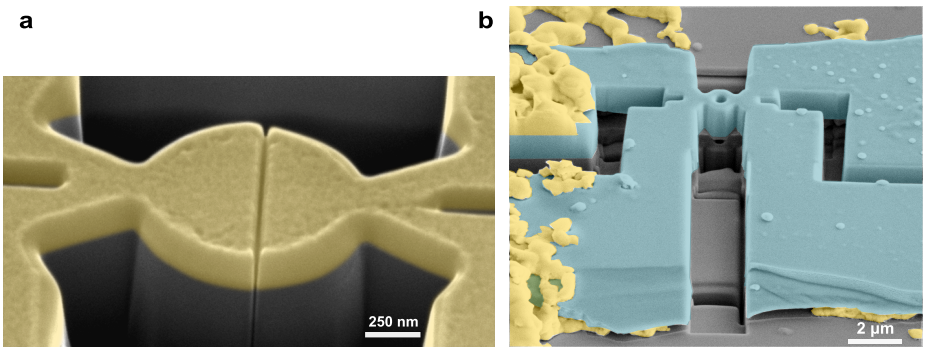

Figure 1.2: Examples of FIB milling used for structuring of the different systems discussed in this thesis (false coloured electron microscope images) . **a** Disk-shaped Josephson junction, structured from a multilayer of Co/Cu/Ni/Nb. The junction is formed by the central trench. The gap is less than 20 nm wide, and cuts the top superconducting Cu/Ni/Nb layers in two halves — leaving only Co as a ferromagnetic barrier connecting them. **b**, a mesoscopic ring structured by milling a single Sr_2RuO_4 crystal (cyan), residing on a $SrTiO_3$ substrate, which is contacted by silver epoxy (gold) for electrical transport measurements.

ground states is the emergence of chiral superconducting domains, where the two chiral states are segregated in real space. Despite numerous efforts over the past two decades, a direct observation of such domains is still lacking. The vast majority of these experiments have been limited to bulk crystals of Sr_2RuO_4, typically hundreds of microns in dimension. This is partly due to the absence of thin superconducting Sr_2RuO_4 films. The domains are expected to be no more than a few microns in size [5]. Moreover, while the domains are expected to be pinned to random defects in the crystal, they also appear to be easily displaced under the influence of an applied current or magnetic field [6]. The arbitrary configuration of the domains in bulk systems introduces an element of uncertainty, which can be problematic when probing the local order parameter to demonstrate the spatial segregation of chiral states. This is where mesoscopic structures can provide a solution. It is known that the energy cost associated with a chiral domain wall, grows per area [7]. Hence, a domain wall would favour the most constricted parts of a given structure to reduce its energy. The situation is somewhat analogous to the magnetic domains inside a ferromagnet, where geometrical restrictions (e.g. a notch in a ferromagnetic wire), can be used as an effective mechanism for pinning the domain walls by lowering the free energy. This is a widely popular practice in spintronics and novel magnetic memory devices. This concept however has not been explored in the context of superconducting domains. This can partly be attributed to the material properties of Sr_2RuO_4, which put severe constraints on the fabrication of mesoscopic structures. This is also reflected in the fact that, while there have been a substantial number of experiments on Sr_2RuO_4 for over two decades, no more than a handful have examined mesoscopic structures.

This lack of studies on microstructures is not unique to Sr_2RuO_4. There is a growing family of exotic correlated electron systems which suffer the same drawback, as they can currently be prepared only as bulk-like crystals, due to their sensitivity to disorder. Many of these materials have highly unconventional magnetic and transport properties, which currently cannot be described by any existing theory. Understanding the mechanisms behind such correlated electron systems is one of the principal challenges of modern condensed matter physics. Here, we tackle this issue by utilizing a Ga^+ focused ion beam (FIB) to prepare mesoscopic structures out of bulk crystals of Sr_2RuO_4. The method can be described as "sculpting" the desired structure by shooting ions at a target to sputter away (or mill) the surrounding material. This provides a highly precise and versatile nanostructuring technique, and is implemented as the principal fabrication method throughout this work. In case of S-F devices, the use of exceptionally small ion currents (down to 1 pA) together with the spot-size of a carefully focused beam provided the means to obtain well-defined nanostructures, with the smallest features reaching below 20 nm (shown in Figure 1.2 **a**). As for Sr_2RuO_4, FIB enables us to cut through crystals that otherwise would be too thick to structure using conventional lithography and etching techniques (Figure 1.2 **b**). Furthermore, the arbitrary shape and dimensions of a crystal could carefully be accounted for while the milling took place. This allowed for precise adjustments to the sample design based on the unique structure of individual crystals.

OUTLINE OF THE THESIS

- **Chapter 2** (*Pairing symmetry*) begins with the general symmetry classes for Cooper pairs, with an emphasis on spin-triplet pairing. The discussion is then directed towards Sr_2RuO_4. By introducing the d-vector formalism, this chapter continues to describe possible pairing symmetries for Sr_2RuO_4. The likelihood of each case is evaluated as we review a number of key experiments.

- **Chapter 3** (*Triplet Cooper pairs in magnetic hybrids*) is related to odd-frequency (even-parity) triplet correlations. The first section introduces the concept of long-range proximity effect, and addresses the challenges in utilising it in functional devices. The next section describes how we tackle these issues with the use of micromagnetic simulations. An example of this is provided in the last section, where we describe the magnetic patterns of CrO_2 nanowires, which we then implement to generate long-range triplet currents.

- **Chapter 4** (*Controlling supercurrent and their spatial distribution in ferromagnets*) demonstrates how micromagnetic simulations can be used to control the path of spin-triplet supercurrents in a magnetic multilayer. This is realised in a disk-shaped planar Josephson junction with a Ni/Co/Ni barrier, where Co and Ni layers can have non-collinear magnetizations.

- **Chapter 5** (*Generating spin-triplet supercurrents with a ferromagnetic vortex*). Here we show that the magnetic pattern of a *single* ferromagnet can be implemented to generate and control long-range triplet currents. We also examine the *phase* of the triplet channels formed by a ferromagnetic vortex, and show that displacing the vortex core can produce widely different transport behaviours in the same device.

- **Chapter 6** (*Little-Parks oscillations with half-quantum fluxoid features in Sr_2RuO_4 micro rings*) is concerned with the half-quantum vortex in Sr_2RuO_4, and its possible signatures in magnetotransport measurements.

- **Chapter 7** (*Spontaneous emergence of Josephson junctions in single-crystal Sr_2RuO_4*) focuses on the behaviour of a *single* chiral domain wall, which is predicted to act as an unconventional Josephson junction. We investigate this using mesoscopic rings, structured entirely out of a single Sr_2RuO_4 crystal. Order parameter simulations predict a domain wall to cross the arms of the ring, forming a pair of parallel Josephson junctions. Our transport measurements show a clear critical current oscillation, similar to that of a DC SQUID with two symmetric junctions. This, together with a detailed analysis of current-voltage behaviour make a compelling case for the presence of a chiral domain wall.

REFERENCES

[1] J. Bardeen, L. N. Cooper, and J. R. Schrieffer. Theory of superconductivity. *Physical Review*, 108(5):1175, 1957.

[2] J. Alicea. New directions in the pursuit of Majorana fermions in solid state systems. *Reports on Progress in Physics*, 75(7):076501, 2012.

[3] N. Read and D. Green. Paired states of fermions in two dimensions with breaking of parity and time-reversal symmetries and the fractional quantum hall effect. *Physical Review B*, 61(15):10267, 2000.

[4] T. Rice and M. Sigrist. Sr_2RuO_4: an electronic analogue of ^{3}He ? *Journal of Physics: Condensed Matter*, 7(47):L643, 1995.

[5] A. Bouhon and M. Sigrist. Influence of the domain walls on the Josephson effect in Sr_2RuO_4. *New Journal of Physics*, 12(4):043031, 2010.

[6] F. Kidwingira, J. Strand, D. Van Harlingen, and Y. Maeno. Dynamical superconducting order parameter domains in Sr_2RuO_4. *Science*, 314(5803), 2006.

[7] M. Sigrist and D. F. Agterberg. The role of domain walls on the vortex creep dynamics in unconventional superconductors. *Progress of Theoretical Physics*, 102(5):965–981, 1999.

2

PAIRING SYMMETRY

2.1. GENERAL SYMMETRY CLASSES

IN A SUPERCONDUCTING MATERIAL, Cooper pairs can form at the Fermi surface by some type of weakly attractive interaction. The origin of this attractive interaction however, appears to vary for different types of superconductors. For instance, it is more or less established that in most elemental superconductors (e.g. Al, Pb and Nb) the electron-phonon coupling is responsible for the pair formation. This class of material are generally referred to as conventional or BCS superconductors, as they can be described by the BCS theory. This theory however fails to describe a growing number of so-called "unconventional" superconductors, including cuprates and heavy fermions. While the exact origin of unconventional superconductivity is currently not clear, it is however evident that the pairing mechanism is more closely related to spin fluctuations than BCS-type electron-phonon coupling. A discussion on these interactions would go well beyond the scope of this thesis. Instead, here we focus on the different types of wavefunction which, at least in principle, could allow two electrons to exist as a pair, irrespective of the underlying interactions involved.

The superconducting wavefunction is generally represented by a complex gap function Δ. This corresponds to the energy gap which develops around the Fermi surface when electrons are condensing into Cooper pairs — illustrated in Figure 2.1. Within this gap electrons are in a coherent state, and are only available as Cooper pairs. The size of the gap is a measure of the energy of a condensate, as it roughly translates to the energy required to break a pair by exciting electrons (holes) to states above

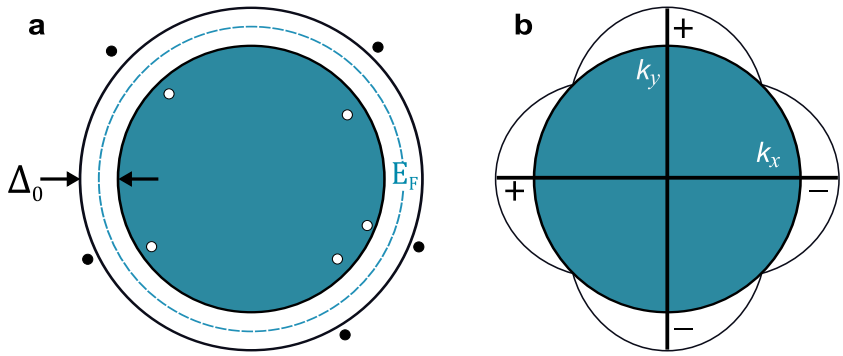

Figure 2.1: The superconducting gap. **a** Representation of a BCS superconductor. Pairing occurs within a uniform energy gap formed around the Fermi surface E_F (the shaded region represents occupied electron states). Unpaired electrons (black dots) and holes (white dots) are not allowed within the gap. They only appear as quasiparticles in the states above and below the gap. BCS superconductors are characterised by an isotropic gap Δ_0, uniform in k-space. **b** The $d_{x^2-y^2}$ gap, common amongst cuprates. The order parameter consists of four lobes with alternating phase (represented by$+/-$). This leads to an anisotropic gap which goes to zero in certain directions (here, along $k_x = \pm k_y$).

(below) the superconducting gap. It is important to remember that the gap function is essentially the wavefunction of two electrons in a paired state which, broadly speaking, behaves as a Bose particle. Nevertheless, the constituting electrons are still fermions; and therefore must preserve the anticommuting properties that follow from the Pauli exclusion principle. This, in a nutshell, means that a paired state between two fermions is only allowed if its wavefunction is antisymmetric i.e. changes sign upon exchange of particles. This condition can be satisfied in a number of ways, as there are three distinct components in the wavefunction of a pair of electrons. These are spin, space (represented by the orbital part of the wavefunction in momentum space) and time (or frequency). Each component is allowed to correspond to an odd or even function. However, the *overall* wavefunction (the product of all three) must always be odd.

Cooper pairs can be divided into two categories based on their spin symmetry: singlets (odd) and triplets (even). For the singlet $(|\uparrow\downarrow\rangle - |\downarrow\uparrow\rangle)/\sqrt{2}$, the sum of the spin angular momenta is zero ($S = 0$), while the combined spin of a triplet pair is $S = 1$. There are three distinct triplet states with different spin projections (m_s) defined with respect to the quantization axis for spin. These are $|\uparrow\uparrow\rangle$; ($m_s = 1$), $|\downarrow\downarrow\rangle$; ($m_s = -1$) and $(|\uparrow\downarrow\rangle + |\downarrow\uparrow\rangle)/\sqrt{2}$; ($m = 0$). The first two correspond to equal-spin pairing, where the electron spins are parallel to each other.

With respect to the momentum (spatial) symmetry, it is customary to implement the conventions used in describing atomic orbitals. Depending on its orbital component

(L), the symmetry of the order parameter can be approximated by the shape of the s ($L = 0$), p ($L = 1$), d ($L = 2$) and f ($L = 3$) orbitals. Superconductors with s- or d-wave gaps are momentum-symmetric (even-parity), while the p- and f-wave gaps are represented by pair functions with an antisymmetric momentum (odd-parity). A BCS superconductor is characterised by s-wave symmetry. This corresponds to an isotropic order parameter in k-space (see Figure 2.1**a**), with a uniform gap around the Fermi surface $\Delta(\mathbf{k}) = \Delta_0$ (independent of k). Cuprates on the other hand (e.g. YBCO), are mostly characterised by the d-wave order parameter $d_{x^2-y^2}$, shown in Figure 2.1**b**. Such a gap is anisotropic with respect to the Fermi sheet, and its amplitude and phase are both k-dependent. More specifically, $\Delta(\mathbf{k})$ is represented by four lobes with alternating (reversed) phase. This also results in nodes in the superconducting gap, where the parameter is suppressed along certain axes.[1]

While frequency symmetry may seem as an abstract concept, which can only be expressed in terms of the Gor'kov anomalous Green function [2] in the Matsubara representation [3], its basic idea can be readily understood by picturing the correlation between two electrons as a function of time. The restrictions of the Pauli principle are imposed to this correlation at equal *times*. This means the two electrons cannot occupy the same state at the same time. The electrons however can avoid each other through the exchange of time variables. This corresponds to a pair function with asymmetric (odd) time component. Naively, one can think of this as a form of quantum mechanical timesharing, where two electrons can occupy the same state at different times. The time component of the correlation function is conveniently represented by a Matsubara frequency ω. An order parameter has odd-frequency if $\Delta(-\omega) = -\Delta(\omega)$.

Given that the overall pairing function must be antisymmetric, we can combine the symmetries of spin, frequency and momentum components to represent the allowed pairings states; compatible with the exclusion principle and Fermi-Dirac statistics. All Cooper pairs now can be categorised into four general groups, shown in Figure 2.2. This classification scheme was formalised independently by Eschrig *et al.* [4], and by Tanaka and Golubov [5, 6] in 2007.

Spin singlet Cooper pairs can either occur with even-frequency and even-parity, or with odd-frequency and odd-parity. These correspond to the first and second categories of Figure 2.2 respectively. Remarkably, the first category alone represents the overwhelming majority of all known superconductors. This includes all BCS superconductors (s-wave) as well as high-T_c cuprates and a large number of other unconventional superconductors with d-wave symmetry.

[1] Note that in some literature a k-dependent order parameter is considered as the criterion for unconventional superconductivity (e.g. Ref [1]) This classification however tends to neglect s-wave odd-frequency triplets and signed-reversed s-wave pairing, predicted for iron pnictides, by grouping them together with conventional (BCS-like) singlets.

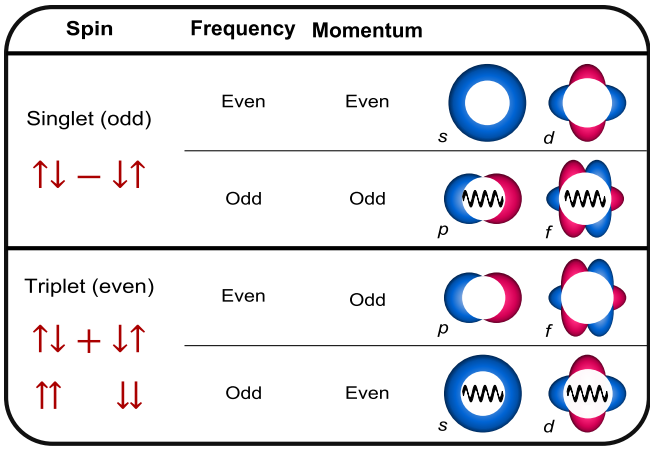

Figure 2.2: The four classes of Cooper pair symmetry, as allowed by the Pauli principle. This classification is based on three independent components which determine the overall pairing symmetry of the superconducting wavefunction: spin, frequency and momentum. The drawings in the right panel represent the allowed orbital symmetries for each category. The black wavy line represents odd frequency.

The available symmetries for spin triplet Cooper pairs are represented in the third and fourth classes of Figure 2.2: even-frequency with odd-parity; and odd-frequency even-parity respectively. The former category was first discovered in the p-wave superfluid that forms in ^{3}He [7], and is also the proposed symmetry for the superconducting phase that occurs in Sr_2RuO_4 below 1.5 K.

The last category of triplets was intitially introduced by in 1974 by Berezinskiĭ [8] as a proposal for superfluidity in ^{3}He, which later was found to be p-wave instead. While an odd-frequency triplet state has so far never been observed by itself in nature, it was found that its pairing amplitude can be generated at (carefully engineered) superconductor-ferromagnet (S-F) interfaces [9, 10]. The triplet correlations studied in our S-F hybrids correspond to odd-frequency with s-wave symmetry.

Odd-frequency triplet pairing can be realised with a simple s-wave gap. This has a profound consequence on the survival of these correlations in a diffusive environment, where strong scattering leads to the mixing of different k states, see Figure 2.3. A p-wave gap, characterised by a k-dependent phase, would be fully suppressed under strong averaging in k-space. The s-wave gap on the other hand, is protected from scattering by its k-independent phase. As a consequence, the (odd-frequency) s-wave triplet pairing can be realised in a variety of diffusive S-F hybrids, made from a wide range of materials. In contrast, odd-parity (*e.g.* p-wave) triplet correlations are characterised by the clean limit (i.e. non-diffusive), and are restricted to a rather small number of materials, amongst which, Sr_2RuO_4 is one of the most prominent candidates (for a review see Refs. [11]). In this particular case, the order parameter

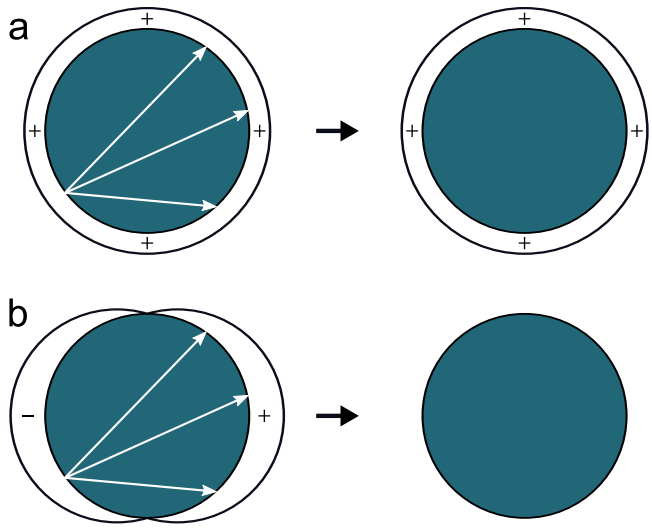

Figure 2.3: Representation of elastic scattering for two different order parameters. Each case shows the phase (denoted by $+/-$) and amplitude of the superconducting gap with respect to the Fermi surface (shaded). The arrows in the left panel represent typical elastic scattering events. The effect of scattering on the order parameter is shown in the right panel. **a**, The s-wave gap corresponds to an isotropic gap, where phase and amplitude are k-independent. The order parameter is practically unaffected under strong scattering. **b**, The p-wave order parameter is characterized by a k-dependent phase. As a result, the gap is averaged to zero by the scattering events — leading to a complete loss of superconductivity

is expected to be of $p_x \pm i p_y$ form, which can be considered as the two-dimensional analogue of the A-phase of superfluid ^{3}He.

2.2. PAIRING SYMMETRY OF Sr_2RuO_4

This section introduces the general formalism used to describe odd-parity symmetry, with an emphasis on p-wave pairing and its significance in the context of Sr_2RuO_4. This subject can be better appreciated with some background on the material.

2.2.1. Sr_2RuO_4: BASIC PROPERTIES

Since its discovery in 1994 by Maeno *et al.* [12], the superconducting state in Sr_2RuO_4 has been the subject of thousands of studies. Yet, to this date, the symmetry of its order parameter remains a moot point, making this material one of the most controversial superconductors.

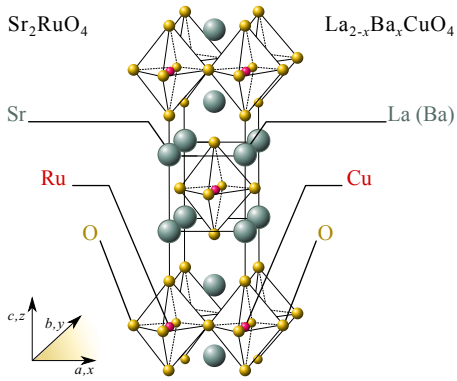

Figure 2.4: Sr_2RuO_4 (left) has a common layered perovskite structure with cuprate superconductors such as $La_{2-x}Ba_xCuO_4$ (right).

Table 2.1: Superconducting parameters of Sr_2RuO_4. H_c and H_{c2} are the thermodynamic and upper critical fields, respectively, ξ is the coherence length and λ is the magnetic penetration depth. The values are taken after Ref. [11].

Parameter			*ab*	*c*
T_c	[K]	1.5		
$\mu_0 H_c$	[T]	0.023		
$\mu_0 H_{c2}$	[T]		1.5	0.075
$\xi(0)$	[nm]		66	3.3
$\lambda(0)$	[nm]		190	3000

As shown in Figure 2.4, Sr_2RuO_4 has the same lattice structure as the high T_c cuprates such as $La_{2-x}Ba_xCuO_4$; but only becomes superconducting below 1.5 K. More importantly, unlike La_2CuO_4, which is an antiferromagnetic insulator, Sr_2RuO_4 is highly metallic with a (quasi) 2-dimensional Fermi surface consisting of three cylindrical sheets. This is also evident in the pronounced ratio of out-of-plane to in-plane resistivity ($\rho_c/\rho_{ab} > 1400$ at low temperatures) [13]. Sr_2RuO_4 is also highly anisotropic as a superconductor. As shown in Table 2.1, the in-plane to out-of-plane coherence lengths correspond to an anisotropy ratio of 20. However, ξ_c is still several times larger than the interlayer spacing (12.72 Å), allowing interlayer coherence.

In direct contrast to cuprates, normal state Sr_2RuO_4 can be well described as a (quasi) 2-dimensional Landau-Fermi liquid, with a distinct T^2 dependence of resistivity at low temperatures [14]. In fact the superconducting transition at 1.5 K only occurs in exceptionally clean crystals, with residual resistivities below $1\mu\Omega$cm at low temperatures, corresponding to an electron mean free path of $l \approx 1-3$ μm [15]. The superconducting state is also highly vulnerable to nonmagnetic impurities. It was found that even trace amounts of Al and Si (≈ 400 ppm) are sufficient to fully suppress T_c. As described in Section 2.1, such pronounced sensitivity to elastic scattering is a hallmark of unconventional superconductivity – where the order parameter has a k-dependent phase (see Figure 2.3).

Given the Landau-Fermi liquid behaviour; and the results of de Haas-van Alphen experiments — which show an enhancement of the effective mass by a factor of 3-5 [16] — it is also evident that the relevant interactions at low temperatures are predominantly due to strongly correlated electrons (as opposed to weak electron-phonon interactions). As first indicated by Sigrist and Rice (1995) [17], these characteristics bear an uncanny resemblance with that of ^{3}He, which also is a well-characterised

Landau-Fermi liquid. Based on this, and the close affinity with ferromagnetic oxides such as $SrRuO_3$, the authors proposed that Sr_2RuO_4 may have a triplet pairing — similar to that of the p-wave superfluid ^{3}He.

By now there is a substantial body of experimental evidence supporting the equal-spin triplet pairing in Sr_2RuO_4. These include NMR Knight-shift [18] and polarized neutron measurements [19], observation of half-quantum vortices [20, 21] (see Chapter 6) and the experiments on Sr_2RuO_4-ferromagnet hybrids [22]. The orbital parity of Sr_2RuO_4 however has been far more challenging to establish, and remains a highly debated subject.

2.2.2. d-VECTOR FORMALISM

Unlike for even-parity (i.e. $s-$ or d-wave pairing), a p-wave gap breaks the reflection symmetry of a 2-dimensional square lattice. Moreover, triplet pairing requires three independent gap functions to describe the spin symmetry. This can be represented by a general 2×2 gap matrix in momentum space.

$$\Delta(\boldsymbol{k}) = \begin{pmatrix} \Delta_{\boldsymbol{k},\uparrow\uparrow} & \Delta_{\boldsymbol{k},\uparrow\downarrow} \\ \Delta_{\boldsymbol{k},\downarrow\uparrow} & \Delta_{\boldsymbol{k},\downarrow\downarrow} \end{pmatrix} \tag{2.1}$$

For a given quantization direction, $\Delta_{\uparrow\uparrow}$ and $\Delta_{\downarrow\downarrow}$ represent spin projections of $+1$ and -1, respectively, while $\Delta_{\uparrow\downarrow} = \Delta_{\downarrow\uparrow} = \Delta_0$ corresponds to triplet pairing with zero spin projection (i.e. Cooper pairs do have a spin $S = 1$, but it lies perpendicular to the quantization axis). This gap matrix can be elegantly reduced to a three-dimensional complex vector $\boldsymbol{d}(\boldsymbol{k}) = [d_x(\boldsymbol{k}), d_y(\boldsymbol{k}), d_z(\boldsymbol{k})]$ (known as the d-vector), defined by

$$\begin{pmatrix} \Delta_{\boldsymbol{k},\uparrow\uparrow} & \Delta_{\boldsymbol{k},0} \\ \Delta_{\boldsymbol{k},0} & \Delta_{\boldsymbol{k},\downarrow\downarrow} \end{pmatrix} = \begin{pmatrix} -d_x(\boldsymbol{k}) + i\,d_y(\boldsymbol{k}) & d_z(\boldsymbol{k}) \\ d_z(\boldsymbol{k}) & d_x(\boldsymbol{k}) + i\,d_y(\boldsymbol{k}) \end{pmatrix} \tag{2.2}$$

A state is called unitary if $\left|\boldsymbol{d}(\boldsymbol{k}) \times \boldsymbol{d}^*(\boldsymbol{k})\right| = 0$. In this case, $\boldsymbol{d}(\boldsymbol{k})$ has a straightforward meaning: its amplitude is proportional to size of the gap at $(\boldsymbol{k}, -\boldsymbol{k})$; and its direction is perpendicular to the plane of equal-spin paired electrons, where $|\uparrow\uparrow\rangle$ and $|\downarrow\downarrow\rangle$ can be defined with respect to any quantization direction in that plane. For instance, if we choose z to be the quantization axis for spin, then the d-vector $\boldsymbol{d}(\boldsymbol{k}) = [0, 0, d_z(\boldsymbol{k})] \parallel \hat{\mathbf{z}}$ would correspond to $\Delta_{\uparrow\uparrow z} = \Delta_{\downarrow\downarrow z} = 0$. This only leaves Δ_{0z}, which means the Cooper pair spins must lie perpendicular to the quantization axis (i.e. in the xy plane $\perp \boldsymbol{d}$).

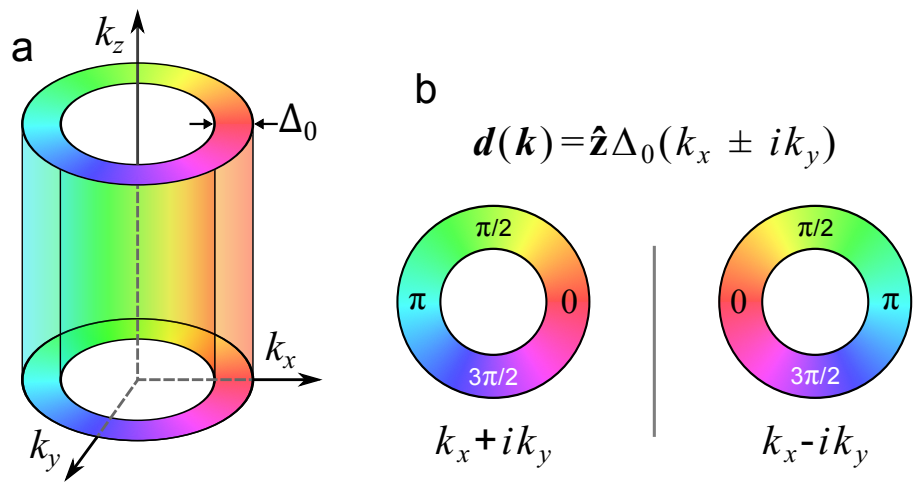

Figure 2.5: Energy gap of the chiral p-wave state $\boldsymbol{d}(\boldsymbol{k}) = \hat{\mathbf{z}}\Delta_0(k_x \pm ik_y)$. Colours represent the orbital phase of the order parameter θ_k, where $\boldsymbol{d}(\boldsymbol{k}) \propto e^{i\theta_k}$. (**a**) The two-dimensional gap forms around the cylindrical Fermi surface. While the gap amplitude Δ_0 is isotropic in the xy plane, its phase varies continuously. (**b**) The degenerate "chiral" states $k_x - ik_y$ and $k_x + ik_y$ wind their phase in opposite directions.

If we switch the quantization axis from z to any direction along the xy plane, there would be equal densities of $|\uparrow\uparrow\rangle$ and $|\downarrow\downarrow\rangle$ Cooper pairs with spin projections of $+1$ and -1, corresponding to zero spin polarization for the condensate. The absence of spin polarization is a common characteristic of all unitary states, since $|\Delta_{\uparrow\uparrow}|^2 - |\Delta_{\downarrow\downarrow}|^2 = 2i[\boldsymbol{d}(\boldsymbol{k}) \times \boldsymbol{d}^*(\boldsymbol{k})]_z = 0$.

In the absence of external fields, unitary states are more applicable (than nonunitary states) to Sr_2RuO_4. A list of possible unitary states for a tetragonal lattice with a cylindrical Fermi surface (appropriate for Sr_2RuO_4) is presented in Table 2.2. Amongst these, the $\boldsymbol{d}(\boldsymbol{k}) \propto \hat{\mathbf{z}}(k_x \pm ik_y)$ state is the most discussed pairing symmetry in the context of Sr_2RuO_4. In this case the d-vector is weakly pinned to the c-axis of the lattice ($z \parallel c$), and corresponds to a full (isotropic) gap in the ab plane (see Figure 2.5).

The order parameter has a k-dependent phase (represented by colours), which continuously winds in 2 dimensions as a function of k_x and k_y (i.e. in the ab plane). Since the order parameter can wind its phase in either directions, it results in two degenerate states $k_x + ik_y$ and $k_x - ik_y$ with opposite phase windings. This superconducting state $\boldsymbol{d}(\boldsymbol{k}) \propto e^{i\theta_k}$ is therefore characterised by an orbital phase θ_k which has a direction (i.e. winding left or right).

The direction of θ_k is considered as the "chirality" of the superconducting state, and is responsible for the broken time-reversal symmetry (TRS) associated with this order parameter. A bulk crystal of Sr_2RuO_4 is expected to spontaneously break into a

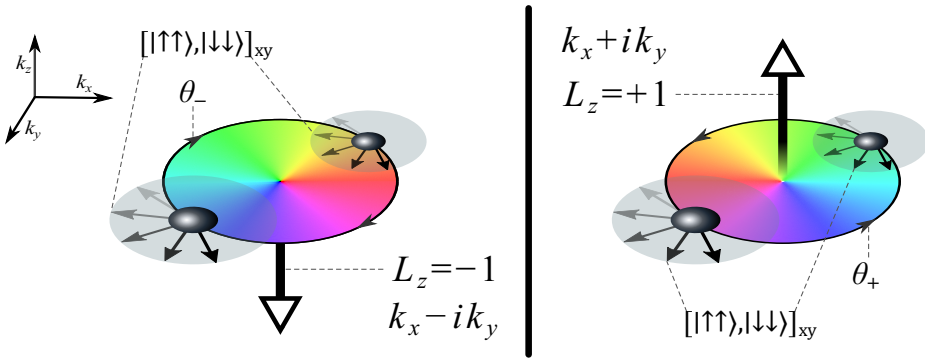

Figure 2.6: Chiral Cooper pairs of $k_x - ik_y$ and $k_x + ik_y$ states. Small arrows represent equal-spin pairing of the electrons. Spin quantization axis is defined as *any* direction in the xy plane, resulting in zero spin polarization. Both chiral states have the same spin symmetry. Colours correspond to the orbital phase θ, which has a different winding direction in each state, hence the $\pm$ sign. Large arrows represent the orbital angular momentum of each Cooper pair, which is responsible for breaking the time-reversal symmetry.

multitude of spatially segregated *domains* of $k_x + ik_y$ and $k_x - ik_y$ chirality. However, if a system is sufficiently small and homogenous, it can also be in a single domain state. This means that, when cooled below T_c, one of the chiral states will spontaneously emerge over the entire superconductor.

As shown in Figure 2.6, Cooper pairs consist of equal-spin electrons with a total spin $S = 1$, which lies in the ab plane. However, $|\uparrow\uparrow\rangle$ and $|\downarrow\downarrow\rangle$ states have equal weights along *any* given quantization axis in the ab plane. While $|\uparrow\uparrow\rangle$ and $|\downarrow\downarrow\rangle$ each have a spin projection ($S_{xy} = \pm 1$), the total spin polarization is zero. In the absence of external fields, this can be thought of as the superposition of $|\uparrow\uparrow\rangle$ and $|\downarrow\downarrow\rangle$ states. Also note that both chiralities have the same spin symmetry i.e. $k_x + ik_y$ and $k_x - ik_y$ cannot be distinguished by the spin part of the order parameter.

Generally, a p-wave orbital would automatically imply an orbital angular momentum $L = 1$. For $k_x \pm ik_y$ states, this would correspond to $L_z = \pm 1$. This means that the electrons of a Cooper pair have a relative orbital motion, which depends on chirality (the pairs are rotating either clockwise or anticlockwise). The direction of orbital motion, and therefore the sign of L_z, is determined by the winding direction of the orbital phase θ_k (represented by θ_- and θ_+ in Figure 2.6). The fact that within each chiral state *all* electron pairs have the same rotation (either clockwise or anticlockwise) breaks the TRS. Unlike the non-unitary states, which break TRS by having a preference of one of the spins, here TRS breaking is purely due to the orbital part of the wavefunction.

An important consequence of this would be the emergence of the so-called *edge current*, which refers to a finite charge current at the boundaries of a single chiral do-

main. Even in the absence of external fields, the edge current would spontaneously appear at the onset of T_c and its direction is purely defined by the intrinsic direction of the orbital phase – and hence chirality.

2.2.3. POSSIBLE SYMMETRIES FOR Sr_2RuO_4

Our discussion on parity has so far been focused on the $k_x \pm ik_y$ state, while we conveniently ignored the other symmetry candidates for Sr_2RuO_4 . Table 2.2 lists all the unitary states with a p-symmetry for a tetragonal crystal with a cylindrical Fermi surface (labelled **A** to **G**). The derivations can be found in Refs. [17, 23, 24] The following discussion intends to compare the likelihood of the listed symmetries by examining the results of a number of key experiments. For a more detailed review on this topic, the reader is refered to Refs. [1, 11, 25].

We can divide the items of Table 2.2 into two groups based on orientation of the d-vector. In the first category (**A—D**), the d-vector has an arbitrary orientation in the ab plane. This means that the spin of the Cooper pairs must be aligned with c axis (d-vector points perpendicular to Cooper pair spin). For the second category (**E—G**), which also includes the previously mentioned $k_x \pm ik_y$ case, the d-vector has a well-defined direction, pointing along the c-axis. Hence, the Cooper pairs have spins that lie in the ab plane (as we saw for $k_x \pm ik_y$). The two categories can therefore be distinguished by the spin part of the order parameter. This can be investigated by measuring the spin susceptibility in the presence of an external magnetic field. For instance, if there is sufficient spin-orbit coupling to pin the d-vector to the lattice, which is the case for (**E—G**), then the measured spin susceptibility would depend on the direction of the d-vector.

Under a constant applied field, the spin susceptibility of a singlet superconductor $S = 0$ would simply begin to drop when cooled down below T_c. For a triplet superconductor however the situation is considerably different. If the external field is along the plane of equal-spin paired electrons ($H \perp \boldsymbol{d}$), it would induce a spin polarization by creating an imbalance between the population of $\uparrow\uparrow$ and $\downarrow\downarrow$ states. By contrast, if $H \parallel \boldsymbol{d}$ the spins of the Cooper pairs will lie in a perpendicular plane to the applied field, and the condensate cannot be polarized.

The spin susceptibility of Sr_2RuO_4 has been measured by a number of independent techniques, including Knight shift experiments [18] and polarized neutron scattering [19]. These studies have consistently found that, if a field is applied along the ab plane, the spin susceptibility remains unchanged by the superconducting transition (i.e. same susceptibility signal above and below T_c).

There are two aspects to the significance of these observations. First, they provide

d-vector	Δ/Δ_0	direction	TRS	Label
$\hat{\mathbf{x}}k_x + \hat{\mathbf{y}}k_y$	$\sqrt{k_x^2 + k_y^2}$	$\boldsymbol{d} \parallel ab$	preserved	**A**
$\hat{\mathbf{x}}k_y - \hat{\mathbf{y}}k_x$	$\sqrt{k_x^2 + k_y^2}$	$\boldsymbol{d} \parallel ab$	preserved	**B**
$\hat{\mathbf{x}}k_x - \hat{\mathbf{y}}k_y$	$\sqrt{k_x^2 + k_y^2}$	$\boldsymbol{d} \parallel ab$	preserved	**C**
$\hat{\mathbf{x}}k_y + \hat{\mathbf{y}}k_x$	$\sqrt{k_x^2 + k_y^2}$	$\boldsymbol{d} \parallel ab$	preserved	**D**
$\hat{\mathbf{z}}k_x$	$\lvert k_x \rvert$	$\boldsymbol{d} \parallel c$	preserved	**E**
$\hat{\mathbf{z}}(k_x + k_y)$	$\lvert k_x + k_y \rvert$	$\boldsymbol{d} \parallel c$	preserved	**F**
$\hat{\mathbf{z}}(k_x \pm i k_y)$	$\sqrt{k_x^2 + k_y^2}$	$\boldsymbol{d} \parallel c$	broken	**G**

Table 2.2: List of possible unitary states with p-wave symmetry for Sr_2RuO_4 [1].

strong evidence in favour of triplet pairing in Sr_2RuO_4, due to the measured spin polarization below T_c. The second is that the same behaviour is observed for different directions in the ab plane, which suggests a uniform d-vector pointing along the c axis. This is in agreement with our second category (**E—G**), and $\hat{\mathbf{z}}(k_x \pm i k_y)$ in particular, since the amplitude of $\boldsymbol{d}$ does not have a $\boldsymbol{k}_{x,y}$ dependence (i.e. the gap is homogenous in the ab plane). However, these measurements still cannot conclusively prove that the d-vector is pinned to the c-axis. The uncertainty comes from the fact that a d-vector with no specific relation to the crystal (uniform in all 3-dimensions), could presumably also change its orientation under the applied field and yield a similar results. One solution to this would be to measure the spin susceptibility with $H \parallel c$. Since the spins should then be in the plane that is perpendicular to the applied field, one would expect to find no spin polarization. Such experiments however have proven rather challenging due to the large anisotropy of the superconductor, which requires the applied field to be 20 times smaller than the ones used for the ab plane (see Table 2.1).

In summary, based on spin-susceptibility measurements, an order parameter with $\boldsymbol{d} \parallel c$ (i.e. $|\uparrow\uparrow\rangle, |\downarrow\downarrow\rangle \parallel ab$), seems quite probable for Sr_2RuO_4. Amongst the three order parameters with $\boldsymbol{d} \parallel c$, only $\hat{\mathbf{z}}(k_x \pm i k_y)$ corresponds to a full gap in the ab plane. Both $\hat{\mathbf{z}}k_x$ and $\hat{\mathbf{z}}(k_x + k_y)$ cases (**E** and **F**) are associated with vertical line nodes. So far however, no evidence of such vertical line nodes has been found, making the relevance of **E** and **F** somewhat harder to justify.

Arguably, the most unique characteristic of a chiral order parameter is the breaking of

time-reversal symmetry (TRS). This fundamental distinction can already be deduced from the list of d-vectors in Table 2.2, where $\hat{\mathbf{z}}(k_x \pm i k_y)$ is the only one with broken TRS. The reason for this can be understood by examining how TRS is restored in a number of examples. For instance, consider $\hat{\mathbf{x}}k_x + \hat{\mathbf{y}}k_y$ (state **A**), which can also be written as

$$\hat{\mathbf{x}}k_x + \hat{\mathbf{y}}k_y = \frac{1}{2}\Big[\overbrace{(\hat{\mathbf{x}} + i\hat{\mathbf{y}})}^{S_z=+1}\underbrace{(k_x - i k_y)}_{L_z=-1} + \overbrace{(\hat{\mathbf{x}} - i\hat{\mathbf{y}})}^{S_z=-1}\underbrace{(k_x + i k_y)}_{L_z=+1}\Big] \tag{2.3}$$

which is the superposition of two states with opposite spin ($\hat{\mathbf{x}} \pm i\hat{\mathbf{y}}$) and orbital ($k_x \pm i k_y$) components. Each state has a spin (S_z) and orbital angular momentum (L_z). They are both quantized along the c-axis, and are antiparallel to each other (i.e. $S_z = \mp 1$ corresponds to $L_z = \pm 1$). When the two states are combined however, the resulting L and S are both zero, and TRS is therefore respected.

A more similar example to the chiral d-vector $\hat{\mathbf{z}}(k_x \pm i k_y)$ would be $\hat{\mathbf{z}}k_x$ (state **E**), as it also has a direction along c — with the spin plane $(|\uparrow\uparrow\rangle, |\downarrow\downarrow\rangle)_{xy} \parallel ab$. This can be represented as

$$\hat{\mathbf{z}}k_x = \frac{1}{2}\hat{\mathbf{z}}\Big[\overbrace{(k_x + i k_y)}^{L_z=+1} + \underbrace{(k_x - i k_y)}_{L_z=-1}\Big] \tag{2.4}$$

This can be considered as the superposition of two states with equal and opposite angular momenta. The spin of each state is characterized by the equal population of $|\uparrow\uparrow\rangle$ and $|\downarrow\downarrow\rangle$ pairs, defined with respect to any quantization axis along the ab plane. Consequently, this order parameter cannot be assigned with a net value for either L or S, which means that TRS is once again respected.

The order parameter of $\hat{\mathbf{z}}(k_x \pm i k_y)$ is the only p-wave unitary state which spontaneously breaks TRS with its orbital part. This implies that each chiral state will have a finite magnetization, even in the absence of external magnetic fields. There are currently two independent experiments which strongly support this claim. The first evidence of TRS breaking came from muon spin-relaxation (μSR) measurements, which showed the spontaneous appearance of an *internal* magnetic field below the superconducting transition temperature [26]. In this technique, 100 % spin-polarized muons are implanted (one at the time) into a material over a finite depth. The muon spin then begins to evolve in presence of the *local* magnetic fields at its implantation site. Subsequently, when the muon decays (≈ 2.2 μs), a positron is emitted in a

direction that corresponds to the spin of the muon at the time of its decay. Hence, each muon acts as a local magnetic probe for its immediate environment. A typical experiment is based on measuring 10^7 individual events.

In the absence of external magnetic fields the muon measurements found a dilute distribution of internal magnetic fields. This is a direct indication of TRS breaking, and also supports the existence of chiral domains, where the edge currents of individual domains can results in local magnetic fields *inside* the superconductor. Given the finite size of the domains, and their arbitrary arrangements in a three-dimensional sample, it is reasonable that the internal fields would be heavily diluted and smeared out. This makes μSR a particularly powerful technique, since a muon can directly probe the local magnetic fields of its immediate environment. While μSR serves as a reliable test for TRS — which would ultimately be in favour of the chiral order parameter — the measurements cannot conclusively prove that the internal magnetic fields of Sr_2RuO_4 are necessarily produced by chirality.

The breaking of TRS in Sr_2RuO_4 has also been confirmed by ultra-high resolution magneto-optic polar Kerr effect (PKE) measurements [27]. This technique is related to the magneto-optic Kerr effect (MOKE), where the polarization direction of a polarized light beam is rotated upon being reflected from a magnetic surface. The PKE experiments found a rotation of the polarization plane of the light reflected from the *ab* plane of the crystal. This rotation corresponded to a Kerr signal of the order of 10^{-9} rad. It appears spontaneously at $T_c \approx 1.5$ K and increases in magnitude by lowering the temperature down to 0.5 K, where it seems to saturate at 60×10^{-9} rad. While this Kerr signal may seem small, it is still well within the exceptionally high resolution of the measurement apparatus (see Ref. [28] for more details).

In the absence of external fields, the sign of the Kerr signal randomly switches with each cooling cycle. The sign of the signal may indeed correspond to the orbital angular momentum of a chiral domain. In that case, the chirality of the area probed with the beam would be naturally non-deterministic, switching randomly with each cooling cycle. More importantly, it was shown that the sign of the Kerr signal can be reversed by field cooling ($\gtrsim 5$ mT) the sample prior to the (zero field) PKE measurements. It has been proposed that applying a magnetic field whilst cooling through T_c, can promote one chirality over the other. The field is expected to enhance the size of the domains whose angular momentum has the same direction as the applied field [29].

To this date, the results of the PKE experiments provide one of the most compelling arguments in favour of the chiral order parameter in Sr_2RuO_4. In addition to demonstrating TRS breaking, the PKE measurements indicate that the condensate may be divided into domains with opposite magnetic signs, along the *ab* plane. Based on the beam diameter (25 μm) these domains are expected to be of the order of a few

microns.

Motivated by the results of PKE measurements, there was a series of attempts to verify the existence of edge currents by searching for stray fields coming out of the surface of Sr_2RuO_4 [30–33]. These attempts have, as yet, been unsuccessful. The reason for this is not currently understood, but it may well be due to an efficient screening mechanism which can heavily suppress the effective flux generated by the edge current, since Meissner screening is still applicable. For instance, consider the typical Sr_2RuO_4 sample used in most experiments, which is 100s of microns thick along the c-axis of the crystal. Meanwhile, the coherence length in that direction is only $\xi_c = 3.3$ nm. Instead of stacking the domains with the same chirality on top of each other, whose edge currents would generate a net magnetic flux (subject to Meissner screening), the condensate could potentially lower its energy by switching its chirality along the c-axis over the scale of a few ξ_c. By averaging out the net flux threading this vertical stack of domains, the quasi-2-dimensional order parameter could minimise the energy associated with the Meissner screening. However, this would also heavily suppress the external dipole fields which can be detected by scanning-SQUID [30, 31] and scanning-Hall probe [32, 33] measurements.

In summary, from all the d-vectors in Table 2.2, the chiral symmetry is the only which can account for the results of μSR and the PKE experiments, making it by far the most likely candidate amongst the unitary states with a p-symmetry. Though, a direct observation of spontaneous edge currents is still lacking. There is however substantial body of transport experiments which support the presence of chiral domains, and the breaking of TRS. Unlike the experiments described above, which rely on measuring the magnetization, transport experiments can probe the non-trivial phase variations produced by the chiral states. This is the subject of Chapter 7.

REFERENCES

[1] A. P. Mackenzie and Y. Maeno. The superconductivity of Sr_2RuO_4 and the physics of spin-triplet pairing. *Reviews of Modern Physics*, 75(2):657, 2003.

[2] A. A. Abrikosov, L. P. Gorkov, and I. E. Dzyaloshinski. Methods of quantum field theory in statistical physics. *Dover Publications*, 1975.

[3] T. Matsubara. A new approach to quantum-statistical mechanics. *Progress of Theoretical Physics*, 14(4):351–378, 1955.

[4] M. Eschrig, T. Löfwander, T. Champel, J. Cuevas, J. Kopu, and G. Schön. Symmetries of pairing correlations in superconductor–ferromagnet nanostructures. *Journal of Low Temperature Physics*, 147(3-4):457–476, 2007.

[5] Y. Tanaka and A. A. Golubov. Theory of the proximity effect in junctions with unconventional superconductors. *Physical Review Letters*, 98(3):037003, 2007.

[6] Y. Tanaka, Y. Tanuma, and A. A. Golubov. Odd-frequency pairing in normal-metal/superconductor junctions. *Physical Review B*, 76(5):054522, 2007.

[7] A. J. Leggett. A theoretical description of the new phases of liquid ^{3}He. *Reviews of Modern Physics*, 47(2):331, 1975.

[8] V. Berezinskiĭ. New model of the anisotropic phase of superfluid ^{3}He. *JETP Lett*, 20(9):287–289, 1974.

[9] F. Bergeret, A. Volkov, and K. Efetov. Long-range proximity effects in superconductor-ferromagnet structures. *Physical Review Letters*, 86(18):4096, 2001.

[10] F. Bergeret, A. F. Volkov, and K. B. Efetov. Odd triplet superconductivity and related phenomena in superconductor-ferromagnet structures. *Reviews of Modern Physics*, 77(4):1321, 2005.

[11] Y. Maeno, S. Kittaka, T. Nomura, S. Yonezawa, and K. Ishida. Evaluation of spin-triplet superconductivity in Sr_2RuO_4. *Journal of the Physical Society of Japan*, 81(1):011009, 2011.

[12] Y. Maeno, H. Hashimoto, K. Yoshida, S. Nishizaki, T. Fujita, J. Bednorz, and F. Lichtenberg. Superconductivity in a layered perovskite without copper. *Nature*, 372(6506):532, 1994.

[13] N. Hussey, A. Mackenzie, J. Cooper, Y. Maeno, S. Nishizaki, and T. Fujita. Normal-state magnetoresistance of Sr_2RuO_4. *Physical Review B*, 57(9):5505, 1998.

[14] A. Mackenzie, S. Julian, A. Diver, G. McMullan, M. Ray, G. Lonzarich, Y. Maeno, S. Nishizaki, and T. Fujita. Quantum oscillations in the layered perovskite superconductor Sr_2RuO_4. *Physical Review Letters*, 76(20):3786, 1996.

[15] A. Mackenzie, R. Haselwimmer, A. Tyler, G. Lonzarich, Y. Mori, S. Nishizaki, and Y. Maeno. Extremely strong dependence of superconductivity on disorder in Sr_2RuO_4. *Physical Review Letters*, 80(1):161, 1998.

[16] A. Mackenzie, S. Julian, A. Diver, G. McMullan, M. Ray, G. Lonzarich, Y. Maeno, S. Nishizaki, and T. Fujita. Quantum oscillations in the layered perovskite superconductor Sr_2RuO_4. *Physical Review Letters*, 76(20):3786, 1996.

[17] T. Rice and M. Sigrist. Sr_2RuO_4: an electronic analogue of ^{3}He ? *Journal of Physics: Condensed Matter*, 7(47):L643, 1995.

[18] K. Ishida, H. Mukuda, Y. Kitaoka, K. Asayama, Z. Mao, Y. Mori, and Y. Maeno. Spin-triplet superconductivity in Sr_2RuO_4 identified by ^{17}O Knight shift. *Nature*, 396(6712):658, 1998.

[19] J. Duffy, S. Hayden, Y. Maeno, Z. Mao, J. Kulda, and G. McIntyre. Polarized-neutron scattering study of the Cooper-pair moment in Sr_2RuO_4. *Physical Review Letters*, 85(25):5412, 2000.

[20] J. Jang, D. Ferguson, V. Vakaryuk, R. Budakian, S. Chung, P. Goldbart, and Y. Maeno. Observation of half-height magnetization steps in Sr_2RuO_4. *Science*, 331(6014):186–188, 2011.

[21] Y. Yasui, K. Lahabi, M. S. Anwar, S. Yonezawa, T. Terashima, J. Aarts, and Y. Maeno. Half-quantum fluxoid features in the magnetotransport of Sr_2RuO_4 micro rings. *Bulletin of the American Physical Society*, 2018.

[22] M. Anwar, S. Lee, R. Ishiguro, Y. Sugimoto, Y. Tano, S. Kang, Y. Shin, S. Yonezawa, D. Manske, H. Takayanagi, et al. Direct penetration of spin-triplet superconductivity into a ferromagnet in au/$SrRuO_3$/Sr_2RuO_4 junctions. *Nature Communications*, 7:13220, 2016.

[23] J. F. Annett. Symmetry of the order parameter for high-temperature superconductivity. *Advances in Physics*, 39(2):83–126, 1990.

[24] K. Machida, M.-a. Ozaki, and T. Ohmi. Odd-parity pairing superconductivity under tetragonal symmetry-possible application to Sr_2RuO_4. *Journal of the Physical Society of Japan*, 65(12):3720–3723, 1996.

[25] A. P. Mackenzie, T. Scaffidi, C. W. Hicks, and Y. Maeno. Even odder after twenty-three years: the superconducting order parameter puzzle of Sr_2RuO_4. *NPJ Quantum Materials*, 2(1):40, 2017.

[26] G. M. Luke, Y. Fudamoto, K. Kojima, M. Larkin, J. Merrin, B. Nachumi, Y. Uemura, Y. Maeno, Z. Mao, Y. Mori, et al. Time-reversal symmetry-breaking superconductivity in Sr_2RuO_4. *Nature*, 394(6693):558, 1998.

[27] J. Xia, Y. Maeno, P. T. Beyersdorf, M. Fejer, and A. Kapitulnik. High resolution polar Kerr effect measurements of Sr_2RuO_4: evidence for broken time-reversal symmetry in the superconducting state. *Physical Review Letters*, 97(16):167002, 2006.

[28] J. Xia, P. T. Beyersdorf, M. M. Fejer, and A. Kapitulnik. Modified sagnac interferometer for high-sensitivity magneto-optic measurements at cryogenic temperatures. *Applied Physics Letters*, 89(6):062508, 2006.

[29] A. Bouhon and M. Sigrist. Influence of the domain walls on the Josephson effect in Sr_2RuO_4. *New Journal of Physics*, 12(4):043031, 2010.

[30] J. Kirtley, C. Kallin, C. Hicks, E.-A. Kim, Y. Liu, K. Moler, Y. Maeno, and K. Nelson. Upper limit on spontaneous supercurrents in Sr_2RuO_4. *Physical Review B*, 76(1):014526, 2007.

[31] C. W. Hicks, J. R. Kirtley, T. M. Lippman, N. C. Koshnick, M. E. Huber, Y. Maeno, W. M. Yuhasz, M. B. Maple, and K. A. Moler. Limits on superconductivity-related magnetization in Sr_2RuO_4 and $PrOs_4Sb_12$ from scanning SQUID microscopy. *Physical Review B*, 81(21):214501, 2010.

[32] P. J. Curran, V. V. Khotkevych, S. J. Bending, A. S. Gibbs, S. L. Lee, and A. Mackenzie. Vortex imaging and vortex lattice transitions in superconducting Sr_2RuO_4 single crystals. *Physical Review B*, 84(10):104507, 2011.

[33] P. Curran, S. Bending, W. Desoky, A. S. Gibbs, S. L. Lee, and A. Mackenzie. Search for spontaneous edge currents and vortex imaging in Sr_2RuO_4 mesostructures. *Physical Review B*, 89(14):144504, 2014.

3

TRIPLET COOPER PAIRS IN MAGNETIC HYBRIDS

3.1. PROXIMITY EFFECT

PROXIMITY EFFECT is a general term used to describe the phenomena which occur at the interface between two different orders. We begin this section with a basic example, where a conventional (singlet) superconductor (S) is sharing an interface with a nonmagnetic normal metal (N), illustrated in Figure 3.1. At the interface the superconducting condensate $\Psi(\mathbf{R})$ extends into its adjacent layer, making it superconducting by proxy. In other words, despite the absence of an attractive interaction, there is still a finite probability of finding Cooper pairs in the normal metal. One can therefore think of this as the "leakage" of Cooper pairs into an adjacent medium.

As shown in Figure 3.1, deep within the superconductor the pair amplitude is at its maximum $\Psi(\mathbf{R} \to -\infty) = \Psi_0$, while on the other side of the interface, in the normal metal, the condensate must ultimately drop to zero $\Psi(\mathbf{R} \to +\infty) = 0$. Proximity effect is concerned with the region in between, where $|\Psi|$ falls as a function of distance. The characteristic length scale over which the order parameter can vary its amplitude is called the coherence length ξ, which is a material property. At the interface, Cooper pairs are depleted from the superconductor over a distance defined by $\xi_s(T) \approx \xi(0)(1/\sqrt{T/T_c - 1})$, where $\xi(0)$ corresponds to the coherence length of the superconductor at $T = 0$ K. Depending on the material, the value of $\xi(0)$ can vary from a couple of nanometer (cuprates) up to over a micron (Aluminium).[1]

[1] It is worth noting that Al is a rather extreme example. For most superconductors $\xi(0)$ is less than 200 nm.

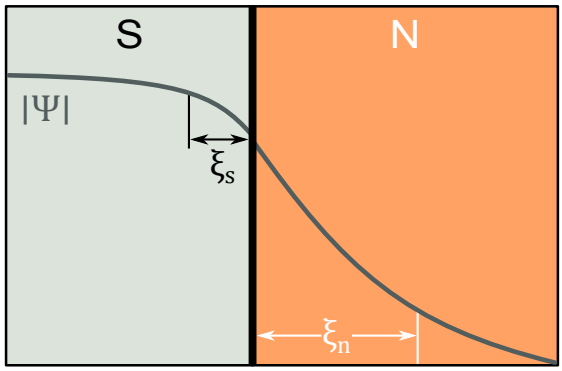

Figure 3.1: Proximity effect at the interface between a superconductor (S) and a normal metal (N). As the condensate Ψ spreads across the interface, its amplitude decays over the length scales ξ_s and ξ_n.

On the other side of the interface, the amplitude of Ψ falls over the characteristic length of ξ_n. In a diffusive system (dirty limit), defined by $\xi_n < l$, where l is the mean fee path of the electron, ξ_n is given as

$$\xi_n = \sqrt{\frac{\hbar D_n}{k_B T}} \tag{3.1}$$

where $\hbar$ is the Planck constant, D_n is the diffusion coefficient of the normal metal and k_B is the Boltzmann constant. For a transparent interface, this length scale is typically 100s of nm. While ξ_s and ξ_n may correspond to widely different values, the total condensate remains conserved. i.e. for every pair injected into the normal metal, a pair is "drained" from the superconductor.

So far we have described the proximity effect in terms of a macroscopic order parameter. There is however an equivalent microscopic description which concerns Andreev reflections. In this process an incident electron (hole) from N, with an energy below the superconducting gap, is retroreflected at the interface as a hole (electron) with equal and opposite momentum. The Andreev reflected electrons and holes result in a phase-coherent transport in units of $2e$, which is equivalent to transferring Cooper pairs across the interface. Likewise, the electron-hole pairs can maintain their phase-coherence in the normal metal over a characteristic distance which depends on the energy of the electron (hole) with respect to the Fermi energy, but on average, corresponds to ξ_n.[2]

[2] For more details on Andreev process see Refs. [1, 2].

3.1.1. SPIN-ACTIVE INTERFACES

Consider now replacing the normal metal with a ferromagnetic layer (F). The main difference with a normal metal is the exchange field of the ferromagnet E_{ex}, which splits the electronic bands for up and down spins by shifting their energy by $2E_{\text{ex}}$. The singlet Cooper pair consists of two electrons with equal and opposite spins $(\uparrow,\downarrow)$ and momenta $(\mathbf{k}_f, -\mathbf{k}_f)$. This means a pair has a total spin and momentum of zero. By splitting the Fermi surface, the exchange field introduces a shift in momenta for spin up $\mathbf{k}_{f\uparrow} = \mathbf{k}_f + \mathbf{Q}/2$ and spin down $\mathbf{k}_{f\downarrow} = \mathbf{k}_f - \mathbf{Q}/2$ electrons (see Figure 3.2 **a**). In the diffusive limit, the shift corresponds to $Q = 2E_{\text{ex}}/(\hbar v_f)$, where v_f is the Fermi velocity. This results in a finite momentum for $|\uparrow\downarrow\rangle$: $\mathbf{k}_{f\uparrow} - \mathbf{k}_{f\downarrow} = \mathbf{Q}$, and similarly for $|\downarrow\uparrow\rangle$: $\mathbf{k}_{f\downarrow} - \mathbf{k}_{f\uparrow} = -\mathbf{Q}$. The singlet state is then transformed into the linear combination of terms with different momenta

$$\frac{1}{\sqrt{2}}(|\uparrow\downarrow\rangle - |\downarrow\uparrow\rangle) \quad \longrightarrow \quad \frac{1}{\sqrt{2}}\Big(|\uparrow\downarrow\rangle\, e^{i\mathbf{R}.\mathbf{Q}} - |\downarrow\uparrow\rangle\, e^{-i\mathbf{R}.\mathbf{Q}}\Big) \tag{3.2}$$

which can be simplified to

$$\frac{1}{\sqrt{2}}\Big[\Big(|\uparrow\downarrow\rangle - |\downarrow\uparrow\rangle\Big)\cos(\mathbf{R}.\mathbf{Q}) \quad + \quad i\Big(|\uparrow\downarrow\rangle + |\downarrow\uparrow\rangle\Big)\sin(\mathbf{R}.\mathbf{Q})\Big]. \tag{3.3}$$

The first term is an oscillating singlet state $|0,0\rangle$ with zero spin ($S = 0$), while the second term describes a triplet state $|1,0\rangle$ ($S = 1$), whose spin projection is zero ($m = 0$) with respect to the spin quantization axis, which is defined by the direction of the exchange field of the ferromagnet. This spatially inhomogeneous singlet-triplet mixture (shown in Figure 3.2 **b**) is the equivalent of the famous FFLO state[3], which was originally intended as a possibility for *bulk* ferromagnetic superconductors [3, 4].

These correlations however can only survive in the F layer within a finite length scale from the interface. In a diffusive system (relevant to our structures) all pair amplitudes decay exponentially over ξ_{f}, which is given by

$$\xi_{\text{f}} = \sqrt{\frac{\hbar D}{E_{\text{ex}}}} \tag{3.4}$$

[3] Also known as the LOFF state, it is named after Peter Fulde and Richard Ferrell [3], and Anatoly Larkin and Yurii Ovchinnikov [4], who independently proposed the idea in connection with the coexistence problem of superconductivity with ferromagnetism. More details on this can be found in Refs. [5, 6]

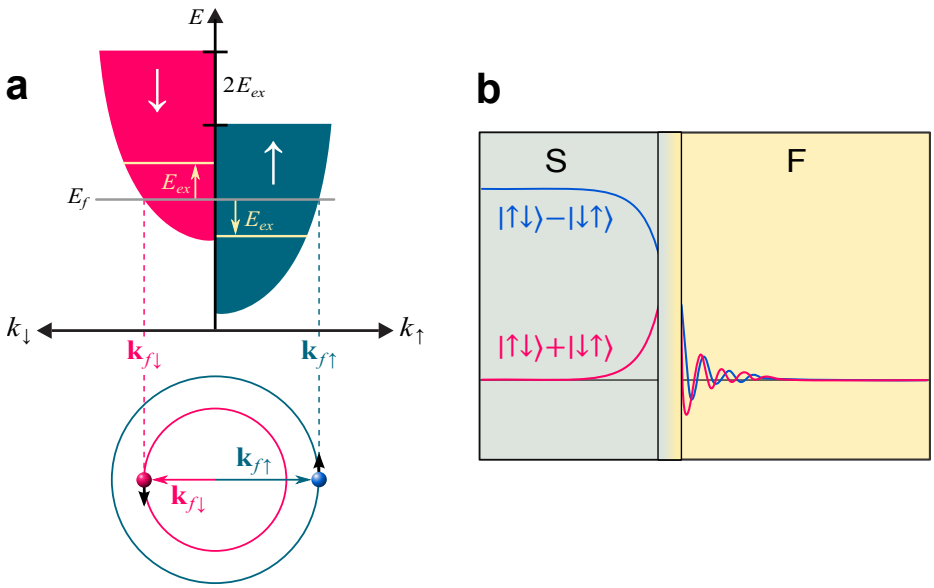

Figure 3.2: Cooper pairs at S-F interface: short-range proximity effect. **a** Spin polarization of the ferromagnet splits the bands for spin up (blue) and spin down (red) electrons by $2E_{\text{ex}}$ at the Fermi surface E_f, and leads to a shift in their momenta. This results in a finite momentum of the Cooper pair ($\mathbf{k}_{f\uparrow} \neq -\mathbf{k}_{f\downarrow}$). **b** singlet (blue)-triplet (red) mixing at the S-F interface. Spatially inhomogeneous singlet triplet mixture in the F layer corresponds to the FFLO state. In a diffusive ferromagnet with strong spin polarization, the correlations decay exponentially over $\xi_{\text{f}} \approx 1-5$ nm. The reflections from F layer cause spin-dependent phase shifts on the other side of the interface, forming a singlet-triplet mixture in S.

Unlike ξ_{n}, which was mostly determined by thermal processes, the value of ξ_{f} is dominated by the exchange energy E_{ex}. To gain some perspective, we can roughly translate E_{ex} to the Curie temperature, which is typically in the order of 100s of Kelvin. This means that in strong ferromagnets like Co and Ni, all correlations die out within $3-5$ nm from the interface— hence the name short-range proximity effect. The stronger the spin-polarization, the more suppressed the FFLO state is in the ferromagnet. At the same time however, stronger spin-polarization would have a larger impact on the superconducting side, where it induces an $m = 0$ triplet component (see Figure 3.2 **b**). This triplet component is a product of spin-dependent scattering phase shifts at the interface, which grow larger with the spin-polarization of F.

The exchange field results in different scattering phase delays for different spins ($\phi_\uparrow, \phi_\downarrow$). The corresponding phase shift can be expressed in terms of a spin-mixing *angle*, defined as $\theta = \phi_\uparrow - \phi_\downarrow$. In case of Cooper pairs, θ corresponds to the phase difference between a spin-up electron with momentum $\mathbf{k}$, and a spin-down with $-\mathbf{k}$, where $\mathbf{k}$ and $-\mathbf{k}$ point towards and away from the interface respectively. This results in a phase shift of θ for $|\uparrow\downarrow\rangle$, and $-\theta$ for $|\downarrow\uparrow\rangle$. The singlet state is hence converted to

$$\frac{1}{\sqrt{2}}(|\uparrow\downarrow\rangle - |\downarrow\uparrow\rangle) \quad \longrightarrow \quad \frac{1}{\sqrt{2}}\Big(|\uparrow\downarrow\rangle\, e^{i\theta} - |\downarrow\uparrow\rangle\, e^{-i\theta}\Big) \tag{3.5}$$

and can be written as

$$\frac{1}{\sqrt{2}}\Big[\Big(|\uparrow\downarrow\rangle - |\downarrow\uparrow\rangle\Big)\cos(\theta) \quad + \quad i\Big(|\uparrow\downarrow\rangle + |\downarrow\uparrow\rangle\Big)\sin(\theta)\Big] \tag{3.6}$$

In analogy to the formation of the FFLO state, we again arrive at a mixture of singlet $|0,0\rangle$ (first term) and triplet pairs $|1,0\rangle$ (second term) with no spin projection. The distinction here is that, instead of a momentum, the pair acquires a phase shift θ. The angle θ describes the rotation of the spin components *perpendicular* to the quantization axis under reflection. More importantly, we can consider θ as a measure of singlet-triplet mixing, which is a crucial ingredient for generating long-range triplet correlations.

3.1.2. LONG-RANGE TRIPLET CORRELATIONS

Given their capacity to generate $m = 0$ triplet correlations, it is natural to wonder if a spin-active interface can also provide the other triplet states $|\uparrow\uparrow\rangle$ and $|\downarrow\downarrow\rangle$ ($m = \pm 1$). Such correlations correspond to equal-spin pairing of the electrons, which puts them in a particularly interesting position. The reason for this is that pairs with parallel spin alignment are almost immune to the usual destructive influence of the exchange field, and can therefore lead to long-range superconducting correlations which are also spin-polarized. This provides an attractive prospect for spintronic applications, where decoherence and dissipation can be substantially minimized.

In order to proceed, consider the case where F and S are separated by a magnetic interface, whose magnetization vector $\mathbf{M}_i$ can vary with respect to that of the F layer $\mathbf{M}_\mathrm{F}$ (see Figure 3.3). The thickness of the interface region is restricted to values close to its ξ_f. For simplicity, we assume the interface and F are both highly spin-polarized, and therefore refrain from including the damped FFLO state in the sketches.

When $\mathbf{M}_i \parallel \mathbf{M}_\mathrm{F}$ (Figure 3.3 **a**), the system is practically equivalent to a single S-F interface. Inside the ferromagnet, the FFLO state leads to a mixture of spatially oscillating singlet and $m = 0$ triplet components. These correlations are faced with the problem of populating spin-split Fermi surfaces, and therefore only last for atomically small distances. However, there is also singlet-triplet mixing in the S layer, as a result of spin-dependent phase shifts that occur during reflections from the F layer. Interestingly, these correlations can reach up to 10s of nm, as their characteristic length scale

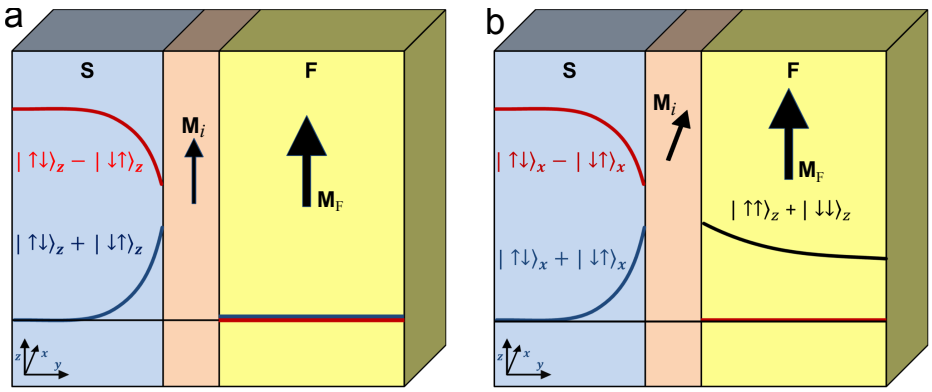

Figure 3.3: Generating equal-spin triplet pairs at S-F interface: long-range proximity effect. **a**, magnetization of the interface $\mathbf{M}_i$ and that of the F layer $\mathbf{M}_\mathrm{F}$ are aligned with z. Spin quantization axis for triplet-singlet mixing is z, and the correlations are suppressed in the F layer. **b**, if $\mathbf{M}_i \parallel x$, the $|\uparrow\downarrow\rangle_x + |\downarrow\uparrow\rangle_x$ triplet has zero spin-projection along x, but can decompose into $|\uparrow\uparrow\rangle_\mathrm{z}$ and $|\downarrow\downarrow\rangle_\mathrm{z}$ as we switch the quantization axis to z in F. The equal-spin pairs are not broken by the exchange field, leading to long-range proximity.

is defined by the size of the Cooper pairs i.e. the coherence length of the superconductor ξ_s. However, this triplet state cannot survive in the ferromagnet as it also has zero spin-projection along z, and therefore suffers the same fate as the FFLO phase.

Let us now consider the case where $\mathbf{M}_i$ makes an angle with $\mathbf{M}_\mathrm{F}$ (shown in Figure 3.3 **b**). For simplicity, we assume $\mathbf{M}_\mathrm{F}$ to align with the z-axis within the F layer, while $\mathbf{M}_i$ points along the x-axis. The spin-mixing that occurs in the S layer is therefore a result of the exchange field in the x-direction. In contrast to Figure 3.3 **a**, the spin quantization of the singlet-triplet mixture at the interface is now defined with respect to the x-axis. While the triplet state $|\uparrow\downarrow\rangle_\mathrm{x} + |\downarrow\uparrow\rangle_\mathrm{x}$ has zero spin-projection in x-direction, it can decompose to $|\uparrow\uparrow\rangle_\mathrm{z}$ and $|\downarrow\downarrow\rangle_\mathrm{z}$ pairs in the F layer. Due to their equal spins, such pairs do not "feel" the exchange field of the ferromagnet. These triplet correlations can therefore spread through the ferromagnet, just as singlet pairs do in a normal metal. By the same token, the characteristic decay length for equal-spin triplets is given by

$$\xi_\mathrm{f}^\mathrm{ESP} = \sqrt{\frac{\hbar D_\mathrm{f}}{k_\mathrm{B} T}} \tag{3.7}$$

which is equivalent to the expression for ξ_n (3.1). As a result, the typical length scale for equal-spin triplet Cooper pairs in a ferromagnet can exceed far beyond the value of ξ_f. For a strong ferromagnet such as Co, $\xi_\mathrm{f}^\mathrm{ESP}$ is in the order of 10s of nm, but it can also reach values as large as a micron in case of the half-metallic ferromagnet CrO_2. Furthermore, the amplitude of equal-spin pairing is proportional to the magnetic

non-collinearity at the interface. In the above example (Figure 3.3 **b**), we assumed the magnetization of the interface to be perpendicular to that of the F layer. This corresponds to the maximum amplitude of long-ranged triplets generated. Besides amplitude, the orientation of the magnets also determines the phase of the triplet correlations. This is discussed in Section 3.1.4 in connection with π- and φ-junctions.

Supercurrents (triplet as well as singlet) are generally studied in the context of a basic device known as the Josephson junction. It is therefore necessary to introduce the general Josephson effect before proceeding further with the discussion on triplet correlations in S-F hybrids.

3.1.3. JOSEPHSON EFFECT

The Josephson effect is concerned with the overlap of two macroscopic wavefunctions that are separated by some form of weak link. The concept is illustrated in Figure 3.4**a**, which shows two superconducting electrodes, each corresponding to a distinct wavefunction described by $\Psi_{l,r} = ne^{i\phi_{l,r}}$. Here n is the density of Cooper pairs, which we assume to be the same for the left (l) and right (r) electrodes, and $\phi_{l,r}$ corresponds to the macroscopic quantum phase of individual condensates. The two wavefunctions can extend over the weak link and couple with each other through proximity effect. On the other hand, Ψ_l and Ψ_r can have different phases, and in order to transfer Cooper pairs between the electrodes, phase coherence must be maintained. Josephson showed that the supercurrent across a junction is determined by this phase difference through

$$I = I_c \sin(\varphi) \tag{3.8}$$

where $\varphi = \phi_l - \phi_r$, and I_c is the maximum amount of supercurrent the junction can sustain. Below this value transport is dissipationless, and characterised with zero voltage V (i.e. resistance). The nonlinear current-voltage characteristic of a typical junction is shown in Figure 3.4**b**, where the system is biased with a d.c. current. The Josephson relation 3.8 also demonstrates an important distinction between superconductors and normal conductors. Conventional electronics are governed by the Ohm's law, which states that electrical current is driven by the voltage ($I \propto V$). In a superconducting circuit however, there is no potential difference ($V = 0$). Instead, the current is driven by the phase difference φ. What makes the macroscopic phase of fundamental importance is that it means electrical transport in a superconductor has a wave-like nature. This can be confirmed by the behaviour of a single Josephson junction in presence of a magnetic field. As shown in Figure 3.4 **c**, $I_c(B)$ follows a Fraunhofer "diffraction pattern", similar to that of a wave passing through a narrow slit. In analogy with optics, the total supercurrent that can flow in one direction is modulated by the spatial variations of the phase. The difference is that here the

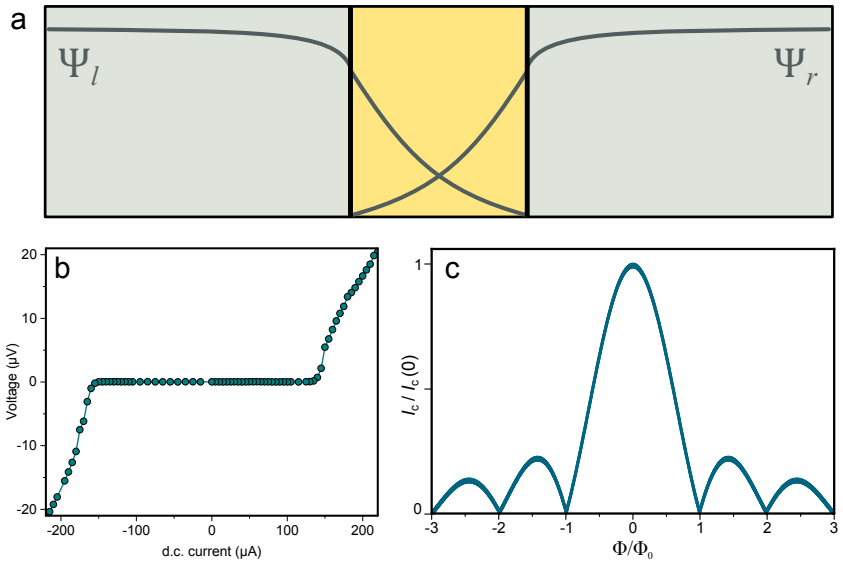

Figure 3.4: Josephson effect. **a**, schematic of a Josephson junction. A weak link (yellow) is proximized by the overlapping wavefunctions $\Psi_{l,r}$ of the superconducting electrodes. **b**, typical $I-V$ characteristic of Josephson junction. The plateau corresponds to the zero resistance (i.e. static phase). **c**, Fraunhofer pattern (simulated), representing the basic relation between critical current (normalised) and applied magnetic flux in a standard Josephson junction.

phase variation is introduced by the magnetic flux threading the junction Φ. Since flux can only enter a superconductor in quantised units, the supercurrent diffraction is described by

$$I_c(B) = I_c^{\max}\left|\frac{\sin\left(\frac{\pi\Phi}{\Phi_0}\right)}{\frac{\pi\Phi}{\Phi_0}}\right| \tag{3.9}$$

where $\Phi_0 = \hbar/2e$ is the magnetic flux quantum (fluxoid), and $I_c^{\max}$ is the maximum critical current of the junction.

In the same way ξ is the characteristic length for the amplitude of the order parameter, a characteristic length (λ) can be assigned to the phase of the order parameter. Hence, generally speaking, λ can be described as the length scale over which ϕ can vary. This definition of can be applied to any superconducting system, and is not limited to Josephson junctions.[4] Given that supercurrent is driven by the phase difference, λ is also the characteristic length for supercurrent amplitude. For instance, under an external magnetic field, the circulating currents inside a superconductor are restricted to a finite range. As the supercurrent amplitude decays over λ, so does the magnetic field, which is the reason for referring to λ as the penetration depth.

[4] Not to be confused with the λ_J, which is specific to Josephson junctions.

There are however multiple variations of λ, each applicable to a different system i.e. a bulk superconductor would correspond to a different λ than the one for a thin film or a Josephson barrier. The bottom line here is that the phase of the order parameter can only vary over a finite length scale, which is determined by λ. Also, as we describe in later chapters, external magnetic fields are not the only means of creating a phase difference.

3.1.4. LONG-RANGE TRIPLET SUPERCURRENTS

The theoretical developments on long-range proximity effects began by a series of consecutive papers in the beginning of 2000s [7–9]. In their pioneering work, Sebastián Bergeret, Anatoly Volkov and Konstantin Efetov studied S-F structures where the magnetization rotates near the interface. They showed such systems can produce equal-spin triplet amplitudes which can extend over long distances in the ferromagnet. More surprisingly however, was that they found these triplet correlations to have even-parity (s-wave) and odd-frequency. This was the same pairing state that Berezinskiĭ [10] had proposed in 1974 for superfluid ^{3}He, which later was found to be p-wave (even-frequency). This rather unexpected development had important symmetry implications. The realization of equal-spin pairing with s-wave symmetry meant the order parameter is robust against elastic scattering from non-magnetic impurities. Therefore, spin-polarized supercurrents can propagate through ordinary ferromagnetic films, even when transport is diffusive. This is to be distinguished from p-wave triplets (even frequency), which are restricted to clean materials [11].

A crucial aspect of the theory of the odd-frequency triplets was that it relied strongly on the presence of a certain type of magnetic inhomogeneity at the interface. It was clear that without this, spin-mixing could not produce the s-wave triplet correlations. This led to an on-going series of theoretical proposals for generating, and controlling, long-range triplet correlations in various S-F hybrid systems. The early theoretical studies considered the use of domain walls [7, 12–16] and spiral magnetic structures [17–20] as possible candidates for triplet spin-mixing. Sosnin *et al.* attempted to realise these ideas using the intrinsic helical magnetic phase of holmium [21]. The authors applied Andreev interferometry to investigate transport through a Ho wire ($50-150$ nm long) contacted by superconducting electrodes. They observed Φ_0-periodic conductance oscillations, which indicated phase-coherent superconducting transport through the Ho wire. A Josephson current however was not detected. The wires maintained appreciable resistance which, below a certain point, did not seem to decrease by lowering the temperature— indicating the junctions were most likely not fully proximized.

An important experimental evidence of long-range triplet supercurrent came in 2006, where Keizer *et al.* reported supercurrents through the half-metallic ferromag-

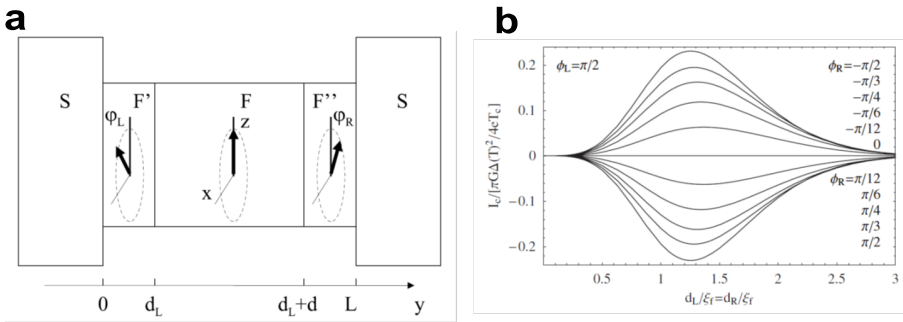

Figure 3.5: Generating long-range triplet current with a magnetic trilayer. **a** Schematic of an S/F'/F/F"/S junction. Arrows indicate the magnetic orientation of each layer. Magnetization of the middle F layer (thickness = d) is fixed along z, while F' and F" (thicknesses d_L and d_R) can rotate their magnetizations by φ_L and φ_R respectively. **b** Normalised I_c as a function of layer thickness d_L (d_R), plotted for various orientations of φ_R, while fixing $\varphi_L = \pi/2$. I_c amplitude is maximum for $\varphi_R = \pm\pi/2$ i.e. if F' and F" magnetizations are both perpendicular to the magnetization in F. Negative (positive) I_c corresponds to the π (zero) state. Taken from Ref. [30].

net CrO_2 [22]. They observed a finite supercurrent between NbTiN electrodes that were separated by over 300 nm on a CrO_2 film. Given the fully spin-polarized nature of CrO_2 (only one spin type has a conduction band, and the other is insulating) [23–28], this was a strong evidence of a long-range triplet component with equal-spin pairing of electrons. Their experiments however could not provide any information about the frequency of orbital symmetry of the correlations. As transport in the CrO_2 film may still be in the clean limit, where an odd-parity order parameter could survive, it was therefore not possible to determine whether the triplet pairing was of odd-frequency (s-wave) or odd-parity (p-wave) type. Furthermore, the results of Keizer *et al.* proved rather difficult to reproduce. It was only in 2010 that Anwar *et al.* succeeded in reproducing the effect using MoGe electrodes separated by 700 nm on CrO_2 film [29]. This was partly due to the difficulties in making transparent interfaces with CrO_2, which is metastable and reduces to Cr_2O_3 at room temperature. This forms an insulating layer, which needs to be carefully removed from the surface of CrO_2 before depositing any electrical contacts. The other difficulty however was the lack of control over magnetization at the interface with the CrO_2 films. As described in section 3.1.2, the presence of a certain magnetic inhomogeneity at the interface is crucial for generating long-range odd-frequency triplet pairing. However, the source of magnetic inhomogeneity in the early CrO_2 devices was rather ambiguous and difficult to control.

A major breakthrough was made in 2007 by Houzet and Buzdin who proposed a device structure to generate (and potentially control) triplet supercurrents in multilayer systems [30]. Their proposal was based on a Josephson junction where the weak link consisted of a ferromagnetic trilayer (S/F/'F/F"/S), where the magnetization of F'

and F" could be rotated with respect to F (see Figure 3.5 **a**). They showed that the amplitude of long-range triplet supercurrent is maximum if F' and F" are magnetized perpendicular to F, and vanishes if they are collinear (i.e. when F' and F" are either parallel or antiparallel to F). Equally important was that the relative alignment of the F' and F" also determined if the junction is in a 0 or π state. They showed that if the F' and F" are parallel, the junction has an intrinsic phase of $\varphi = \pi$ (i.e. is a π-junction), while in the antiparallel configuration $\varphi = 0$ (see Figure 3.5 **b**). Hence, in addition to controlling the amplitude of supercurrent, the magnetic orientation of the layers can be used to realise both 0 and π states in the same device. This was recently demonstrated in Ref. [31], where the phase of a triplet junction, with a multilayer weak link, could be switched between 0 and π by turning the magnetization of one layer by 180°.

Note that even before the emergence of long-range triplet devices, π-junctions had been realized by short-range proximity effect in thin (< 10 nm) and weakly spin-polarized ferromagnets. In such systems the crossover between 0 and π was usually achieved by carefully varying the thickness of the ferromagnet or, under very specific circumstances, by varying the temperature [5, 32]. In terms of device applications, neither of these options could match the robustness of a triplet junction, such as the one depicted in Figure 3.5. This led to a growing interest in the use of magnetic multilayers for singlet to triplet conversion. Shortly after, a series of experimental efforts succeeded in realizing this, and long-range triplet currents were found in a number of multilayer junctions — using different materials and device configurations.

As shown in Figure 3.5 singlet to triplet conversion with a multilayer requires non-collinear magnetization of the ferromagnets. In practice however, realising such magnetic configuration is by no means a trivial task. The difficulties arise from the fact that local interlayer coupling tends to favour parallel or antiparallel alignment of the magnetizations [5]. While interlayer exchange interactions can be regulated with nonmagnetic spacers, interlayer dipolar (magnetostatic) coupling has proven to be rather problematic. This has been a major hurdle for the controlled generation of triplet correlations, and has been the focus of intensive studies [33–37]

The individual groups which succeeded in generating long-range triplet currents, each had a distinct method to overcome this issue. Robinson *et al.* implemented the conical magnetic configuration of holmium to create non-collinearity with cobalt magnetization in Nb-Ho-Co-Ho-Nb nano-pillar junctions (see Figure 3.6 **a**,**b**) [38]. Meanwhile Khaire *et al.* developed a different approach using a synthetic antiferromagnetic interlayer (SAF) made of a Co-Ru-Co trilayer [39]. In this case, the exchange coupling through Ru leads to antiparallel alignment of magnetic domains in the adjacent Co layers, thereby suppressing their demagnetising fields. The SAF decouples the Co magnetization from the other ferromagnets in a S-F'-N-SAF-N-F'-S

[5] More on this in Section 3.2 where we examine multilayer systems with micromagnetic simulations

stack used in their devices (See Figure 3.6 **c**,**d**), allowing a magnetic non-collinearity to be present between Co and F' layers. The multilayer convertor was also implemented by Anwar *et al.* , where they extended their work on CrO_2 junctions [40]. Using MoGe-Ni(1.5 nm)-Cu(5 nm) electrodes, deposited on a CrO_2 film, they found critical currents that were about two orders of magnitude higher than their previous works. This was a strong indication of spin-mixing by magnetic misalignment, and consistent with the behaviour of odd-frequency triplets.

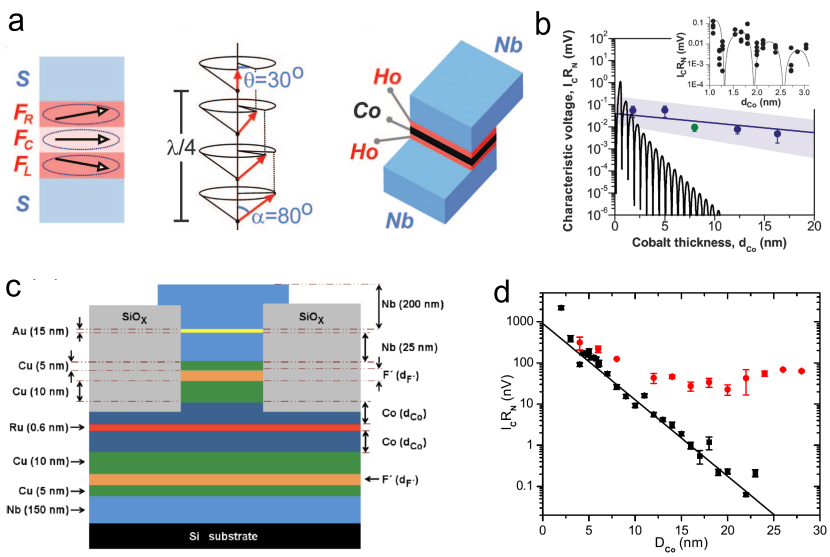

Figure 3.6: **a**, configuration of the Ho/Co/Ho trilayer used in Ref. [38], where the conical magnetic structure of Ho was used to inject long-range triplet correlations into Co. Magnetic moments of Ho (red arrows) rotate by $\theta = 30^\circ$ per atomic layer, leading to a spiral with a period of $\lambda \approx 3.4\ nm$. **b**, normalised I_c as a function of Co thickness. The oscillating curve is the simulated behaviour for short-range proximity, where I_c would be rapidly suppressed. Instead, the the measured I_c falls as if the Co barrier was nonmagnetic. Taken from Ref. [38]. **c**, schematic of the magnetic multilayer used for generating long-range triplet current in Ref [39]. Here, the magnetic "trilayer" consists of one (Co/Ru/Co) and two separate PdNi (4 nm) layers, shown here as F'. **d**, I_c as function of Co thickness for junction with (red circle) and without (black square) the F' layers. For the full trilayer, there is no appreciable decay of I_c for Co thicknesses up to 30 nm. Taken from Ref. [34].

Besides non-collinear multilayers, there is a growing number of proposals for generating and controlling triplet correlations which remain unexplored. A number of these ideas revolve around the use of spin "texture". This corresponds to systems where two; or all three components of magnetization (m_x, m_y, m_z) vary spatially in at least two dimensions. The spatial variation of the magnetization needs to take place over a certain length scale that is comparable to ξ_f. These conditions can be realised in the magnetic ordering of certain mesoscopic ferromagnets and magnetic domain walls.

3.2. MICROMAGNETIC SIMULATIONS

3.2.1. MICROMAGNETIC THEORY

The magnetic state of any given structure can be modelled by finding the state that corresponds to lowest free energy. The magnetic energy however consists of a number of discrete components. In systems described here, the most relevant energy terms are the exchange, anisotropy, demagnetizing (also called magnetostatic energy) and Zeeman. The total energy is then determined by the sum of all energy densities, integrated over the volume of a system.

$$E_{\text{tot}} = \int_V \left(\varepsilon_{\text{ex}} + \varepsilon_{\text{anis}} + \varepsilon_{\text{demag}} + \varepsilon_{\text{z}}\right) dV \tag{3.10}$$

Consider calculating this for the relatively simple 3-dimentional system shown in Figure 3.7 **b**. On the atomic scale the exchange interaction aligns the neighbouring magnetic moments, while on a larger scale the demagnetizing term forces the magnetic moments to align with the sample boundaries to minimize stray fields. Nevertheless, depending on the exact geometry, there will be a presence of demagnetizing fields which results in dipole interactions between the adjacent ferromagnets. In addition to these, there are also the contributions from magnetic anisotropy, which can be different for each material, and external magnetic fields.

There is no doubt that an analytical approach to this problem would be overwhelmingly complex and tedious. Fortunately however, the micromagnetic theory allows us to implement numerical methods that are far more effective. Instead of considering individual magnetic moments, the micromagnetic theory postulates that magnetization (i.e. magnetic moments per unit volume) is a spatially continuous function $\mathbf{M}(\mathbf{r})$ [41]. Based on this approximation a system can be divided into discrete units

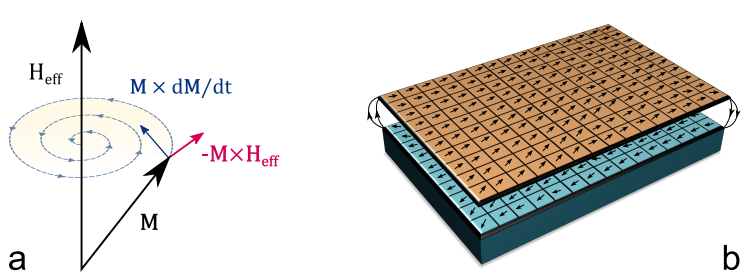

Figure 3.7: **a** Precession (red) and damping (blue) of magnetization vector **M** under an effective magnetic field $\mathbf{H}_{\text{eff}}$, as described by LLG 3.12. **b** Micromagnetic theory applied to a magnetic multilayer. System is divided into discrete cells, where each unit can be assigned with a magnetization vector **m**, which is subject to a local effective field. This also includes stray fields, which lead to interlayer dipolar coupling (shown as solid lines connecting the layers).

of finite dimensions. Each segment is described by a unit magnetization vector, and experiences a local effective field $\mathbf{H}_{\text{eff}}(\mathbf{r})$ given by

$$\begin{aligned} \varepsilon_{\text{tot}} &= -\int \mu_0 \mathbf{H}_{\text{eff}}(\mathbf{r}).\mathbf{M}(\mathbf{r}) d^3 r \\ \mathbf{H}_{\text{eff}}(\mathbf{r}) &= -\frac{1}{\mu_0} \nabla_{\mathbf{M}} \varepsilon_{\text{tot}} \end{aligned} \tag{3.11}$$

Hence, all the components of magnetic energy are now elegantly represented by single magnetic field. This enables us to obtain the *dynamic* magnetization of each cell by solving the time-dependent Landau-Lifshitz-Gilbert (LLG) equation

$$\frac{d\mathbf{M}}{dt} = \gamma \mu_0 \mathbf{M} \times \mathbf{H} - \frac{\alpha}{M_s} \mathbf{M} \times \frac{d\mathbf{M}}{dt} \tag{3.12}$$

where γ is the gyromagnetic ratio and α is the Gilbert damping parameter. Here, the first term describes the procession of $\mathbf{M}$ in a local effective field, while the second term corresponds to dissipation (see Figure 3.7 **a**). Solving the LLG for every cell, one by one, over the entire system, and in many iterations, allows each unit of magnetization to interact with its neighbouring cells and reconfigure its direction over time. The overall magnetization therefore "evolves" by minimizing its total energy, until the system relaxes into a minimum in the free energy landscape.

3.2.2. SIMULATIONS

The simulations are carried out using the object-oriented micromagnetic framework (OOMMF) software package [42], which applies finite element techniques to the differential LLG equation 3.12. It works discretising a given object over a small mesh, where at each point LLG is solved and integrated using Runge-Kutta algorithms [43] to calculate the magnetization. It is possible to define the anisotropy and initial magnetization of individual cells, and vary an applied field over the entire object. It also calculates the demagnetizing fields using Fast-Fourier-transformations [44, 45].

The equilibrium state can be found by monitoring the rate at which magnetization changes its direction. In the Runge-Kutta evolver this is represented by the parameter $|d\mathbf{m}/dt|_{\text{max}}$, which has units of degrees per nanosecond, where $\mathbf{m}$ is the unit magnetization direction. Preferably, the value of $d\mathbf{m}/dt$ should be as small as possible. Depending on the individual system, we set $|d\mathbf{m}/dt|_{\text{max}} < 0.1$, which means the simulation will stop if the maximum magnetization derivative of each cell is less than 0.1 degrees per nanosecond. A typical simulation can take somewhere between

10^5 to 10^6 iterations and, in some cases, may not converge at all. Even with the high-performance clusters of 48 - 64 cores, this could correspond to days, and sometimes weeks, of computational time. It is therefore critical to choose our computational parameters carefully, and monitor the evolution of magnetization at every stage to ensure the simulation is progressing in consistent manner.

The mesh size is one of the crucial parameter which should be chosen carefully. In most cases, but not always, a smaller cell size provides a more realistic representation of a given object. One the other hand, increasing the number of cells could overwhelmingly slow down the simulation. As a rule, this value needs to be of the order of the exchange length, given by

$$l_{\text{ex}} = \sqrt{\frac{2A}{\mu_0 M_s^2}} \tag{3.13}$$

where A is the exchange stiffness in units of J/m. In general, l_{ex} can be described as the characteristic length scale over which the magnetic moments can change their alignment in presence of an exchange field. For strong ferromagnets this value is in the order of 5 nm, which is also the standard mesh size used in our simulations. Another important parameter for convergence is the damping constant α in LLG 3.12. This can be interpreted as a measure of how quickly the field and magnetization align (see Figure 3.7 **a**). As we are mainly interested in the equilibrium state, we set $\alpha = 0.5$ for rapid convergence. Using smaller values would substantially increase the simulation time and hardly affect the equilibrium state.

As stated earlier, OOMMF allows defining the magnetic anisotropy of the individual cells. This can be set to represent the appropriate magnetocrystalline anisotropies (e.g. uniaxial for cobalt and cubic for nickel etc.). However, with the exception of CrO_2, the ferromagnetic films used in this work are prepared by sputter deposition on amorphous SiO_2 substrates. To represent the polycrystalline nature of these films, where each grain has an arbitrary orientation, we use a random vector field to set the principal axes of each unit cell. Since magnetocrystalline anisotropy is now smeared out in all directions, shape anisotropy (the minimization of the stray fields) becomes the dominant factor. For the sputtered films of Co and Ni used here, this leads to an in-plane magnetisation with no specific easy axes. This anisotropy was also confirmed by our ferromagnetic resonance (FMR) and SQUID magnetometry [46].

Crystallinity and geometry however are not the only factors which can result in a magnetic anisotropy. In some cases, certain deposition conditions can also result in a preferred magnetic direction. An example of this is the permalloy (Py) films deposited in presence of a finite magnetic field, which can develop an out-of-plane anisotropy [47]. In this case, experiments were necessary to determine the

anisotropy, which we could then use as input in our simulations — and model the individual domain structures found in the patterned Py films.

In addition to anisotropy, simulations also require the exchange stiffness A and saturation magnetization M_s. These values are provided in the OOMMF database (commonly used in literature). We found the reported values for M_s to be in close agreement with the ones obtained from our FMR and SQUID measurements.

3.2.3. MULTILAYER PLANAR JUNCTIONS

In this section we describe how micromagnetic simulations can be applied to multilayers to design optimal planar junctions with long-range triplet current (see Figure 3.8). Ideally we need a stable magnetic non-collinearity (MNC) between F and F' layers, which can also be modified and controlled by applying external magnetic fields. For our devices, we will be using Ni (1.5nm) and Co (50-60 nm) as the F and F' respectively. The ferromagnets are separated by a Cu(5 nm) layer to avoid interlayer exchange coupling. The thickness of the Ni layer was found to be optimal for triplet generation in similar multilayer systems [34, 48].

We begin by examining a bar-shaped device, which is the standard configuration of planar Josephson junctions. This is typically realised a rectangular multilayer strip, where the superconducting layer can in some way be discontinued to create a weak link. In our devices, this would mean opening a gap in the top Nb-Ni-Cu layers, leaving only Co in the weak link.

Figure 3.9 **a** shows the plane view of Co and Ni magnetizations at zero field, obtained from 3-D OOMMF simulations. The pixel colour scheme, red-white-blue, scales with the magnetization along x. In order to estimate the MNC, for each cell at the top of the Co layer we determine the angle θ between its magnetization vector and that of the Ni cell above (see Figure 3.9 **b**). From this we can extract a MNC profile over the entire structure, shown in Figure 3.9 **c**. We observe a pronounced cou-

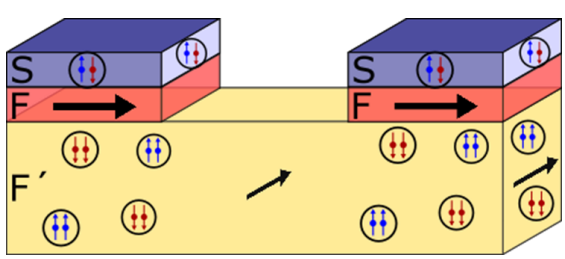

Figure 3.8: Schematic representation of a planar multilayer junction. To generate long-range triplet current, F and F' layers must have non-collinear magnetizations.

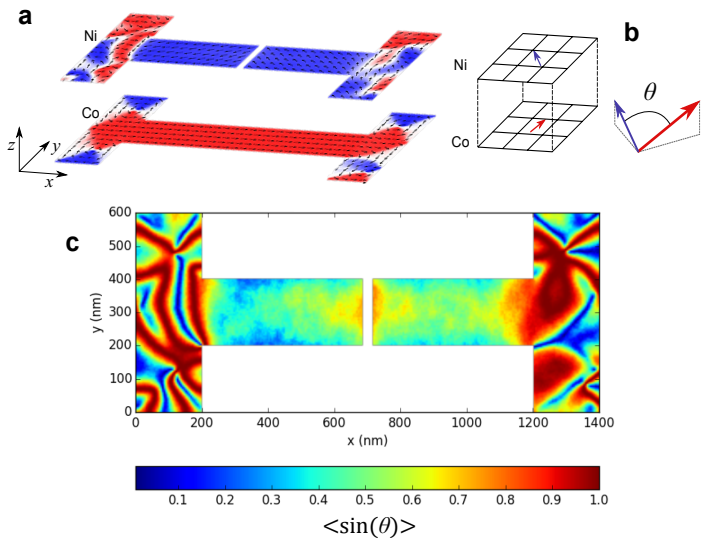

Figure 3.9: **a**, Plane view magnetization of Co(45 nm) and Ni (2 nm) at zero applied field, obtained from 3D OOMMF simulations. The gap in Ni corresponds to the location of weak link is. The pixel colour scheme, red-white-blue, scales with the magnetization along x. **b** represents our method to obtain the MNC profile shown in **c**. For each cell at the top of the Co layer, θ is determined by the angle between the magnetization vector of Co and that of the Ni cell above. $< \sin(\theta) >$ is defined as the absolute value of the outer product between the Co and Ni magnetization vectors (note that the colour scheme is different from **a**).

pling between the ferromagnets, with an antiparallel configuration being the magnetic ground state. This has a detrimental effect on the MNC in the junction, which is clearly visible in Figure 3.9 **c**.

To better understand the nature of the interlayer interactions we performed film dependent simulations, where the magnetizations are reversed by sweeping an in-plane field. An example of this is shown in Figure 3.10. Initially, both Co and Ni are fully magnetized by a large magnetic field applied in $-x$ direction. As we sweep the field towards zero, the Co magnetization remains relatively unchanged. Meanwhile, Ni begins to reverse its magnetization around -100 mT — which switches its direction to $+x$ already at $\mu_0 H = -15$ mT. This is a result of local dipole fields from Co, which begin to dominate the effective field acting on Ni when the applied field is not substantial. The antiparallel configuration continues up to $\mu_0 H = 65$ mT, at which point Co reverses its magnetization to $+x$. While we observe some adjustments in the Ni magnetization, for the most part it remains along $+x$, and parallel to Co.

We found the interlayer dipole coupling to be consistently present in all bar-shaped junctions studied, even when the boundaries were extended to reduce the effects of stray fields Figure 3.9 **c**. In such systems only the parallel and antiparallel magnetic configurations are stable, both equally undesirable for generating triplet currents.

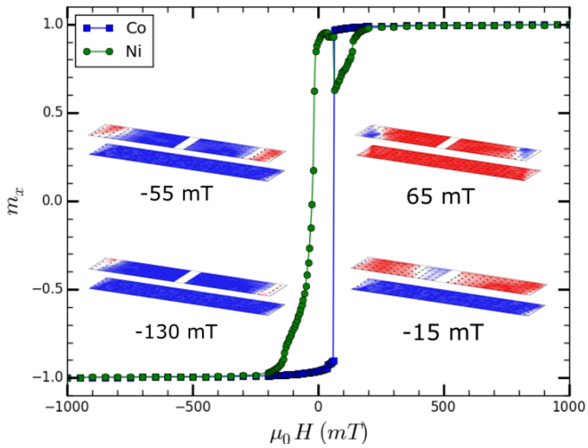

Figure 3.10: Simulation of the magnetization reversal in a bar-shaped Co(45 nm) / Ni(1.5 nm) bilayer. The field is swept from −1 T to 1 T, taking 5 mT field steps within ± − 200 mT. Individual magnetizations of Co (blue squares) and Ni (green circles) layers are plotted separately. The insets show snap-shots of Co (bottom) and Ni (top) at different stages of magnetization reversal.

Even if the ferromagnets could somehow be decoupled and form a non-collinear state, their stray fields could still be a serious issue for the junction. Most SFS junctions are known to suffer from stochastic self-fields which lead to distorted and/or shifted interference patterns, and other unwanted irregularities [33–37].

In order to resolve these issues altogether, we implemented a disk-shaped design to create a vortex magnetization in the Co layer. As shown in Figure 3.11, the curled structure of a ferromagnetic vortex is highly effective in minimizing stray fields. Furthermore, the vortex magnetization is fully in-plane except for the core, where it sharply turns out of plane. The core has a local magnetization of $\mu_0 M_s \approx 1.8$ T. Despite its large value, due to the small radius of the core (5 – 10 nm) [49], this field corresponds to a relatively small flux $\approx 10 - 20\ \%\Phi_0$.

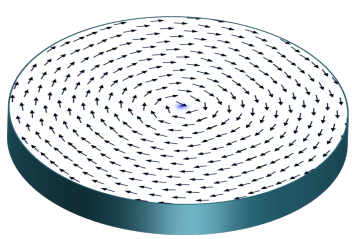

Figure 3.11: **Ferromagnetic vortex**. Simulated magnetic pattern of a 50 nm thick Co disk with 1 μm diameter. At the vortex core the magnetic moments turn sharply out-of-plane (blue pixels).

The position of the core can be varied in a coherent manner using in-plane magnetic fields. Moreover, the magnetic anomaly at the core is expected to suppress long-range triplet correlations [50]. We therefore can utilize the core as the means to gain dynamic control over the distribution of triplet current. This concept is described in detail in Chapters 4 and 5.

3.3. CrO_2 NANOWIRES

In this section we present an alternative to the S/F'/F/F"/S trilayer, the conventional device configuration for generating triplet supercurrent. This is realised by implementing the domain structure of mesoscopic CrO_2 crystals. We begin by describing the micromagnetic pattern of various CrO_2 nanowires.

3.3.1. MAGNETIC PATTERNS

The magnetic structure of a crystalline CrO_2 wire is a product of magnetocrystalline and shape anisotropies. The former is a uniaxial anisotropy which favours the magnetization to align with the [001] axis of the crystal, while the latter serves to minimise the demagnetizing energy by aligning the magnetic moments along the wire (i.e. the long side of the structure). These two terms can be exploited to obtain widely different magnetic states in CrO_2. We realise this with the help of selective area growth, where a SiO_x mask, deposited on a TiO (100) substrate, can be used to define the shape and orientation of individual CrO_2 crystals (see Figure 3.12 **a**). Sample prepration and the growth of crystalline CrO_2 wires are described in Ref. [51].

If grown along [001], the wire would be aligned with the magnetic easy axis of the crystal. In this case both anisotropies favour the magnetization to lie parallel to the wire. When a wire is sufficiently narrow ($w \lesssim 2$ μm), it would have a highly uniform magnetization where $M \parallel [001]$. In such systems, domain walls are typically scarce, since a transverse component of magnetization would be unfavourable by both anisotropies. This uniform magnetic structure has been utilized in some of our wire CrO_2 wire junctions to create a non-collinear magnetization with a Ni layer at the interface with the superconducting electrodes, which were deposited on the wire (perpendicular to its axis) [51].

If a is wire grown along [010], which is the hard axis of CrO_2, its magnetic structure will be entirely different. In this case, shape anisotropy prefers the magnetization to lie along the wire ($M \parallel [010]$), while the magnetocrystalline anisotropy favours

* The work presented in this section is to be submitted for publication.

Author contributions: samples were prepared by Amrita Singh. Kaveh Lahabi and Louis Maduro did the micromagnetic simulations. Transport measurements were carried out by Amrita Singh and Kaveh Lahabi. Jan Aarts supervised the project.

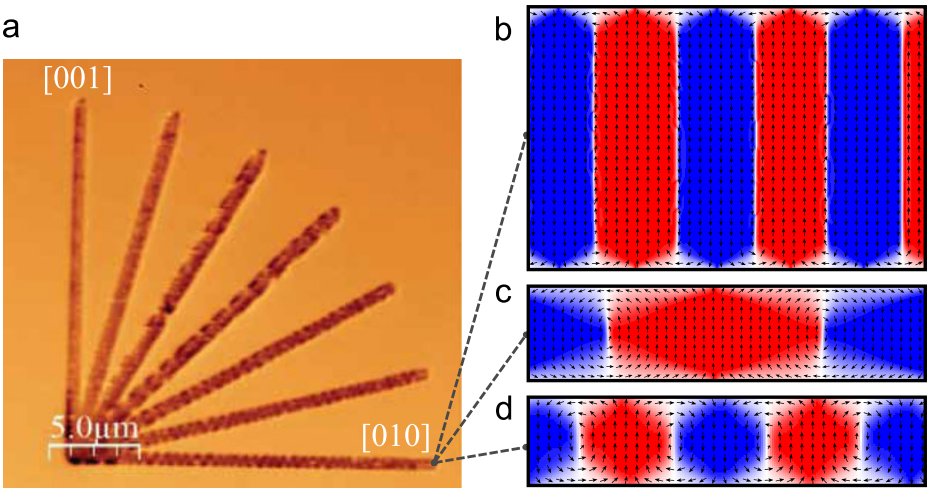

Figure 3.12: Magnetic patterns of CrO_2 crystals: **a** Magnetic force microscopy images of CrO_2 bars, grown along various directions [51]. **b**, **c** and **d** show the micromagnetic simulations for the 2 μm, 0.5 nm and 200 nm wide wires, respectively, grown along [010]. The pixel colour scheme, red-white-blue, scales with the (positive-zero-negative) magnetization along the easy axis of the crystal, which is transverse to the wire. Note that **b**, **c** and **d** correspond to different magnifications (wires in **c** and **d** are enlarged for clarity). In all simulations presented here, we set the wires to be 10 μm long and 104 nm thick. The cell size is (8 nm× 8 nm× 8 nm) for the 2 μm wide wire, and (5 nm× 5 nm× 5 nm) for the rest.

the magnetization to be perpendicular to it. The resulting magnetic pattern would then be a compromise, corresponding to their relative energies. While the crystalline anisotropy maintains a fixed value (2.7×10^4 J/m^3), the shape anisotropy can be tuned by varying the lateral dimensions of the bar.

Figure 3.12 **b-d** present the simulated magnetizations for bars of various widths, grown along the hard axis of CrO_2. In the 2 μ m wide bar (3.12 **b**), we observe stripe-like domains where magnetization alternates transverse to wire. Within each domain the magnetization is relatively uniform except for the regions near the edges of the wire, where magnetic moments are rotated to reverse the magnetization between adjacent domains. This spatially continuous rotation of magnetization is a consequence of the shape anisotropy, whose role to minimize dipole (stray) fields by turning the magnetic moments parallel to the surface of the bar. The shape anisotropy becomes more dominant by reducing the width of the bar. This leads to the emergence of an array of magnetic vortices in the 500 nm and 200 nm wide wires.

A vortex is characterised by two independent parameters: chirality, defined by the in-plane winding of magnetization (left or right), and polarity, set by the out-of-plane magnetization (up or down) located of the vortex core. Usually the vortices in ferromagnetic nanowires are isolated or, in certain circumstances, apear as pairs (see for example Refs. [52, 53]). More importantly, in almost every case they are a form

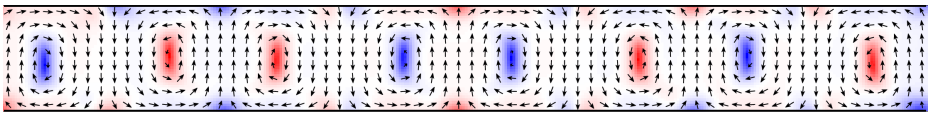

Figure 3.13: Simulated magnetic pattern of a 200 nm wide CrO_2 wire grown along [010]. The pixel colour scheme, red-white-blue, scales with the out-of-plane magnetization. The wire hosts a series of magnetic vortices with well-defined cores. The adjacent vortices have opposite chiralities.

of domain wall: separating two larger segments with uniform magnetizations. Interestingly however, here we observe a continuous array of adjacent vortices (see Figure 3.13). Unlike the stripe domains in the 2 μm wide bar (Figure 3.12 **b**), there is no clear distinction between a domain and a domain wall.[6]

This unusual state leads to a particular type of magnetization reversal which, to the best of our knowledge, has so far has been exclusive to magnetic disks [7]. These systems are characterized by a vortex core that can be displaced in a highly coherent and reversible manner, with no remnant magnetization. This results in a peculiar type of hysteresis loop, as shown in Figure 3.14.

The simulations in Figure 3.14 describe the magnetization reversal of a 5 μm$\times$200 nm CrO_2 bar, grown along the hard magnetic axis of the crystal. It also illustrates the magnetization patterns at various stages of the reversal. We begin by magnetizing the sample with a large magnetic field, applied in the $-y$ direction, which is transverse to the wire, and parallel to the easy axis of CrO_2 ($y \parallel [001]$). At **A** the wire is uniformly magnetized by the applied field. As we reduce the field, magnetic moments begin to align themselves with the sides of the wire, and magnetization begins to buckle. This trend continues up to **B**, after which point the pattern breaks down into a series of vortices distributed along the wire. At zero field (**C**) we find the vortices to be uniformly spaced. This results in zero remnant magnetization, since m_y has the same magnitude in $\pm y$. As we switch the field direction (**D**), a $+y$ magnetization begins to develop by displacing vortices along the wire (perpendicular to the applied field). By increasing the field, one or two vortices are driven out from the ends of the wire. The rest however end up as pairs, and are locked in to each other. This is because of the opposite chirality of adjacent vortices, which drives in them in different directions under the applied field. The motion of each vortex is therefore blocked by one of its neighbours, travelling in the opposite direction. As magnetization grows, vortex displacement begins to halt as the pairs are pushed against each other. This trend continues until they cannot get any closer to each other (**E**), at which point they vanish by spontaneously switching their magnetization.

[6] Note that we also found no vortex cores in the 2 μm wide bar.

[7] Here, we have also included the wires where multiple vortices can be stacked on top of each other [54, 55].

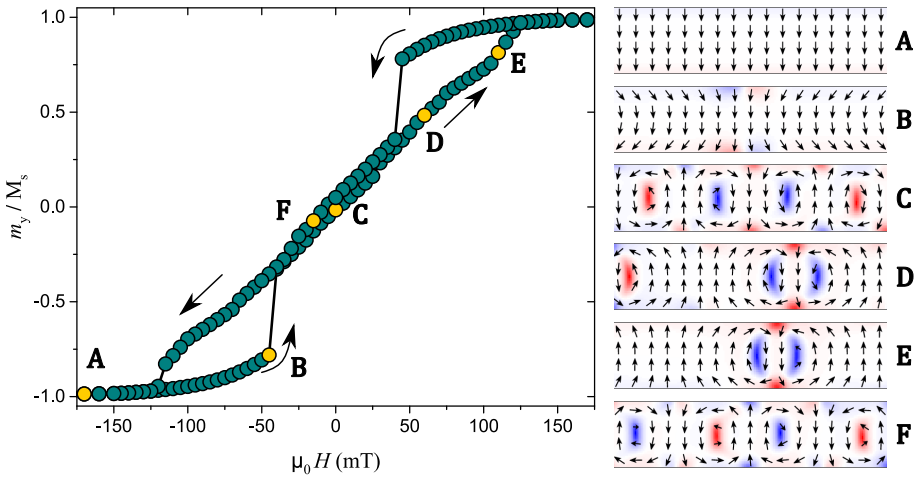

Figure 3.14: The simulated $M-H$ loop of a 200 nm wide wire, together with the magnetization patterns at various stages of vortex revesal.

As we magnetize the wire along $+y$ and bring the field back to zero, the magnetization goes through the equivalents of **A** and **B**. Lastly, at **F** we see a similar pattern as **C**. Even though the system was fully magnetized in the opposite direction, there is no sign of a remnant magnetization when we compare **F** with **C**.

In a magnetic disk, the field would push the vortex core (in a perpendicular direction) to one side of the disk, where it begins to slow down as it approaches the edge. This continues until the vortex cannot get any closer to the edge and vanishes in a single transition. Hence, vortex displacement is restricted solely by the geometry of the disk and its physical boundaries. In a wire however, there are no geometrical restrictions to stop a vortex from moving along its axis, which is why (domain wall) vortices in a typical ferromagnetic wire yield an entirely different type of magnetization reversal. Remarkably, here we find vortex chirality to play the role of sample boundary: the motion of a vortex is stopped by one of its adjacent vortices, as it would have been by the edge of a disk.

Note also that there is no particular relation between the polarity and/or the chirality of vortices in **F** and **C**. This is because the symmetries of the reversal process described above; do not favour a particular chirality or polarity over the other. The two parameters are therefore nondeterministic during a magnetization reversal.

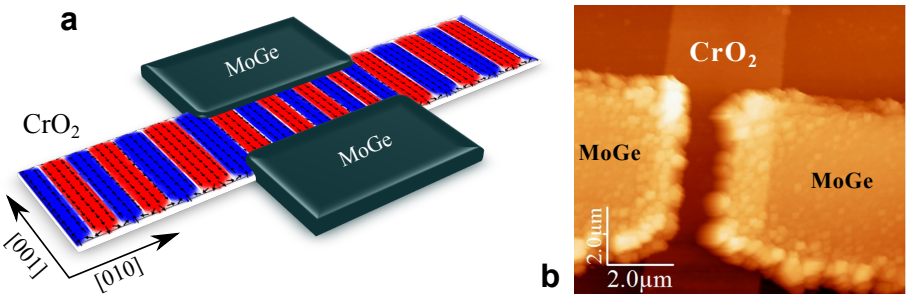

Figure 3.15: **a**, schematic of a transverse junction where the magnetic barrier consists of a single 2 μm wide CrO_2 bar with stripe domains. The pixel colour scheme, red-white-blue, scales with magnetization along [001]. **b**, scanning force microscopy image of the junction used in transport measurements of Figure 3.16. The superconducting MoGe electrodes contact the CrO_2 wire on both sides.

3.3.2. GENERATING LONG-RANGE TRIPLETS WITH MAGNETIC PATTERN

In addition to non-collinear multilayers, it has been proposed that long-range triplet correlations can also be generated by the magnetic pattern of a single ferromagnet [50, 56]. We demonstrate this in planar Josephson junctions, where the superconducting electrodes (MoGe) are deposited on the sides of a 2μm CrO_2 nanowire, as shown in Figure 3.15. Note that in this configuration; the transport direction is perpendicular to the axis of the wire. Here, the triplet correlations are generated by the exchange field gradient present on the sides of the wire with stripe domains. Although the contacts are separated by ≈ 500 nm, we a observe substantial critical current. At 2 K the supercurrent density is close to 4×10^9 A/m^2, see Figure 3.16 **a**.

At zero field, the system is in equilibrium. The stripes are about 500 nm wide and equally spaced, and the supercurrent is at its maximum. For the 2 μm wide bar however, our simulations indicate that the stripes can be modified by applying a relatively small in-plane field along the easy axis of CrO_2 (μ_0H ∥ [001]). They show that as we sweep the field from zero, the domains that are aligned with field direction (i.e. red stripes when the field is positive and blue stripes for negative fields) begin to increase in size, while the opposite domains shrink (see Figure 3.16 **a**). Taking field steps of 2 mT in our simulation, we find all domains to be magnetized by the field at 26 mT. This state corresponds to a relatively uniform magnetization with substantially less exchange field gradient, corresponding to minimum triplet generation. This is also supported by the transport measurements where we find no critical current above 20 mT. The reason for supercurrent vanishing even below the switching field is addressed below. First however, we make a note that the junction is relatively robust against out-of-plane fields. Even at fields as high as 600 mT the critical current maintains a finite value. This is because the stripe domains continue to be present until the bar is magnetized out-of-plane, and that requires substantially higher fields.

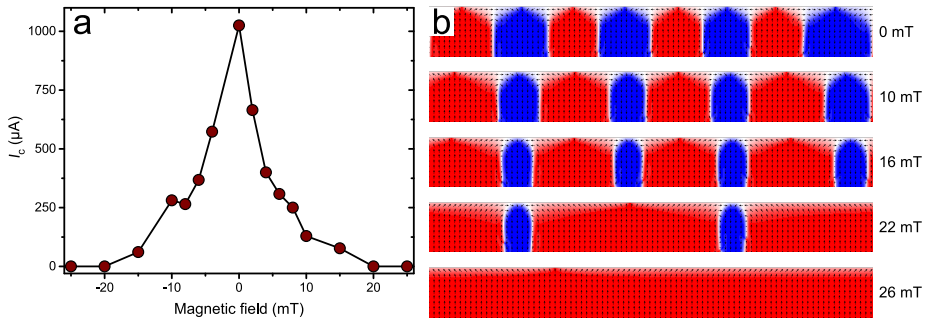

Figure 3.16: **a**, I_c measured as a function magnetic field, applied in the [001] direction i.e. along the stripe domains ($H \parallel I$). **b** , micromagnetic simulations for different applied fields, showing the magnetic pattern at the *edge* of the 2 μm-wide bar (full width shown in Figure 3.12 **b**), where the superconducting MoGe electrodes make contact with the CrO_2 wire. Red and blue correspond to parallel and antiparallel magnetizations, with respect to the direction of applied field.

It is evident that the junction transport strongly depends on the magnetic inhomogeneity – which is a key ingredient in generating long-range triplet correlations. For junctions with a single ferromagnetic barrier, spin-mixing is commonly associated with the exchange field gradient that is present at the magnetic domain walls (DWs). In our system however, the rotation of magnetization near the edges of the wire are arguably just as relevant (if not more) than the actual DWs.

The simulations show that magnetizing the sample would increase the size of one domain type over the other (e.g. red over blue or vice versa in Figure 3.16 b). The actual number of DWs however remains constant over a 3 μm-long segment of the wire (corresponding to the length of superconducting electrodes) up to 22 mT, where the minority domains begin to vanish by abruptly switching their magnetization from parallel to antiparallel to the field. Similarly, for small fields, there are no drastic changes in the overall magnetic texture of the wire. As shown in Figure 3.16 b), increasing the field to 10 mT barely changes the rotating magnetization pattern that appears near the edges. Hence, the rapid suppression of critical current cannot be entirely due to the lack of magnetic inhomogeneity for triplet generation. To appreciate the full picture, we consider what happens when we break the symmetry of parallel and antiparallel domains.

Unlike the 500 nm and 200 nm wide bars shown in Figure 3.12 **b**, the 2 μm bar does not contain magnetic vortices. While the stripe domains have may have chirality, there are no vortex cores with out-of-plane magnetization. Instead, we observe in-plane magnetic dipoles that form near the edge, in between the DWS. In equilibrium, the adjacent domains produce equal and opposite dipole fields, which cancel each other out over a few microns. However, applying a relatively small in-plane field can tip this balance by making one type of domain slightly larger than the other one. This

leads to an effective local field which induces additional screening currents in the superconducting electrodes, which in turn lead to the suppression of critical current.

The upshot here is that micromagnetic simulations can be implemented to design a wide range of magnetic hybrids which can generate and control long-range triplet supercurrent. In the above example, the simulations were used to obtain detailed description of the local magnetization texture in a variety of CrO_2 structures. We showed that by making basic adjustments to the dimensions of a simple wire bar we can extract widely different magnetic states. Subsequently, the well-defined stripe domains of a 2 μm wide bar were used to inject high supercurrent densities in CrO_2, without the need for extra magnetic layers. Reducing the problem to a single ferromagnet plays a significant role in our ability to control the triplet current. Utilizing the robust nature of magnetization reversal in for these particular dimensions enables us to switch off all supercurrent with only a few mTs — which is a highly practical field range for device applications. It is also worth noting that the coercive field of the CrO_2 nanowires could be significantly enhanced by reducing their width.

We note that a vortex pattern, such as the one shown in Figure 3.13 should also be capable of generating triplet currents [50, 56]. This is the focus of Chapter 5, where we demonstrate how the exchange field gradient in a ferromagnetic disk can induce long-range triplet correlations in cobalt. Combining the exceptionally high supercurrent densities in crystalline CrO_2 wires with the coherent motion of magnetic vortices would offer a rich platform to study triplet Coopers in the nonequilibrium setting, which is necessary for magnetization dynamics and spin-transfer torque. This system becomes even more intersting if we consider the possibility of storing information (bits) with the polarity and chirality of individual vortices.

REFERENCES

[1] T. Klapwijk. Proximity effect from an Andreev perspective. *Journal of Superconductivity*, 17(5):593–611, 2004.

[2] C. W. Beenakker. Random-matrix theory of quantum transport. *Reviews of Modern Physics*, 69(3):731, 1997.

[3] P. Fulde and R. A. Ferrell. Superconductivity in a strong spin-exchange field. *Physical Review*, 135(3A):A550, 1964.

[4] A. Larkin and I. Ovchinnikov. Inhomogeneous state of superconductors (production of superconducting state in ferromagnet with Fermi surfaces, examining Green function). *Soviet Physics-JETP*, 20:762–769, 1965.

[5] A. I. Buzdin. Proximity effects in superconductor-ferromagnet heterostructures. *Reviews of Modern Physics*, 77(3):935, 2005.

[6] M. Eschrig. Spin-polarized supercurrents for spintronics: a review of current progress. *Reports on Progress in Physics*, 78(10):104501, 2015.

[7] F. Bergeret, A. Volkov, and K. Efetov. Long-range proximity effects in superconductor-ferromagnet structures. *Physical Review Letters*, 86(18):4096, 2001.

[8] A. Kadigrobov, R. Shekhter, and M. Jonson. Quantum spin fluctuations as a source of long-range proximity effects in diffusive ferromagnet-superconductor structures. *EPL (EuroPhysics Letters)*, 54(3):394, 2001.

[9] F. Bergeret, A. F. Volkov, and K. B. Efetov. Odd triplet superconductivity and related phenomena in superconductor-ferromagnet structures. *Reviews of Modern Physics*, 77(4):1321, 2005.

[10] V. Berezinskiĭ. New model of the anisotropic phase of superfluid ^{3}He. *JETP Letters*, 20(9):287–289, 1974.

[11] M. Eschrig, J. Kopu, J. Cuevas, and G. Schön. Theory of half-metal/superconductor heterostructures. *Physical Review Letters*, 90(13):137003, 2003.

[12] A. Konstandin, J. Kopu, and M. Eschrig. Superconducting proximity effect through a magnetic domain wall. *Physical Review B*, 72(14):140501, 2005.

[13] A. Volkov, A. Anishchanka, and K. Efetov. Odd triplet superconductivity in a superconductor/ferromagnet system with a spiral magnetic structure. *Physical Review B*, 73(10):104412, 2006.

[14] A. Volkov and K. Efetov. Odd triplet superconductivity in a superconductor/ferromagnet structure with a narrow domain wall. *Physical Review B*, 78(2):024519, 2008.

[15] A. Volkov, Y. V. Fominov, and K. Efetov. Long-range odd triplet superconductivity in superconductor-ferromagnet structures with Néel walls. *Physical Review B*, 72(18):184504, 2005.

[16] Y. V. Fominov, A. Volkov, and K. Efetov. Josephson effect due to the long-range odd-frequency triplet superconductivity in SFS junctions with Néel domain walls. *Physical Review B*, 75(10):104509, 2007.

[17] M. Alidoust and J. Linder. Spin-triplet supercurrent through inhomogeneous ferromagnetic trilayers. *Physical Review B*, 82(22):224504, 2010.

[18] C. Wu, O. T. Valls, and K. Halterman. Reentrant superconducting phase in conical-ferromagnet–superconductor nanostructures. *Physical Review Letters*, 108(11):117005, 2012.

[19] C. Wu, O. T. Valls, and K. Halterman. Proximity effects in conical-ferromagnet/superconductor bilayers. *Physical Review B*, 86(18):184517, 2012.

[20] J. Linder, T. Yokoyama, and A. Sudbø. Theory of superconducting and magnetic proximity effect in S/F structures with inhomogeneous magnetization textures and spin-active interfaces. *Physical Review B*, 79(5):054523, 2009.

[21] I. Sosnin, H. Cho, V. Petrashov, and A. Volkov. Superconducting phase coherent electron transport in proximity conical ferromagnets. *Physical Review Letters*, 96(15):157002, 2006.

[22] R. Keizer, S. Goennenwein, T. Klapwijk, G. Miao, G. Xiao, and A. Gupta. A spin triplet supercurrent through the half-metallic ferromagnet CrO_2. *Nature*, 439(7078):825, 2006.

[23] K. Schwarz. CrO_2 predicted as a half-metallic ferromagnet. *Journal of Physics F: Metal Physics*, 16(9):L211, 1986.

[24] J. Coey and M. Venkatesan. Half-metallic ferromagnetism: Example of CrO_2. *Journal of Applied Physics*, 91(10):8345–8350, 2002.

[25] S. P. Lewis, P. B. Allen, and T. Sasaki. Band structure and transport properties of CrO_2. *Physical Review B*, 55(16):10253, 1997.

[26] R. Soulen, J. Byers, M. Osofsky, B. Nadgorny, T. Ambrose, S. Cheng, P. R. Broussard, C. Tanaka, J. Nowak, J. Moodera, et al. Measuring the spin polarization of a metal with a superconducting point contact. *Science*, 282(5386):85–88, 1998.

[27] W. DeSisto, P. Broussard, T. Ambrose, B. Nadgorny, and M. Osofsky. Highly spin-polarized chromium dioxide thin films prepared by chemical vapor deposition from chromyl chloride. *Applied Physics Letters*, 76(25):3789–3791, 2000.

[28] Y. Ji, G. Strijkers, F. Yang, C. Chien, J. Byers, A. Anguelouch, G. Xiao, and A. Gupta. Determination of the spin polarization of half-metallic CrO_2 by point contact Andreev reflection. *Physical Review Letters*, 86(24):5585, 2001.

[29] M. Anwar, F. Czeschka, M. Hesselberth, M. Porcu, and J. Aarts. Long-range supercurrents through half-metallic ferromagnetic CrO_2. *Physical Review B*, 82(10):100501, 2010.

[30] M. Houzet and A. I. Buzdin. Long range triplet Josephson effect through a ferromagnetic trilayer. *Physical Review B*, 76(6):060504, 2007.

[31] J. A. Glick, V. Aguilar, A. B. Gougam, B. M. Niedzielski, E. Gingrich, R. Loloee, W. Pratt Jr, and N. O. Birge. Phase control in a spin-triplet SQUID. *arXiv preprint arXiv:1804.00707*, 2018.

[32] V. Ryazanov, V. Oboznov, A. Y. Rusanov, A. Veretennikov, A. A. Golubov, and J. Aarts. Coupling of two superconductors through a ferromagnet: Evidence for a π junction. *Physical Review Letters*, 86(11):2427, 2001.

[33] T. S. Khaire, W. Pratt Jr, and N. O. Birge. Critical current behavior in Josephson junctions with the weak ferromagnet PdNi. *Physical Review B*, 79(9):094523, 2009.

[34] M. A. Khasawneh, T. S. Khaire, C. Klose, W. P. Pratt Jr, and N. O. Birge. Spin-triplet supercurrent in Co-based Josephson junctions. *Superconductor Science and Technology*, 24(2):024005, 2011.

[35] V. Bol'ginov, V. Stolyarov, D. Sobanin, A. Karpovich, and V. V. Ryazanov. Magnetic switches based on Nb-PdFe-Nb Josephson junctions with a magnetically soft ferromagnetic interlayer. *JETP Letters*, 95(7):366–371, 2012.

[36] E. Gingrich, P. Quarterman, Y. Wang, R. Loloee, W. Pratt Jr, and N. O. Birge. Spin-triplet supercurrent in Co/Ni multilayer Josephson junctions with perpendicular anisotropy. *Physical Review B*, 86(22):224506, 2012.

[37] M. Blamire, C. Smiet, N. Banerjee, and J. Robinson. Field modulation of the critical current in magnetic Josephson junctions. *Superconductor Science and Technology*, 26(5):055017, 2013.

[38] J. Robinson, J. Witt, and M. Blamire. Controlled injection of spin-triplet supercurrents into a strong ferromagnet. *Science*, 329(5987):59–61, 2010.

[39] T. S. Khaire, M. A. Khasawneh, W. Pratt Jr, and N. O. Birge. Observation of spin-triplet superconductivity in Co-based Josephson junctions. *Physical Review Letters*, 104(13):137002, 2010.

[40] M. Anwar, M. Veldhorst, A. Brinkman, and J. Aarts. Long range supercurrents in ferromagnetic CrO_2 using a multilayer contact structure. *Applied Physics Letters*, 100(5):052602, 2012.

[41] W. F. Brown Jr. Thermal fluctuations of a single-domain particle. *Physical Review*, 130(5):1677, 1963.

[42] M. J. Donahue. OOMMF user's guide, version 1.0. Technical report, 1999.

[43] A. Jameson, W. Schmidt, and E. Turkel. Numerical solution of the Euler equations by finite volume methods using Runge Kutta time stepping schemes. In *14th Fluid and Plasma Dynamics Conference*, page 1259, 1981.

[44] A. Aharoni. Demagnetizing factors for rectangular ferromagnetic prisms. *Journal of Applied Physics*, 83(6):3432–3434, 1998.

[45] A. J. Newell, W. Williams, and D. J. Dunlop. A generalization of the demagnetizing tensor for nonuniform magnetization. *Journal of Geophysical Research: Solid Earth*, 98(B6):9551–9555, 1993.

[46] W. Sterk. *Magnetisation characteristics of noncollinear ferromagnetic bilayers*. Bachelor Thesis, Leiden University, 2015.

[47] S. Voltan, C. Cirillo, H. Snijders, K. Lahabi, A. García-Santiago, J. Hernández, C. Attanasio, and J. Aarts. Emergence of the stripe-domain phase in patterned permalloy films. *Physical Review B*, 94(9):094406, 2016.

[48] S. Voltan, A. Singh, and J. Aarts. Triplet generation and upper critical field in superconducting spin valves based on CrO_2. *Physical Review B*, 94(5):054503, 2016.

[49] A. Wachowiak, J. Wiebe, M. Bode, O. Pietzsch, M. Morgenstern, and R. Wiesendanger. Direct observation of internal spin structure of magnetic vortex cores. *Science*, 298(5593):577–580, 2002.

[50] M. Silaev. Possibility of a long-range proximity effect in a ferromagnetic nanoparticle. *Physical Review B*, 79(18):184505, 2009.

[51] A. Singh, C. Jansen, K. Lahabi, and J. Aarts. High-quality CrO_2 nanowires for dissipation-less spintronics. *Physical Review X*, 6(4):041012, 2016.

[52] R. Moriya, L. Thomas, M. Hayashi, Y. B. Bazaliy, C. Rettner, and S. S. Parkin. Probing vortex-core dynamics using current-induced resonant excitation of a trapped domain wall. *Nature Physics*, 4(5):368, 2008.

[53] S. S. Parkin, M. Hayashi, and L. Thomas. Magnetic domain-wall racetrack memory. *Science*, 320(5873):190–194, 2008.

[54] L. Vila, M. Darques, A. Encinas, U. Ebels, J.-M. George, G. Faini, A. Thiaville, and L. Piraux. Magnetic vortices in nanowires with transverse easy axis. *Physical Review B*, 79(17):172410, 2009.

[55] Y. P. Ivanov, A. Chuvilin, L. G. Vivas, J. Kosel, O. Chubykalo-Fesenko, and M. Vázquez. Single crystalline cylindrical nanowires–toward dense 3D arrays of magnetic vortices. *Scientific Reports*, 6:23844, 2016.

[56] M. S. Kalenkov, A. D. Zaikin, and V. T. Petrashov. Triplet superconductivity in a ferromagnetic vortex. *Physical Review Letters*, 107(8):087003, 2011.

4

CONTROLLING SUPERCURRENTS & THEIR SPATIAL DISTRIBUTION IN FERROMAGNETS

Kaveh Lahabi, Morten Amundsen, Jabir Ali Ouassou, Ewout Beukers, Menno Pleijster, Jacob Linder, Paul Alkemade & Jan Aarts

Spin-triplet Cooper pairs induced in ferromagnets form the centrepiece of the emerging field of superconducting spintronics. Usually the focus is on the spin polarization of the triplets, potentially enabling low-dissipation magnetization switching. However, the magnetic texture which provides the fundamental mechanism for generating triplets also permits control over the spatial distribution of supercurrent. Here we demonstrate the tailoring of distinct supercurrent pathways in the ferromagnetic barrier of a Josephson junction. We combine micromagnetic simulations with three-dimensional supercurrent calculations to design a disk-shaped structure with a ferromagnetic vortex which induces two transport channels across the junction. We use superconducting quantum interferometry to verify the presence of the two channels. Moreover, we show how the supercurrent can be controlled by moving the vortex with a magnetic field. This approach paves the way for current paths to be dynamically reconfigured in order to switch between different functionalities in the same device.

This chapter has been published in *Nature Communications* **8**, 2056 (2017).

Author contributions: K.L. and J.A. conceived the disk geometry, K.L. and E.B. performed the micromagnetic simulations. M.A., J.A.O. and J.L. performed the supercurrent simulations and assisted in the Fourier analysis. K.L. FIB-structured the devices, with guidance from P. A., K.L. and M.P. prepared the multilayers and performed the measurements.

4.1. INTRODUCTION

CONVERTING SPIN-SINGLET COOPER PAIRS TO EQUAL-SPIN TRIPLETS requires carefully designed interfaces between a conventional superconductor (S) and a ferromagnet (F) [1, 2]. As described in Section 3.1.2, this process requires both spin-mixing and spin-rotation, which can be brought about by magnetic inhomogeneities at the interface [3]. One method to realize this is to place a thin ferromagnet F' at the S/F interface, and make the magnetization of F and F' non-collinear [4]. This method was recently implemented in Josephson junctions described by 1D geometries, where the supercurrent amplitude was controlled by varying degrees of magnetic non-collinearity (MNC) [5–7]. This concept is illustrated in Figure 4.1 **a-b**. In this work we establish a different direction, where the focus is not the supercurrent amplitude. Instead, the central goal is to exert dynamic control over the triplet generator which in turn determines where the supercurrent spatially flows 4.1 **c**.

We demonstrate how distinct supercurrent paths in a device can be tailored entirely by spin texture, and altered in a dynamic fashion. Such behaviour is intrinsically higher-dimensional and can pave the way for novel hybrid devices in superconducting electronics.

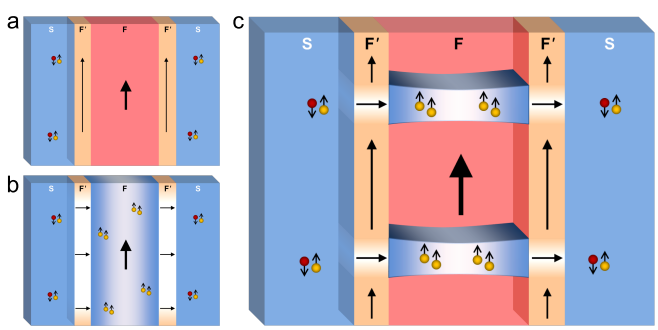

Figure 4.1: **a-b** Controlling the amplitude **a-b** and spatial distribution of supercurrent by the magnetic non-collinearity (MNC) in multilayers. **a** F and F' layers have a collinear magnetization, and the multilayer acts as a single homogenous ferromagnet. This corresponds to minimum junction transport since no long-range triplet current can be generated, and the singlet pairs are broken by the exchange field. Varying the magnetic orientation of the F' layers results in a long-range triplet current, which is maximum when F and F's are perpendicular (**b**). The singlet correlations however remain suppressed. **c** A 2D MNC profile is used to control the distribution of triplet supercurrent and form distinct transport channels.

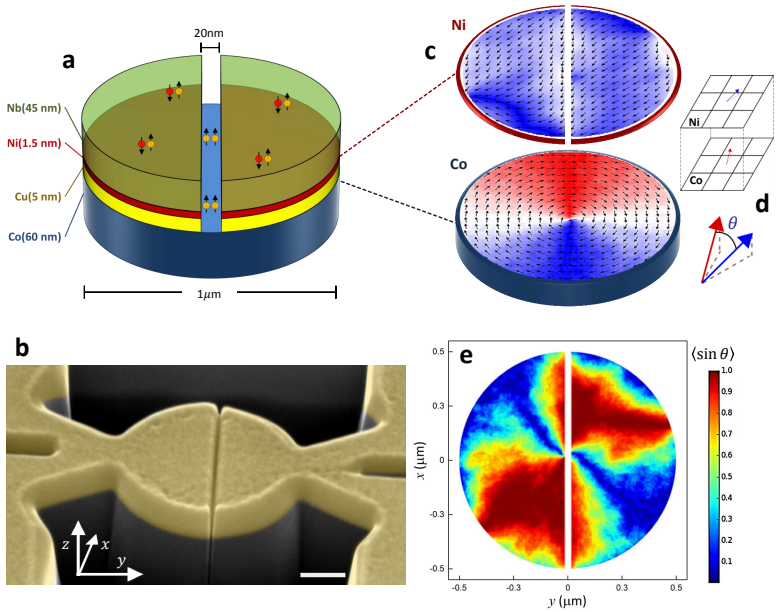

Figure 4.2: **Micromagnetic simulations and device layout**.**a**, Schematic of the device layout. **b**, False-colour scanning electron microscope image of a device. The scale bar corresponds to 250 nm. The disk is structured with Ga^+ focused ion beam (FIB) milling. The junction is formed by opening up a gap in the top Nb/Ni/Cu layers, leaving only Co in the weak link (see Methods for more details).**c**, Plane view of the magnetic states of Co and Ni layers in the disk (from 3-D OOMMF simulations). The pixel colour scheme, red-white-blue, scales with the magnetization along y. Magnetic moments in Ni tend to align with the gap which defines the junction, while the vortex configuration in Co arranges the magnetic moments perpendicular to it. This provides a high degree of magnetic non-collinearity (MNC) for triplet generation. The curled magnetic structure of the vortex is also highly effective in minimizing the stray fields from Co, which otherwise would dominate the Ni magnetization, hence compromising our control of MNC. **d**, Representation of our method to obtain the MNC profile. For each cell at the top of the Co layer, we determine the angle (θ) between its magnetization vector and that of the Ni cell above. **e**, Spatially resolved MNC profile calculated from the simulation results of shown in **c**. $<\sin(\theta)>$ is defined as the outer product between the Co and Ni magnetization vectors (note the colour scheme is different from **c**).The observed suppression of MNC (the blue region) at the centre of the junction is a result of interlayer dipole coupling at the vortex core.

4.2. RESULTS

4.2.1. MICROMAGNETIC SIMULATIONS

The device consists of a disk-shaped planar Josephson junction involving a multilayer of Co/Cu/Ni/Nb, as shown in Figure 4.2 **a**. A central trench cuts the top superconducting Cu/Ni/Nb layers in two halves, here connected via a Co weak link. The disk design combines two crucial elements. First, the magnetic moments in Co are arranged in plane and orthogonal to the trench between the superconducting electrodes, while the moments in Ni lie also in plane but parallel to the trench. Micromagnetic simulations show that this geometry results in a well-defined magnetic ground state with a high degree of MNC, a condition optimal for generating triplets

(Figure 4.2 **c** – **e**). An equally important element is that the disk shape creates a magnetic vortex state in the Co. This vortex produces a distinct suppression of MNC at the centre of the disk (Figure 4.2 **e**), which will be used to distribute the supercurrent in Co over two channels. The MNC suppression is due to the local out-of-plane magnetization at the vortex core, which turns the magnetic moments in the Ni also out-of-plane and, hence, collinear to the Co moments. Incidentally, the in-plane exchange field gradient of a magnetic vortex, without a second ferromagnet, has also been proposed to generate long-ranged triplets [8, 9]. This is the subject of Chapter 5, where we describe the nature transport in disk devices with no Ni layer.

4.2.2. SUPERCURRENT CALCULATIONS

To investigate whether a supercurrent can be expected, we numerically simulate the critical current density passing through the Josephson junction by solving the quasi-classical Usadel equation [10] in 3D using the magnetization texture obtained from the micromagnetic simulations. We do this by means of the finite element method, using the finite element library libMesh [11] in a similar fashion as in Ref. [12] (for details, please refer to Supplementary Note 1 of the original paper Ref. [13]). The superconductors are modelled as bulk, with a phase difference of $\Delta\phi = \pi/2$.

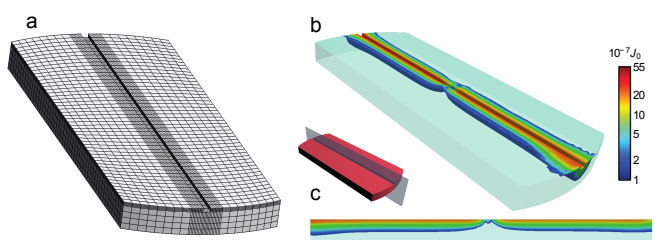

Figure 4.3: **Micromagnetic simulations and device layout**. **a** The discretized model (or mesh) used in the numerical simulation of the critical current. Since the triplet current is mostly concentrated in the immediate vicinity of the trench, the mesh density (and hence the accuracy) is set to be higher for this region. For the same reason, the regions farthest away from the trench have been removed to reduce the calculation time. **b** The critical current density divided by a factor $J_0 = (N_0 e D \Delta)/2\xi$ where N_0 is the density of states at the Fermi level, D is the diffusion constant, Δ is the superconducting gap and ξ is the superconducting coherence length. For clarity, currents lower than $10^{-7} J_0$ are not shown. **c** A slice through the centre of the trench, showing how the current passes across the Co barrier in two separate channels, on either side of the vortex core.

In Figure 4.3 **a** the discretized model is shown. To reduce the calculation time we truncated the otherwise circular geometry to a width of 40% of the disk diameter, as the currents farther away from the trench are negligible. The results are shown in Figure 4.3 **b**, **c**, where it can be seen that the critical current is suppressed at the centre of the disk, thereby effectively creating two separate current channels.

4.2.3. BASIC TRANSPORT PROPERTIES

As shown in Figure 4.4, our junctions show zero resistance and finite critical currents I_c below 3K The magnetic state of the sample was conditioned by applying a 2.5T out-of-plane field at 10K. This is to reduce the stochastic magnetization introduced by FIB milling of when structuring the junction.

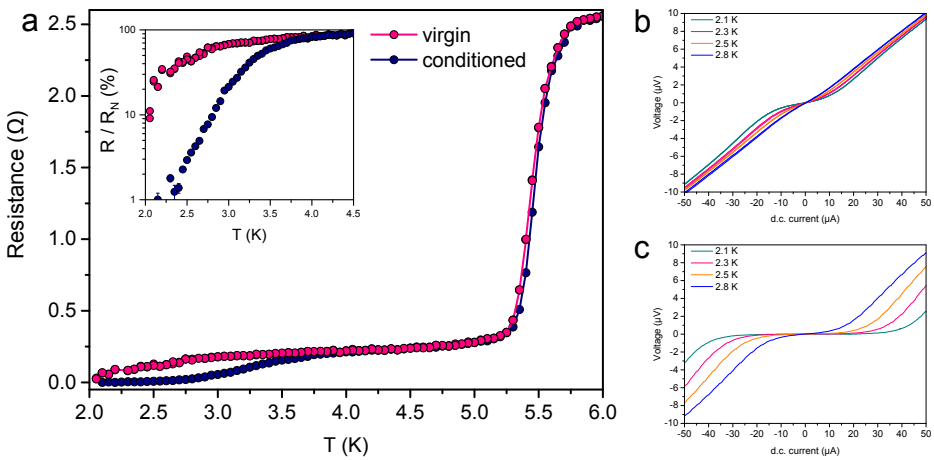

Figure 4.4: Junction transport in the virgin and conditioned states. **a** Resistance as a function of temperature, measured using 10 μA, before (pink) and after (navy) conditioning the sample. Each set shows two distinct transitions. At $T = 5.5$ K, the Nb electrodes become superconducting, while the junction is still in the normal state ($R_N \approx 240$ mΩ). Upon cooling further, resistance undergoes a second transition as the barrier begins to proximize by triplet correlations — eventually reaching zero resistance. For clarity, the $R-T$ dependence at lower temperatures is plotted on a logarithmic scale in the inset. While the superconducting electrodes are unaffected by conditioning the ferromagnets, we observe substantial enhancement of superconductivity in the barrier. **b** and **c** $I-V$ traces taken at several temperatures before and after conditioning the sample, respectively. The pronounced contrast between the two sets indicates that transport depends strongly on the magnetic configuration of the junction.

Figure 4.4 shows there is a strong difference with data taken before and conditioning the sample, which is a first indication that MNC and a triplet supercurrent are involved (also see Supplementary 4.5.2). For instance, conditioning allows the magnetic moments in Ni to rearrange more freely, and align with the gap opened by the FIB. This process increases the MNC in the vicinity of the barrier which, in turn, results in an enhancement of triplet supercurrent at zero field. A consequence of this can be found in the pronounced contrast between the $I-V$ traces measured before and after conditioning the magnetization, as shown in Figure 4.4 **b**, **c**.

4.2.4. SUPERCONDUCTING QUANTUM INTERFEROMETRY

To examine the spatial distribution of current density across our junctions, we apply an out-of-plane magnetic field B_z, and analyse the resulting supercurrent interference pattern. As demonstrated by Dynes and Fulton [14], the shape of such a super-

conducting quantum interference (SQI) pattern is given by the Fourier transform of the position-dependent critical current density across a junction $J_c(x)$ through

$$I_c(B_z) = \left| \int_{-R}^{R} dV J_c(x) e^{\frac{2\pi i L B_z x}{\Phi_0}} \right| \tag{4.1}$$

where L is the effective length of the junction, $2R$ is its lateral width (here the disk diameter), and $\Phi_0 = h/2e$ is the superconducting flux quantum. In a typical junction, the uniform distribution of supercurrent density ($J_c(x)$ =constant) leads to the well-known Fraunhofer interference pattern with a sinusoidal current-phase relation given by

$$\frac{I_c(B)}{I_{c0}} = \left| \frac{\sin\left(\frac{\pi\Phi}{\Phi_0}\right)}{\frac{\pi\Phi}{\Phi_0}} \right| \tag{4.2}$$

Characteristic for the Fraunhofer pattern is a central lobe that is twice as wide as the side lobes (as in Figure 4.5 **c**). These oscillations decay with a $1/B$ dependence. Different device configurations may introduce deviations from the standard pattern, but the described relative widths of the lobes persist as a common feature in all Josephson junctions, since it represents a single-slit interference pattern. In contrast, we expect our disk to exhibit a double-slit interference pattern. This is characterized by slowly decaying sinusoidal oscillations with Φ_0-periodicity, where all lobes have the same width. These patterns are typical for superconducting quantum interference devices (SQUIDs) which, contrary to our device, consist of two individual junctions operated in parallel.

As shown in Figure 4.5 **a**, **b**, the period of the oscillations in our disk device is 7.8 mT (i.e. fluxoid quantization over an effective area of 2.65×10^{-13} m^2, and appears to be temperature-independent. Qualitatively, the SQI patterns in Figure 4.5 **a**,**b** already foretell the presence of two supercurrent channels: the width of the central lobe is comparable to that of the side lobes, and the oscillations decay far more gradually in field than as $1/B$. Two-channel interference patterns were recently observed in junctions with topological weak links [15–17], where the two-slit interference is a result of edge-dominated transport caused by band bending. In our junction however, this is due to the suppression of triplet supercurrent by the (controllable) magnetic vortex core.

To illustrate the contrast with single-slit interference in a similar device configuration, we prepared a disk junction without the Ni layer, and retaining a thin layer of Cu/Nb at the bottom of the trench. This provides a non-magnetic path in the barrier, allowing singlet correlations to contribute to junction transport. Indeed, we observe a typical Fraunhofer-like interference pattern with a two times wider central lobe, shown in Figure 4.5 **c**. Provided that singlet current can dominate the transport, sim-

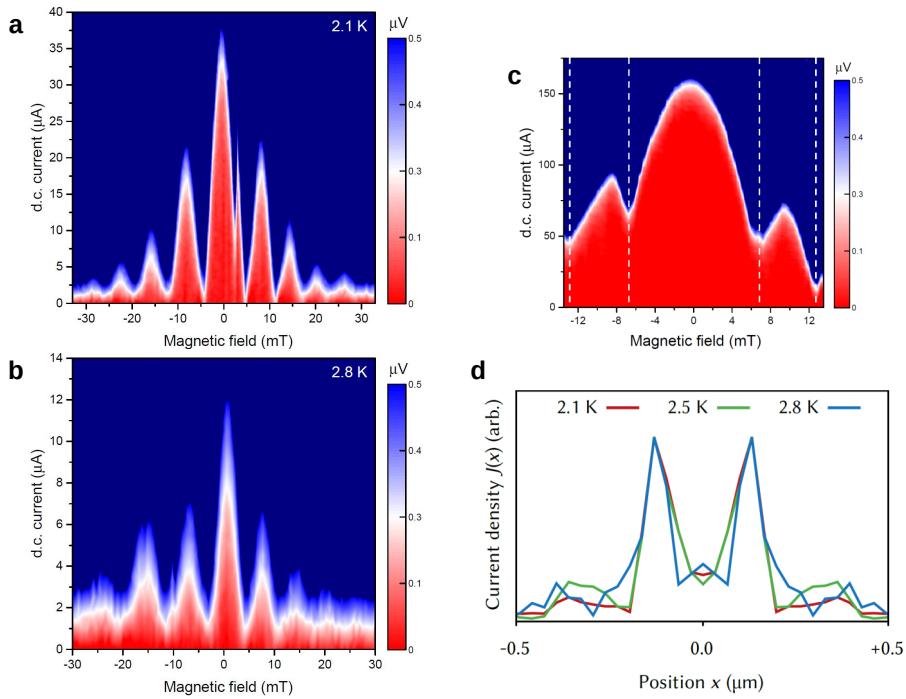

Figure 4.5: Interference patterns and the corresponding current density profiles. **a** and **a** the result of superconducting quantum interference (SQI) measurements taken at 2.1 K and 2.8 K respectively. The patterns show clear double-slit interference, with all lobes having the same width. **c** Single-slit interference pattern from a disk junction where transport is dominated by singlet correlations via a non-magnetic barrier. **d** The current density profiles constructed from the Fourier analysis of SQI patterns taken at 2.1 K , 2.5 K and 2.8 K. The presence of two transport channels, responsible for the SQUID-like interference patterns, is evident.

ilar results can also be produced in presence of the Ni layer (see Supplementary Figure 4.S5).

Figure 4.5 **d** shows the supercurrent density profiles extracted from Fourier analysis of the measured interference patterns. A description of this method can be found in Supplementary 4.5.4, but it should be mentioned that there is some arbitrariness in choosing the position of the sample edge if the effective junction length L is not known. We put the edge at the position where the current density goes to zero, which leads to a value for L of 170 nm. This is a reasonable number. For a homogeneous junction, taking 100 nm for λ_L of the Nb, L would be of the order of 220 nm. There is no reason however to expect very close agreement as discussed in Supplementary 4.5.4. Important is that for any choice of the edge position, two distinct transport channels are clearly visible in the extracted profiles. Comparing these results with the simulations, the supercurrents appear to follow narrower paths, located near the centre of the disk. We attribute this to current crowding effects, in which the neck-

shaped contacts and their sharp corners lead to a forward orientation of the currents. Note that in the electrodes, supercurrent distribution can only vary over a distance set by λ_L, which may explain why it does not simply fan out and form a uniform distribution along the trench.

It is important to note that the origin of the two-channel transport in our junction cannot be explained by singlet supercurrents in a doubly connected path. A direct evidence for this can be found in the SQI measurements taken before conditioning the sample (the virgin state). Let us suppose that two separate current paths were to form by accident during fabrication, and somehow made it possible for singlet correlations to bypass the Co layer via two symmetric channels (asymmetric channels cannot produce the well-defined nodes observed in the interference patterns). Had this been the case, the two channels must have already been present before conditioning the magnetic state, and the device would have behaved as a SQUID from the beginning. In contrast, despite several attempts, no sign of a double-slit interference was found in the virgin state (see Supplementary Figure 4.S1). The SQUID pattern only appeared when the magnetic state was properly conditioned to produce the intended MNC, designed specifically to generate two symmetric triplet channels. More details about the SQI measurements from the virgin state can be found in the Supplementary 4.5.2.

4.2.5. MAGNETOTRANSPORT WITH IN-PLANE FIELDS

Having established the principal role of MNC in shaping the supercurrent, we also examine the possibility of controlling them by altering the MNC profiles using an in-plane field B_y which moves the vortex along the trench Figure 4.6 **a** shows the measured critical currents $I_c(B_y)$ together with the micromagnetic MNC calculations for various stages during the (zero to positive) field sweep. In the first regime (shaded yellow), we modify the MNC profile by moving the vortex core along $+x$ towards the side of the disk. As the field is raised beyond 30 mT, we remove the vortex, thereby suppressing the supercurrent. The suppression of I_c in this regime (shaded blue) is caused by the antiparallel configuration of the ferromagnets, which occurs through the increase of stray fields from Co (now magnetized along $+y$) when the vortex leaves the disk. In the third regime (shaded green), Ni magnetization begins to reverse from negative to positive y direction, while Co remains magnetized along $+y$. At first, this process recovers I_c as a MNC re-emerges over the entire disk. As we increase the field however, the MNC begins to fade away as both layers magnetize along $+y$, resulting in a gradual suppression of I_c. Figure 4.6 **b** shows the variations in $I_c(B_y)$ when sweeping the field from a high positive to negative value, and back. We observe a complex pattern accompanied with a peculiar hysteresis, where individual features are mirrored (and not just shifted) with respect to the direction of field sweep.

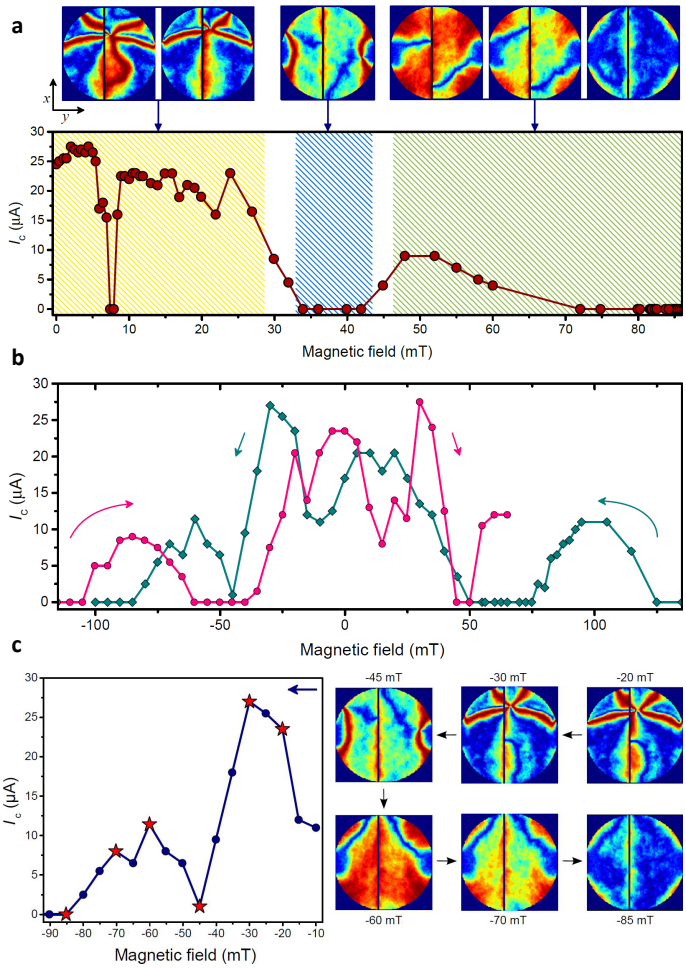

Figure 4.6: Critical current variation and MNC simulations with in-plane field. **a** Measured I_c values and the corresponding magnetic non-collinearity (MNC) profiles, as the system is magnetized by sweeping the field in $+y$ direction. For small fields the vortex core moves along the junction (perpendicular to field direction) to the side of the disk. In this range (shaded yellow), highly non-collinear regions are continuously present and appear to follow the position of the vortex core. The vortex state in Co, which has been effective in suppressing the stray fields, is subsequently removed as the field approaches 30 mT. This leads to a negative dipole field from Co which dominates the effective field acting on Ni. As a result, Ni gets magnetized antiparallel to Co (along $-y$), hence the suppression of MNC and I_c (shaded blue). As the applied field is raised above 45 mT , it begins to compensate for the local stray fields from the Co layer, ultimately reversing the Ni magnetization along $+y$. The change in the magnetic orientation associated with this reversal leads to a distinct (re-)emergence of MNC that gradually fades away above 60 mT - as Ni magnetization aligns with Co (shaded green). **b** I_c measured while reversing the field in both directions along y. A clear hysteresis is observed, with individual features are mirrored with respect to field sweep direction. This complex pattern is a result of a changing MNC as the multilayer reverses its magnetization. **c** Positive to negative branch of experimentally measured I_c (B_y) shown together with simulated MNC profiles. Each MNC snapshot is obtained at the specified field, and corresponds to a measurement labeled by the star symbol. Taking steps of 5 mT, simulation shows the vortex enters at -20 mT, moves along $-x$, and exits the system at -45 mT. The MNC is once again is enhanced at -60 mT, and gradually fades away as the field magnetizes all layers along $-y$.

The observed field dependence is fundamentally different from the usual hysteresis in SFS junctions, where the self-field of the ferromagnets can distort or introduce a shift in the interference pattern [18–20]. This is rather a distinct characteristic of triplet supercurrents produced by a varying degree of MNC, as the multilayer reverses its magnetization. The measured hysteresis is of a similar nature as the ones reported in Refs. [5, 6] for multilayer vertical stacks. The most notable difference here is arguably the relatively large field range where I_c is zero, and the pronounced reentrant superconductivity that follows. Figure 4.6 **c** compares one branch (positive to negative) of the measured $I_c(B_y)$ with the simulated MNC snapshots taken at various stages vortex reversal. Even though the experiment and the simulation both sweep the field in steps of 5 mT, the simulated fields for vortex entry and exit translate to direct enhancement and suppression of the measured I_c, respectively. For the fields below −45 mT, the behavior is similar to the one described for the third regime (green shade) in Figure 4.6 **a**.

As a final point, it should be noted that in the present letter we have assumed the channels have an equal phase. This assumption is reasonable for a symmetric MNC (hence spin-mixing) on each side [4]. Whether both channels are 0 or π, as long as they are symmetric, the SQI results will be indistinguishable. This would not strictly apply to systems with asymmetric spin texture (e.g. caused by vortex displacement), which can result in different phases for the triplet channels [9].

4.3. DISCUSSION

Spin-triplet supercurrents in ferromagnets have been bearing the promise of dissipationless use of spin-polarized currents. This study opens up a completely different direction, in which the focus is not the homogeneous amplitude of the supercurrent, but rather the dynamical control over its spatial distribution. This can lead to novel hybrid devices for superconducting electronics. Moreover, our extensive use of simulations, both of the micromagnetic configurations and of the supercurrents themselves, allow for detailed design and understanding before the actual fabrication of the hybrid device. The next step will be to introduce magnetization dynamics. Magnetic vortices or domain walls can be moved with pulses in the GHz regime, and this can also be simulated. Directing supercurrents then becomes possible on nanosecond timescales, opening the way for high-speed superconducting electronics.

4.4. METHODS

4.4.1. DEVICE FABRICATION

Multilayers of Co (60 nm)/Cu (5 nm)/Ni (1.5 nm)/Nb (45 nm) were deposited on unheated SiO_2-coated Si substrates by Ar sputtering in an ultrahigh vacuum chamber (base pressure below 10^{-8} Pa). The thickness of Co and the diameter of the disk (1 μm) are chosen to ensure stabilization of a magnetic vortex [21, 22]. The 5 nm Cu layer is used to avoid exchange coupling between the layers. The thickness of the Ni layer was tuned for optimal triplet generation in similar systems [20, 23]. The samples were subsequently coated with Pt (7 nm) to protect them from oxidation and to reduce the damage introduced by Ga^+ ions during focused ion beam (FIB) processing.

A combination of electron-beam lithography and FIB milling (50 pA Ga^+ beam current) was used to structure the disks. Next, FIB with 1 pA current was applied to open the sub-20 nm gap that forms the junction. The trench depth is controlled by the duration of milling. The 1 pA beam current provided sufficient timespan (several seconds) to vary the depth in a controlled manner. The device used for investigating single-slit transport was subject to the same processing steps, with the following exceptions. First, the multilayer was deposited without Ni to minimize triplet generation. Second, when creating the weak link, the duration of FIB milling was reduced by 20% to retain a layer of Cu/Nb at the bottom of the trench. This provides a non-magnetic path for singlet supercurrent in the weak link (on top of Co). The trench is presumably deeper near the sides of the disks (where sputtered atoms can escape more easily) than at the centre. Hence, in contrast to triplets, singlet correlations would favor the centre of the disk where a non-magnetic channel may still be present on top of the Co barrier.

4.4.2. MAGNETOTRANSPORT MEASUREMENTS

The magnetic properties of Co and Ni films used in our devices were characterized by ferromagnetic resonance experiments and SQUID magnetometry. Transport measurements were performed in a Quantum Design Physical Properties Measurement System where samples could be cooled down to 2.1 K. For both in- and out-of-plane measurements, the field was aligned within 2° of the sample plane. Resistance versus temperature was measured with a current of 10 μA. The current-voltage characteristics were taken in a four-probe configuration using a current-biased circuit and a nanovoltmeter. The critical current was determined using a voltage criterion: $V > 0.3$ μV for SQI and $V > 0.1$ μV for in-plane measurements.

The virgin state was measured directly after fabrication (Supplementary 4.5.2). Prior to the $I_c(B_z)$ measurements presented in the letter, the magnetic state of the sample

was conditioned by applying a 2.5 T out-of-plane field at 10 K. The sample was stored in a UHV chamber for 106 days and re-wired to a different puck, and the same measurements were repeated using a different magnet. We were able to reproduce the same Ic patterns, and no discernable changes in transport characteristics (e.g., $R(T)$ or I_c) were observed.

4.4.3. MICROMAGNETIC SIMULATIONS

The finite element micromagnetic calculations were carried out using the Object Oriented Micromagnetic Framework (OOMMF) [24]. The multilayer is divided into a three-dimensional mesh of 5 nm cubic cells. The exchange coefficient and saturation magnetization of Co were set to 30×10^{-12} Jm^{-1} and 1.40×10^{6} Am^{-1}, respectively, while for Ni these values were 9.0×10^{-12} Jm^{-1} and 4.90×10^{5} Am^{-1}. The Gilbert damping constant α was set to 0.5 to allow for rapid convergence. The direction of anisotropy was defined by a random vector field to represent the polycrystalline nature of the sputtered films. The Usadel calculations are based on static micromagnetic simulations of a multilayer disk with a diameter of 1 μm. For simulations with an applied in-plane field (shown in Figure 4.6), the disk design was extended to include the leads used for transport measurements in the actual device (Supplementary Figure 4.S2). In the absence of in-plane fields, the overall magnetic configuration remains relatively unaffected by the leads: the vortex core continues to suppress the MNC, resulting in two main channels for long-ranged triplet correlations. However, the influence of the leads on shape anisotropy becomes relevant when sweeping the field along y. This allows for an accurate estimate of the MNC, and the resulting variation in I_c during the magnetization reversal.

4.4.4. CONTROL EXPERIMENT

In addition to the device used for investigating the triplet currents, a control sample was prepared in parallel, on the same substrate. This was deposited together with the main device, and received the same treatment, with only one exception: the Ga^+ dose used for opening the gap that forms the weak link was lowered by 50%. Reducing the dose stops the milling before it reaches the Co layer in the trench. This leaves a non-magnetic path in the weak link for singlet correlations. The contribution of singlet supercurrent results in a critical current that is around 20 times higher than its neighboring junction (the main device) where the Co weak link can effectively suppress singlet correlations, hence allowing long-ranged triplet supercurrents to dominate the transport. Unlike triplets, the singlet current is not sensitive to the spin texture (i.e., MNC) of the system. This is evident from the single-slit (Fraunhofer-like) interference pattern, shown in Supplementary Figure 4.S5.

4.5. SUPPLEMENTARY INFORMATION

4.5.1. SUPPLEMENTARY FIGURES

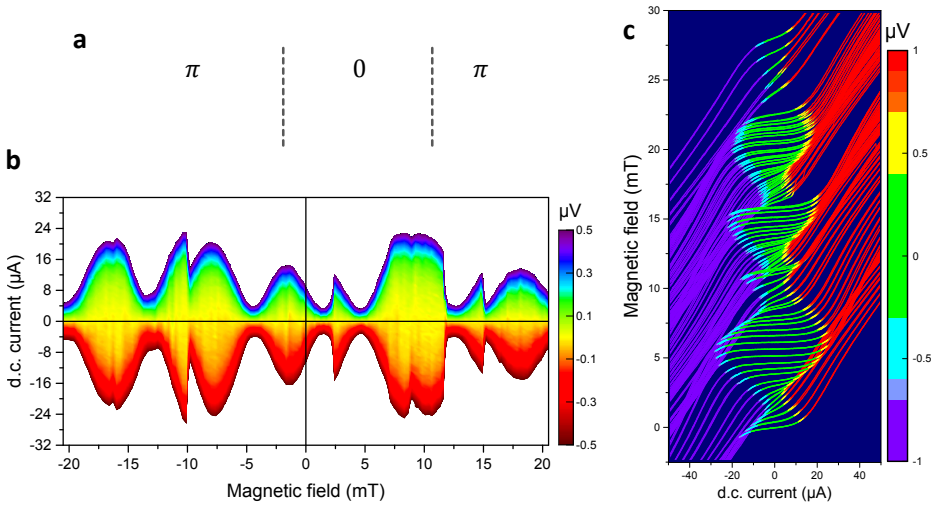

Figure 4.S1: Interference patterns from the virgin magnetic state. (a) Disordered magnetic state of Ni before conditioning (schematic). The stochastic magnetic orientation of Ni on each side of the trench can lead to the formation of multiple 0 and π segments across the junction. (b) Supercurrent interference pattern of the virgin magnetic state, measured while sweeping the out-of-plane field from negative to positive 30 mT in steps of 0.3 mT. On average, the supercurrent is suppressed for small fields (below 5 mT) in both field directions. The interference pattern is characterized by random discontinuities. These irregularities are shown more clearly in (c) which shows individual I-V curves taken while scanning the field from 28 mT back to zero. The curves are given an offset to represent the field they were measured at. All measurements are taken at $T = 2.1$ K.

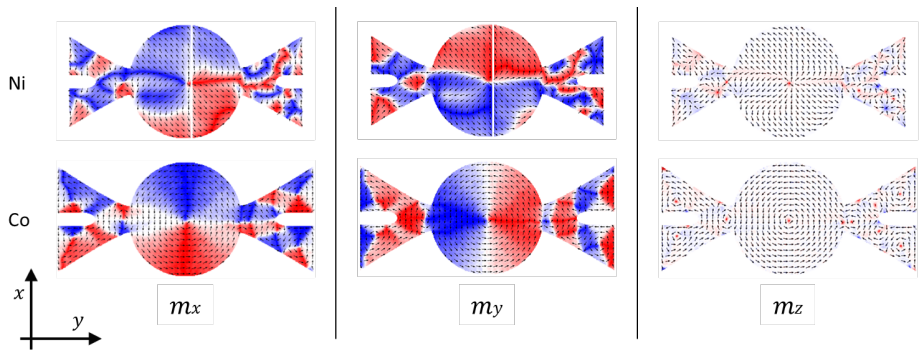

Figure 4.S2: Micromagnetic simulations with an in-plane field. Top views of the magnetic states of Co and Ni layers obtained from OOMMF simulations. The leads are included in the design to produce a more realistic shape anisotropy, needed to accurately describe the system under an in-plane field. Individual components of the magnetization vector $\boldsymbol{m}$ are plotted separately for clarity. The pixel colour scheme, red-white-blue, scales with the magnitude of each component. The red and blue pixels represent positive and negative values respectively. Out of plane magnetization (m_z) is generally suppressed, except at the vortex core where both layers have a highly localized out of plane component. In the actual device, the trench that forms the junction is slightly off-centred. This feature is accounted for in the simulations by placing the gap in Ni 40 nm away from the centre of the disk.

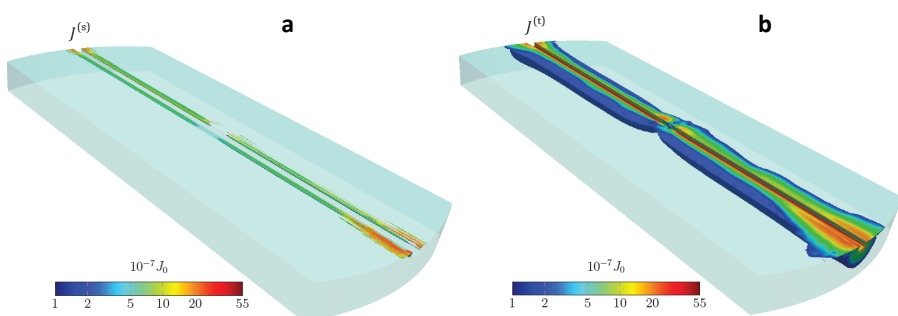

Figure 4.S3: Simulated contributions of singlet and triplet supercurrents. (a) Magnitude of the current density generated by singlet Cooper pairs, $J^{(s)} = |\boldsymbol{J}^{(s)}|$, which is greatly suppressed except for in the immediate vicinity of the superconductors. (b) Magnitude of the current density generated by triplet Cooper pairs, $J^{(t)} = |\boldsymbol{J}^{(t)}|$. For clarity, currents lower than $10^{-7} J_0$ have been removed, which explains why no singlet current is observed in the trench. It is noted that while the total current $\boldsymbol{J} = \boldsymbol{J}^{(s)} + \boldsymbol{J}^{(t)}$ is conserved, $\boldsymbol{J}^{(s)}$ and $\boldsymbol{J}^{(t)}$ are generally not. This is due to the magnetization, which causes oscillations between the singlet and triplet states.

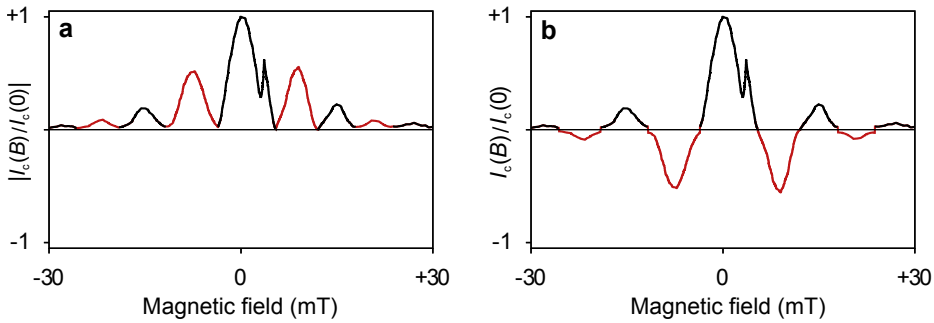

Figure 4.S4: Recovering the complex critical current. (a) The (unsigned) $|I_c(B)|$ pattern extracted from I-V measurements. (b) The signed $I_c(B)$ interference pattern reconstructed by flipping the signs of alternate lobes as in Ref [14]. The data were taken at 2.1 K.

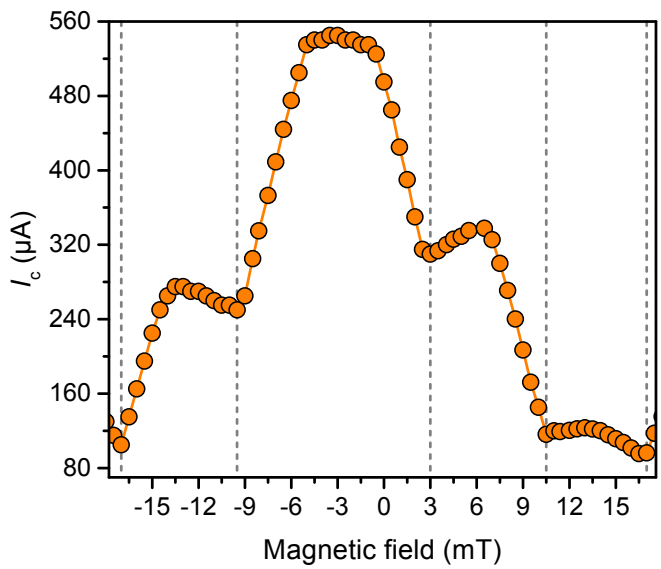

Figure 4.S5: Control experiment. Supercurrent interference pattern measured at $T = 2.1$ K from a control device that was processed in parallel with the one presented in the main text. Deposited together on one substrate, the same multilayer of Pt(7 nm)/Nb(45 nm)/Ni(1.5 nm)/Cu(5 nm)/Co(60 nm) was used in both devices. The Ga^+ dose applied in milling the weak link for the control device was reduced by 50 %. This provides a nonmagnetic pathway in the weak link, where singlet current is not suppressed, and can therefore dominate the transport. The result is a junction with a substantially higher critical current, showing single-slit interference pattern.

4.5.2. SUPPLEMENTARY NOTE 1: TRANSPORT IN THE VIRGIN STATE

Prior to conditioning the magnetization, supercurrent interference patterns were measured using small out-of-plane fields. These are presented in Figure 4.S1. In contrast to the conditioned sample, $I_c(B_z)$ is generally suppressed around zero field. We observe two maxima, which always occur at fields higher than 5 mT. Note that this offset cannot be attributed to remnant fields from the ferromagnet. The applied field for the interferometry measurements is not sufficient to have an appreciable influence on the magnetization of either layer. This is verified by SQUID magnetometry and ferromagnetic resonance experiments.

It has been proposed that the phase of triplet correlations in a S/F'/F/F'/S junction such as ours, is determined by the relative magnetic orientation of the F and F' layers on each side [25]. On the other hand, this unusual interference pattern, with two maxima and suppressed I_c at zero field, is the characteristic of a junction with multiple parallel 0 and π channels [26, 27]. This condition could be fulfilled in the virgin state, where the arbitrary orientation of Ni and Co magnetization can lead to random formation of multiple 0 and π segments across the junction. These interference patterns are also characterized by irregular discontinuities, which could be attributed to the arbitrary arrangement of the 0 and π segments.

Remarkably, we find these features to disappear altogether after conditioning the sample: $I_c(B_z)$ turns into a highly regular and reproducible SQUID pattern, with maximum I_c consistently appearing at $B_z = 0$. This pronounced dependence on magnetic conditioning was absent for junctions where singlet correlations dominated the transport: no significant changes in the interference pattern or the maximum value of I_c were observed.

4.5.3. SUPPLEMENTARY NOTE 2: NUMERICAL SIMULATIONS OF THE CRITICAL CURRENT

To calculate the critical current we use the quasiclassical approximation in the diffusive limit, which yields the Usadel equation [10]*

$$D\nabla\hat{\boldsymbol{g}}\nabla\hat{\boldsymbol{g}} + i\left[\hat{\boldsymbol{\rho}}_3 + \hat{\boldsymbol{\rho}}\cdot\boldsymbol{h}, \hat{\boldsymbol{g}}\right] = 0 \tag{4.3}$$

where D is the diffusion constant and ϵ is the quasiparticle energy. The magnetization texture from the micromagnetic simulations are represented as an exchange field $\boldsymbol{h} = \boldsymbol{h}(\boldsymbol{r})$. Furthermore we have defined $\hat{\boldsymbol{\sigma}} = \mathrm{diag}(\boldsymbol{g}, \boldsymbol{g}^*)$, where σ is a vector of Pauli matrices, and $\hat{\boldsymbol{\rho}}_3 = \mathrm{diag}(1, 1, -1, -1)$. From $\hat{\boldsymbol{g}} = \hat{\boldsymbol{g}}(\boldsymbol{r}, \epsilon)$, the 4×4 retarded Green function matrix in Nambu $\otimes$ spin space, the equilibrium current density may be

* The theoretical insights on supercurrent simulations were provided by Morten Amundsen, Jabir Ali Ouassou and Jacob Linder

computed as

$$\hat{\boldsymbol{J}} = \frac{N_0 e D}{2} \int \mathrm{d}\epsilon \, \mathrm{Re}\,\mathrm{Tr}\left(\hat{\boldsymbol{\rho}}_3 \hat{\boldsymbol{g}} \nabla \hat{\boldsymbol{g}}\right) \tanh\left[\frac{\beta\epsilon}{2}\right] \tag{4.4}$$

where N_0 is the density of states at the Fermi level, and $\beta = 1/(k_B T)$. We neglect the inverse proximity effect, and assume that the superconductors on each side of the trench are large enough to be approximated as bulk. In the calculations, we have used that the critical current is approximately found for a phase difference between the superconductors of $\Delta\phi = \pi/2$. For simplicity, we use transparent boundary conditions between the Ni and the Co layer, whereas we use the low-transparency Kupriyanov-Lukichev boundary conditions [28] at the Ni-Nb interface.

In the modeling of the geometry, we have assumed an effective superconducting coherence length of $\xi = 10$ nm, so that the radius of the circular disk becomes $R = 50\,\xi$. In the direction crossing the trench, the model has been truncated to a width of $W = 40\,\xi$ to reduce the model size. This has been done under the assumption that any contribution to the current from the removed regions is negligible due to the vast distance to the opposite superconductor. The thickness of the Ni and the Co layers have been set to ξ and $6\,\xi$, respectively, and the width of the trench is $2\,\xi$. The Ni thickness is set larger than in the actual experiment to avoid unnecessarily small elements in the Ni-region, which would substantially increase the calculation time. Although this yields lower values for the triplet current, the purpose of our calculation here is to identify the origin of this current; and not its absolute magnitude.

The spatial distribution of the magnetization in both the Ni and the Co layer are accurately mapped onto the 3D mesh via the exchange field $\hat{\boldsymbol{h}}$, where an amplitude of $|\hat{\boldsymbol{h}}| = 30\Delta \approx 46$ meV was used. While this is significantly lower than typical exchange fields in Co, it is still sufficient to quench the contribution of singlet Cooper pairs to the current density. To verify this, we make use of the fact that the supercurrent density generated by the singlet $\boldsymbol{J}^{(s)}$ and triplet $\boldsymbol{J}^{(t)}$ Cooper pairs contribute additively $J = \boldsymbol{J}^{(s)} + \boldsymbol{J}^{(t)}$. The two components are presented in Figure 4.S3 It is clear that the current density of singlet pairs rapidly vanishes away from the superconductors. In contrast, the triplet current density maintains an appreciable value over a substantially larger region, indicating that triplet Cooper pairs are the primary means of transport. The results will therefore be qualitatively the same for a more realistic strength of the exchange field. The advantage of using the reduced value is that the current densities become larger, which in turn make the numerical calculations less resource intensive.

The finite element analysis was carried out using 27-node hexagonal volume elements, and the Green function is interpolated within each element by means of second order Lagrange polynomials. This means that the current density within each element is interpolated by linear polynomials. To ensure that the spatial distribu-

tion of the current density is accurately resolved, we use a refined mesh in a region surrounding the trench, as is shown in Figure 4.3 **a** in the main text. For more details regarding the finite element analysis of three-dimensional superconducting heterostructures, please consult ref [12].

4.5.4. SUPPLEMENTARY NOTE 3: FOURIER ANALYSIS OF SUPERCURRENT DENSITY PROFILES

As shown by Dynes and Fulton1, the supercurrent density profile $J(x)$ can be determined from the superconducting interference pattern $I_c(B)$ using a Fourier transform:

$$J(x) \sim \int_{-\inf}^{+\inf} \mathrm{d}B \; I_c(B) \exp \frac{2\pi i L B x}{\phi_0} \tag{4.5}$$

Here, the coordinate system is defined such that the magnetic field B is applied along the z-axis, the critical current I_c is measured along the y-axis, and the current distribution J(x) can then be determined along the x-axis. The equation also depends on the effective length L of the junction and the flux quantum $\phi_0 = h/2e$. Note that $I_c(B)$ is the signed critical current, where the sign is determined from the experimentally measured $|I_c(B)|$ by assuming that it consists of alternating positive and negative lobes, as described in more detail in ref [14]. This procedure is justified when the interference pattern consists of well-defined maxima separated by deep minima, as is the case for our measurements.

The original method by Dynes and Fulton was derived for a rectangular junction where the dimensions of each superconductor are much larger than the London penetration depth λ. In that case, the effective junction length $L = 2\lambda + d$, where d is the thickness of the barrier between the superconducting leads. In our case, however, the junction is cylindrical and the current distribution not uniform, so the length (which determines the amount of flux to be screened) is not well defined. We therefore performed the Fourier analysis without making any assumptions regarding the value of L, but instead assumed that the position along the x-axis where we obtained $J(x) \to 0$ likely corresponded to the junction ends $x \approx \pm R$, where R is the cylinder radius. From this, we obtained an estimate $L \approx 180$ nm for the effective junction length. This value is somewhat lower than expected for a uniform rectangular junction: in that case the effective area is $2RL$ while the first minimum in $I_c(B_z)$ is at 7.8 mT, yielding $L \approx 270$ nm. Both numbers are of correct order of magnitude: the value of λ for a 50 nm Nb film is about 110 nm [29] so $2\lambda + d$ is 240 nm. If we were to take the sharp drop in the current density profile as the sample edge, L would become less than 100 nm, which appears to be too low in view of the value of λ.

The SQI experiments are carried out by measuring the voltage as a function of current for a given applied magnetic field, i.e. $V(I,B)$. The critical current $|I_c(B)|$, used for the Fourier analysis, is obtained by extracting a contour for a small but finite voltage threshold $V(I_c,B) > 0.3$ μV. Experimentally we find this criterion to be optimal for reducing noise effects that distort the shape of $I_c(B)$. The result is then adjusted to the y-axis so that $|I_c(B)| = 0$ at the nodes between the lobes of the interference pattern. This is to account for the artificial offset introduced by the 0.3 μV threshold voltage. We then recover the complex critical current $I_c(B)$, by switching the sign of every other lobe of the measured $|I_c(B)|$. The original $|I_c(B)|$ and the signed $I_c(B)$ curves are shown side-by-side in Figure 4.S4.

Note that the measured $I_c(B)$ may slightly deviate from a perfectly symmetric pattern, and yield a complex supercurrent distribution $J(x)$ after Fourier transformation. This apparent asymmetry however is predominantly caused by experimental noise. We therefore discard the complex phase $J(x)$ to approximate the supercurrent distribution profile by $|J(x)|$, shown in Figure 4.5 **d** of the main text.

REFERENCES

[1] M. Eschrig. Spin-polarized supercurrents for spintronics: a review of current progress. *Reports on Progress in Physics*, 78(10):104501, 2015.

[2] J. Linder and J. W. Robinson. Superconducting spintronics. *Nature Physics*, 11(4):307, 2015.

[3] F. Bergeret, A. Volkov, and K. Efetov. Long-range proximity effects in superconductor-ferromagnet structures. *Physical Review Letters*, 86(18):4096, 2001.

[4] A. I. Buzdin. Proximity effects in superconductor-ferromagnet heterostructures. *Reviews of Modern Physics*, 77(3):935, 2005.

[5] N. Banerjee, J. Robinson, and M. G. Blamire. Reversible control of spin-polarized supercurrents in ferromagneticJosephson junctions. *Nature Communications*, 5:4771, 2014.

[6] A. Iovan, T. Golod, and V. M. Krasnov. Controllable generation of a spin-triplet supercurrent in a Josephson spin valve. *Physical Review B*, 90(13):134514, 2014.

[7] W. M. Martinez, W. Pratt Jr, and N. O. Birge. Amplitude control of the spin-triplet supercurrent in S/F/S Josephson junctions. *Physical Review Letters*, 116(7):077001, 2016.

[8] M. Silaev. Possibility of a long-range proximity effect in a ferromagnetic nanoparticle. *Physical Review B*, 79(18):184505, 2009.

[9] M. S. Kalenkov, A. D. Zaikin, and V. T. Petrashov. Triplet superconductivity in a ferromagnetic vortex. *Physical Review Letters*, 107(8):087003, 2011.

[10] K. D. Usadel. Generalized diffusion equation for superconducting alloys. *Physical Review Letters*, 25(8):507, 1970.

[11] B. S. Kirk, J. W. Peterson, R. H. Stogner, and G. F. Carey. libMesh: a C++ library for parallel adaptive mesh refinement/coarsening simulations. *Engineering with Computers*, 22(3-4):237–254, 2006.

[12] M. Amundsen and J. Linder. General solution of 2D and 3D superconducting quasiclassical systems: coalescing vortices and nanoisland geometries. *Scientific Reports*, 6:22765, 2016.

[13] K. Lahabi, M. Amundsen, J. A. Ouassou, E. Beukers, M. Pleijster, J. Linder, P. Alkemade, and J. Aarts. Controlling supercurrents and their spatial distribution in ferromagnets. *Nature Communications*, 8(1):2056, 2017.

[14] R. Dynes and T. Fulton. Supercurrent density distribution in Josephson junctions. *Physical Review B*, 3(9):3015, 1971.

[15] S. Hart, H. Ren, T. Wagner, P. Leubner, M. Mühlbauer, C. Brüne, H. Buhmann, L. W. Molenkamp, and A. Yacoby. Induced superconductivity in the quantum spin hall edge. *Nature Physics*, 10(9):638, 2014.

[16] V. S. Pribiag, A. J. Beukman, F. Qu, M. C. Cassidy, C. Charpentier, W. Wegscheider, and L. P. Kouwenhoven. Edge-mode superconductivity in a two-dimensional topological insulator. *Nature Nanotechnology*, 10(7):593, 2015.

[17] M. T. Allen, O. Shtanko, I. C. Fulga, A. Akhmerov, K. Watanabe, T. Taniguchi, P. Jarillo-Herrero, L. S. Levitov, and A. Yacoby. Spatially resolved edge currents and guided-wave electronic states in graphene. *Nature Physics*, 12(2):128, 2016.

[18] V. Bol'ginov, V. Stolyarov, D. Sobanin, A. Karpovich, and V. V. Ryazanov. Magnetic switches based on Nb-PdFe-Nb Josephson junctions with a magnetically soft ferromagnetic interlayer. *JETP Letters*, 95(7):366–371, 2012.

[19] E. Gingrich, P. Quarterman, Y. Wang, R. Loloee, W. Pratt Jr, and N. O. Birge. Spin-triplet supercurrent in Co/Ni multilayer Josephson junctions with perpendicular anisotropy. *Physical Review B*, 86(22):224506, 2012.

[20] M. A. Khasawneh, T. S. Khaire, C. Klose, W. P. Pratt Jr, and N. O. Birge. Spin-triplet supercurrent in Co-based Josephson junctions. *Superconductor Science and Technology*, 24(2):024005, 2011.

[21] J. d. e Castro, D. Altbir, J. Retamal, and P. Vargas. Scaling approach to the magnetic phase diagram of nanosized systems. *Physical Review Letters*, 88(23):237202, 2002.

[22] N. Dao, S. Whittenburg, and R. Cowburn. Micromagnetics simulation of deep-submicron supermalloy disks. *Journal of Applied Physics*, 90(10):5235–5237, 2001.

[23] S. Voltan, A. Singh, and J. Aarts. Triplet generation and upper critical field in superconducting spin valves based on cro 2. *Physical Review B*, 94(5):054503, 2016.

[24] M. J. Donahue. OOMMF user's guide, version 1.0. Technical report, 1999.

[25] M. Houzet and A. I. Buzdin. Long range triplet Josephson effect through a ferromagnetic trilayer. *Physical Review B*, 76:060504, 2007.

[26] H. Smilde, D. Blank, G. Gerritsma, H. Hilgenkamp, H. Rogalla, et al. d-wave–induced Josephson current counterflow in $YBa_2Cu_3O_7$/Nb zigzag junctions. *Physical Review Letters*, 88(5):057004, 2002.

[27] C. Gürlich, S. Scharinger, M. Weides, H. Kohlstedt, R. Mints, E. Goldobin, D. Koelle, and R. Kleiner. Visualizing supercurrents in ferromagnetic Josephson junctions with various arrangements of 0 and π segments. *Physical Review B*, 81(9):094502, 2010.

[28] M. Y. Kuprianov and V. Lukichev. Influence of boundary transparency on the critical current of dirty SS'S structures. *Zh. Eksp. Teor. Fiz*, 94:149, 1988.

[29] A. Gubin, K. Il'in, S. Vitusevich, M. Siegel, and N. Klein. Dependence of magnetic penetration depth on the thickness of superconducting Nb thin films. *Physical Review B*, 72(6):064503, 2005.

5

GENERATING SPIN-TRIPLET SUPERCURRENTS WITH A FERROMAGNETIC VORTEX

Generating long-range spin-triplet Cooper pairs requires some form of magnetic inhomogeneity at the interface with a superconductor. This is usually realized using multiple ferromagnets with non-collinear magnetization. Controlling the magnetization of individual ferromagnets however is a highly challenging task. A more efficient method would be to implement the spin texture of a single ferromagnet. We demonstrate this here in a lateral disk-shaped Josephson junction with a cobalt weak link. In this case, the spin-triplet supercurrent is generated by the in-plane exchange field gradient of a magnetic vortex in a cobalt microdisk. Moreover, we show that such devices offer a distinct capacity for controlling the phase, amplitude and spatial distribution of supercurrent in a dynamic fashion. This opens up new possibilities for the realization of superconducting logic and non-volatile memory elements.

As yet unpublished due to a patent application on "spin-textured Josephson junctions".

5.1. MOTIVATION

We begin this chapter with a follow-up experiment on the device introduced in Chapter 4, where we showed how the path of spin-triplet supercurrents can be modified by the magnetic structure of a Co (60 nm)/Ni (1.5 nm) bilayer in a disk-shaped Josephson junction. The purpose of this experiment is to demonstrate a different aspect of our device, one which concerns the *phase* of spin-triplet channels. This subject is revisited in the next section, where we discuss the triplet supercurrents generated by a single ferromagnetic vortex.

5.1.1. FORMATION OF 0-π TRIPLET CHANNELS: S/F'/F/F"/S

Figure 5.1 **a** shows critical current measured while scanning the magnetic field in x-direction $I_c(H_x)$ i.e. field is applied parallel to the trench that defines our weak link (see Figure 4.3 for more details). We begin at $H_x = 0$, where critical current is at its maximum. In this state (labeled **A**), an out-of-plane measurement would produce the double-slit interference pattern, which was described in section 4.2.4. This is also shown in Figure 5.1 **b**, for both negative and positive bias currents. It is important to remember that in state **A**, $I_c(H_z)$ has a single maximum close to zero field. This is independent of sweep sequence or direction of H_z[1].

As we increase H_x, the magnetic vortex in Co begins to move in y-direction, away from the trench (vortex moves perpendicular to the applied field). This results in a rapid suppression of supercurrent, which completely disappears for $H_x \gtrapprox 20$ mT. Remarkably, $I_c(H_x)$ remains heavily suppressed even when the field is brought back to zero (**B**). Although there is a noticeable rise at $H_x \approx -20$ mT (**C**), the junction only retains its maximum critical current at -45 mT (**D**). At first glance, it may seem that the observed suppression of I_c is simply due to the lack of magnetic non-collinearity (MNC), necessary for generating long-range triplet current. This however would be far from accurate, as our simulations and out-of-plane interferometry measurements reveal.

Micromagnetic simulations with an in-plane field indicate that, during the magnetization reversal, the vortex is not simply brought back, but that an intermediate configuration exists with up to three vortices which converge into a single vortex state at sufficiently large negative magnetic fields. This corresponds to transition at **D** in Figure 5.1, where the critical current recovers its maximum value. Figure 5.1 **c** shows an $I_c(H_z)$ pattern, taken while the system was in the 'suppressed current' state. The experimental setup used for these measurements could only provide magnetic fields in one direction. Hence, to obtain the results shown in Figure 5.1 **c**, we stopped the in-

[1] In some field sweeps the $I_c(H_z)$ maximum may appear slightly shifted (by less than 2 mT), there are however no discernable changes in the pattern itself.

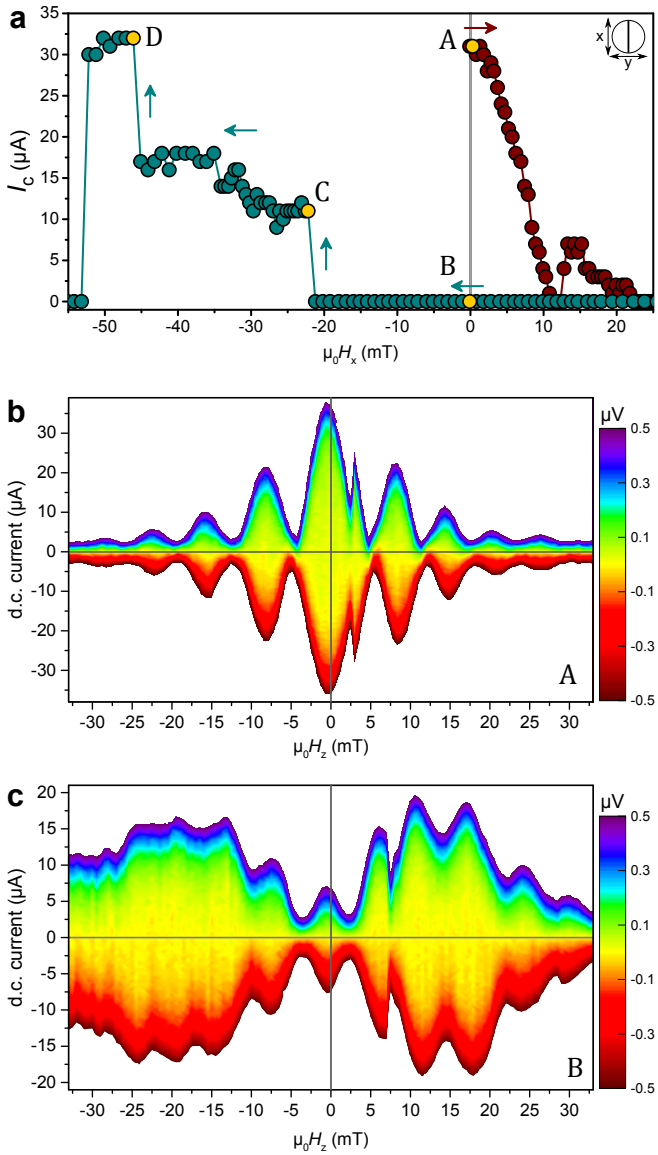

Figure 5.1: **stable states of the Co-Ni disk: interference patterns from different transport states.** **a**, I_c measured as a function of H_x for forward (wine) and reverse (cyan) field sweep directions, at 2.1 K. Inset shows the x and y directions with respect to the orientation of the junction barrier. The H_x sweep sequence was 0 → +150 mT → −150 mT. The field sweep was stopped at **A** and {B to measure the interference patterns shown in **b** and **c**, respectively. **b,c** were obtained by sweeping the out-of-plane field H_z as +35 mT → −35 mT, while the in-plane field is zero. Reducing the field range did not affect the I_c behaviour shown here. **b** is the double-slit interference pattern with maximum I_c at zero field, described in Chapter 4. **c** I_c is suppressed at zero field, and has high-field maxima in *both* directions.

plane field sweep at $H_x \approx 0$, turned the sample plane by 90° (so that $H \parallel z$), and then continued by measuring $I_c(H_z)$. While $I_c(0)$ is initially suppressed, it grows larger as we sweep the field in either direction. In contrast to the initial pattern **A**, the main maxima occur at $\approx \pm 12$ mT or higher. Had there been no triplet generation in our device (e.g. due to lack of MNC), I_c would have remained constantly suppressed throughout the H_z sweep. The reason for measuring a reduced I_c at small fields is not absence of triplet supercurrents, but rather their *presence* in the form of spontaneous supercurrents.

Suppression of $I_c(0)$ and high-field maxima[2] in the interference pattern are the universal characteristics of Josephson junctions with multiple 0 and π segments arranged in parallel (the so-called 0-π junction). Such systems have been realized in zigzag-shaped d-wave/s-wave [1] and S/F/S junctions, where step-like changes in the thickness of the F layer can be used to create an array of 0 and π segments [2, 3] (short-range proximity effect). This means that the critical current density J_c needs to alternate its sign along the junction as $J_c^0 \approx -J_c^\pi$. As the phase varies from 0 to π (and vice versa), it creates a spontaneous circulating current around the 0-π boundary. The spontaneous supercurrent also carries a vortex with the total flux of $\pm\Phi_0$. If the 0 and π segments are equal in size and critical current density $J_c^0 = -J_c^\pi$, the junction has no capacity for an additional bias current, which appears as $I_c = 0$ in a transport measurement. Applying an external field compensates for the built-in phase variations in the junction, and allows for constructive interference of currents between the 0 and π segments, which in turn leads to the enhancement of I_c.

The interference pattern of a given 0-π junction depends on the exact number, size and arrangement of the 0 and π channels, as well as their critical current densities. In our device these parameters are determined by the number and configuration of the magnetic vortices in Co, as well as the relative alignment of the Ni layer in the left and right side of the junction. The former defines the size and the number of channels (since each vortex interrupts the flow of supercurrent), and the latter determines their phase (see 3.5). If the magnetic orientation of the left Ni layer is *locally* parallel (antiparallel) to that on the right side, the channel behaves as a π (0) junction. This concept is illustrated in Figure 4.S1. Unlike the Co disk, the 1.5 nm thick Ni layer does not have a robust magnetization pattern. As shown in Figure 4.S2, its magnetic texture is not fully decoupled from the transport leads connected to the disk, and can be easily disturbed by the magnetization of Co. While every simulation shows the magnetic moments of Ni to lie along the trench ($\parallel x$), the relative orientation of the left and right sides can change. Estimating the Ni magnetization becomes even more challenging if there are multiple vortices in the Co, due to the strong coupling to the local dipole fields from each vortex core.

[2] Interference pattern for a single field sweep needs to have maxima in both positive and negative fields. This is to exclude self-fields of the ferromagnets, which can only introduce a field offset in the original interference pattern.

To summarise, the main obstacle here is that there are no reliable means to control the magnetic structure of the Ni (1.5 nm) layer on both sides of the junction. While this does not prevent us from generating long-range triplet currents, and regulating their spatial distribution, it does limit our capacity to control the phase. We resolve this in the next section by removing the Ni layer, and utilizing the vortex magnetization of the Co disk to generate and control long-range triplet supercurrents.

What makes the results of Figure 5.1 already promising is that there are two stable zero-field states, corresponding to maximum and minimum I_c (**A** and **B**, respectively). For each state, the device was warmed up to room temperature, stored in a vacuum chamber for a finite number of days (often weeks) and measured again. We found no discernable changes in the value of I_c or the interference pattern before the warm-up. This represents a promising new outlook for the realization of non-volatile superconducting memory elements.

5.2. GENERATING SPIN-TRIPLET SUPERCURRENTS WITH A FERROMAGNETIC VORTEX

Triplet supercurrents are commonly generated by a ferromagnetic trilayer S/F'/F/F"/S, where F' and F" can have non-collinear magnetizations. In terms of control over supercurrents, the full potential of such systems is only realised if the magnetization of each ferromagnet can be regulated independently. There are however alternatives to this. It has been proposed that the spin structure of a ferromagnetic vortex can be used to generate long-range triplet correlations [4, 5]. Here we demonstrate this in disk-shaped Josephson junctions, where the superconducting electrodes are separated by a cobalt barrier (≈ 20 nm long). Figure 5.2 shows the schematic of our device. The system contains two key elements. One is the *in-plane* gradient of the exchange field, responsible for generating the long-range triplet correlations, and the other is the vortex core, where the local magnetization turns out-of-plane. The core plays a key role by suppressing the long-range triplet component [4]. Sample preparation followed the same procedure as the one described in Chapter 4. The only difference here is the absence of the Ni (1.5 nm) layer.

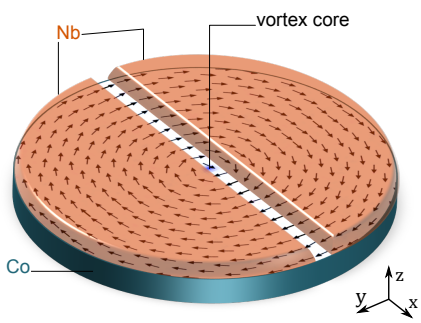

Figure 5.2: Schematic of the device. Superconducting electrodes are deposited directly on the Co, with no additional magnetic layers. The junction is formed by opening a gap (≈ 20 nm) in the Nb layer, leaving only Co in the weak link. The arrows represent the simulated magnetic pattern in Co. At the vortex core the magnetic moments turn sharply out-of-plane (blue pixels).

5.2.1. BASIC TRANSPORT AND GROUND STATE INTERFERENCE

Figure 5.3 shows the typical transport behavior of a Co disk junction with long-range triplet currents. In the absence of in-plane fields, the ground state of our system corresponds to a single vortex at the centre of the disk. While in this state, transport characteristics are similar to those of the Co-Ni disk from Chapter 4. This is shown in Figure 5.3, where we see a double-slit interference pattern (i.e. lobes with a similar width). The two systems however reveal their differences in in-plane measurements.

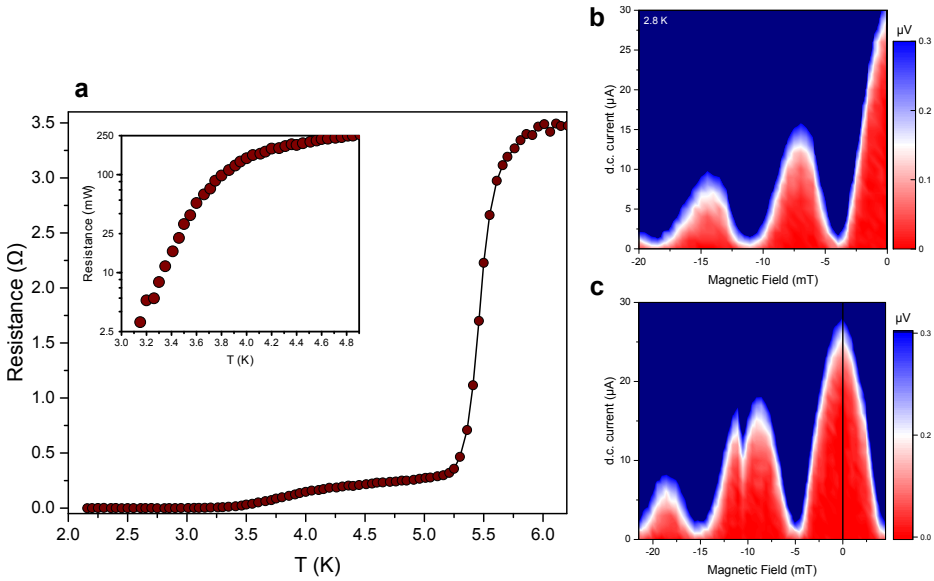

Figure 5.3: **Co disk: transport at ground state magnetizationa**, resistance as a function of temperature $R(T)$, measured using a 10 μA current bias. $R(T)$ shows two distinct transitions, with the one at lower temperatures corresponding to the junction, andis shown on a logarithmic scale in the inset. **b,c** interference patterns at 2.8 K, measured while sweeping the out-of-plane field from 0 to +20 mT (**b**), and from 21 mT to −5 mT (**c**). Both sweeps correspond to a double-slit interference pattern, and I_c has a single maximum at zero field, regardless of sweep direction.

5.2.2. MAGNETOTRANSPORT WITH IN-PLANE FIELDS

In-plane fields can alter the magnetic structure of our junction by displacing the vortex core in a perpendicular direction. Figure 5.4 **a** shows the critical current of Co disk junction; measured as a function of $H_y \perp$ trench. This corresponds to a vortex displacement along the trench. In order to show the contrast, Figure 5.4 **b** presents the same measurements carried out on the Co-Ni disk (taken from the previous chapter). Initially, at $H_y = 0$, both systems show maximum critical current. As we sweep the field to 15 mT, the critical current of the Co disk drops to zero. This field regime corresponds to maximum vortex core displacement ≈ 20 nm per mT (estimated from micromagnetic simulations). We also observe an abrupt suppression of supercurrent in Co-Ni device at $H_y = 7$ mT. This however occurs over a narrow field range ≈ 2 mT, and I_c is recovered by $H_y = 10$ mT. In contrast, supercurrent transport in the Co disk remains suppressed up to 25 mT. Yet, our simulations show the vortex to be present in the disk up to $H_y = 40 \pm 5$ mT. We attribute the suppressed I_c in this field range to the phase difference between the triplet channels, which develops when we disrupt the axisymmetric pattern of the ferromagnetic vortex. This causes the system to act as a 0-π SQUID, and is discussed later in this section.

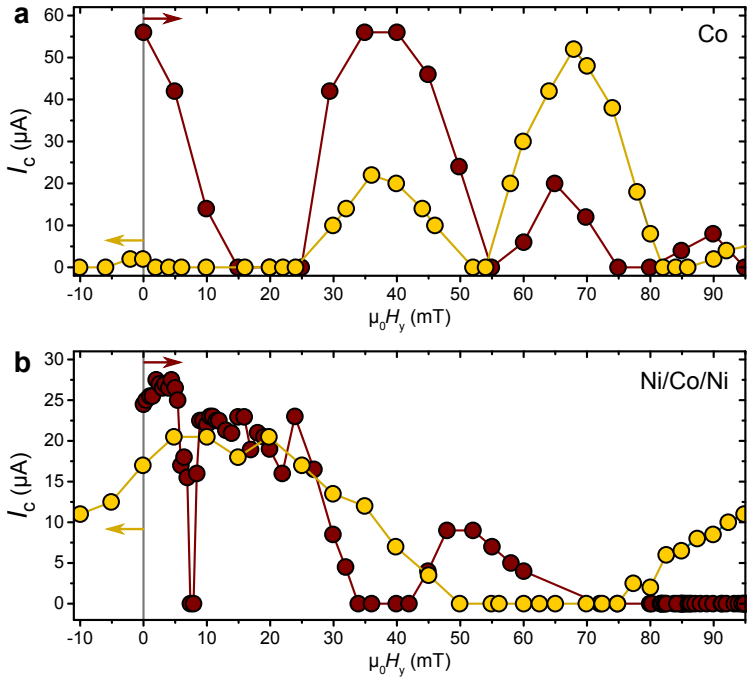

Figure 5.4: **In-plane measurements: Co disk vs. Co-Ni disk.**, I_c measured as a function of H_y, for forward (wine) and reverse (yellow) field sweeps. The sweep sequence followed as 0 → +150 mT → −150 mT. **a**, shows the behaviour of the Co disk, which is the focus of this chapter. **b**, corresponds to the same sequence of measurements from the Co-Ni disk, and is presented here to highlight the contrast between the two systems. The most notable one being the behaviour of I_c during the field reversal, where the Co disk maintains $I_c \approx 0$ at zero field.

I_c grows rapidly as we increase the field above 25 mT, and even recovers the original (zero field) maximum, before it sharply declines at 45 mT. In our simulations this corresponds to the vortex core being pressed against the edge of the disk (on one side of the junction), and subsequently exiting the system at $H_y \gtrsim 45$ mT. Note that the reentrant superconductivity observed in the Co disk is substantially larger than that of the Co-Ni device, and occurs over a different field range (e.g. at 40 mT I_c is maximum in the Co disk, but is zero for the Co-Ni device). We also observe small but finite peaks up to 90 mT. Although we cannot identify their origin at this stage, these might correspond to some form of local spin texture in Co (e.g. buckling).

We continue to magnetize the system by sweeping up to 150 mT, at which point we reverse the sweep direction. As we reduce the field back to zero (yellow), we find a highly unusual behavior, where I_c is maximum at 68 mT but is heavily suppressed around zero field. This $I_c(H_y)$ pattern is also robust with respect to sweep direction. Following the same measurement protocol with negative field would mirror the pattern point by point, i.e. $I_c(-H_y)_{(\text{reverse})} = I_c(+H_y)_{(\text{forward})}$. Hence, sweeping in both

directions results in a suppressed I_c at zero field. This however could be fully reversed by reconditioning the system with fields of 50 mT or higher, which brings back the original SQUID pattern with maximum I_c appearing at zero field.

Micromagnetic simulations indicate that during such field reversal, our system goes through a range of nonuniform magnetic patterns, which can have profound consequence for the phase and distribution of long-range triplet supercurrents. These include various forms of buckling (e.g. the so called S and C states), as well as multiple vortices and saddle points which appear at $H_y = 0$. A discussion on these states is however beyond the scope of this chapter. Instead, here we focus on the single vortex state, which is arguably the most robust and controllable magnetic pattern.

5.2.3. EMERGENCE OF 0 & π CHANNELS IN THE VORTEX

It was proposed by Kalenkov *et al.* [5], that both zero and π junctions can be realized with the long-range triplet components in a ferromagnetic vortex. More specifically, they predict the junction to be in the π state when the superconducting electrodes are not symmetric with respect to the vortex magnetization pattern. They proposed to realize this by asymmetric geometries for the superconducting electrodes placed on the vortex. However, the same situation can in principle be created by breaking the axisymmetric pattern of the vortex, as we do here by applying an in-plane field, which produces an asymmetric magnetic pattern with respect to the electrodes. There is however one crucial difference between our system and the ones described in Ref. [5], and it concerns the vortex core. The above-mentioned theoretical framework was formulated for a system with a fully in-plane magnetization, as the core ($\lesssim$ 20 nm) is deemed to be too small (compared to the coherence length) to play a significant role. This is a sound and practical assumption. As we have seen however, the local magnetization of the vortex core tends to be highly effective in suppressing long-range triplet currents. This leads to the formation of two transport channels, either one of which can be in the zero or π regime. Hence, the system has the capacity to act as a SQUID with four possible configurations: 0-0, π-π, 0-π and π-0. The controllable nature of a magnetic vortex allows for the implemention of in-plane fields to switch between these modes by changing the magnetization pattern in a reversible manner. We explore this in the following section with the use of a vector magnet.

5.2.4. INTERFERENCE PATTERNS FROM A DISPLACED VORTEX

The core of the ferromagnetic vortex can be freely displaced by applying relatively small magnetic in-plane fields ($\lesssim$ 40 mT). Once the field is removed however, magnetization will return to its original state, with the core positioned at the centre of the disk. While in this state, superconducting quantum interferometry (SQI) measure-

ments yield a double-slit pattern, with $I_c(H_z)$ being maximum at zero field, which could correspond to either a 0-0 or a π-π SQUID configuration. The exception to this is when we drive the vortex out of the disk by applying a sufficiently large in-plane field. In this case, removing the field would transform the magnetization to a metastable state with multiple vortices present in the disk[3]. SQI patterns from this state are similar to those of junctions with multiple 0-π segments (...0-π-0-π-0...), which are characterized by a suppressed $I_c(H \approx 0)$ and high-field maxima (e.g. see Figure 5.1 **c**). However, the complex magnetic pattern of the metastable state, combined with unusual interference patterns, prevent us from developing a comprehensive description of the phase and number of transport channels involved. A systematic approach would be to reduce the problem to a single vortex; and examine the $I_c(H_z)$ patterns, measured while the core is displaced by a constant H_{xy} field.

The measurements presented so far were carried out in a Physical Properties Measurement System (PPMS) by Quantum Design, where magnetic field can be applied in only one direction. While we could switch between in- and out-of-plane configurations by (mechanically) turning our sample, the setup cannot support $I_c(H_z)$ measurement in presence of a finite H_{xy}. Hence, SQI measurements could only be applied to the states that are stable at zero in-plane field. We overcome this limitation with the use of a cryostat equipped with a "vector magnet", which allows us to control the applied field in x, y and z directions separately.

Figure 5.5 shows the $I_c(H_z)$ patterns, taken while applying constant H_x fields. For each value of H_x, we also present the simulated magnetic pattern (right panel), with the line representing the gap in Nb. It should also be mentioned that this is a different sample than the one presented in the previous section (its basic transport properties are however very similar). In the absence of in-plane fields, the vortex core is situated at the centre of the disk, and we observe our usual double slit interference pattern, with maximum I_c at zero field (Figure 5.5 **a**).

We then proceed by sweeping H_x to 10 mT, where we find an abrupt suppression of I_c. In this state, the interference pattern is still very much SQUID-like, as the lobes appear to be similar in width. Instead of a maximum however, $I_c(H_z)$ now has a minimum at zero field. For a SQUID device, this pattern would correspond to a 0-π state. Our simulation for this field shows the core to be displaced along y. As the magnetic pattern is no longer symmetric with respect to the superconducting electrodes, the formation of a π channel would also be consistent with the predictions of Ref. [5].

Before we continue with the results, it is important to note that the observed suppression of $I_c(H_z \approx 0)$, which we attribute to a 0-π SQUID state, cannot be produced by self-fields (i.e. stray fields) from the ferromagnet, or a field offset in our measure-

[3] these states are stabilised by the Co in the transport leads, connected to the sides of the disk, which modify the shape anisotropy. Such states are usually absent in symmetric magnetic dots.

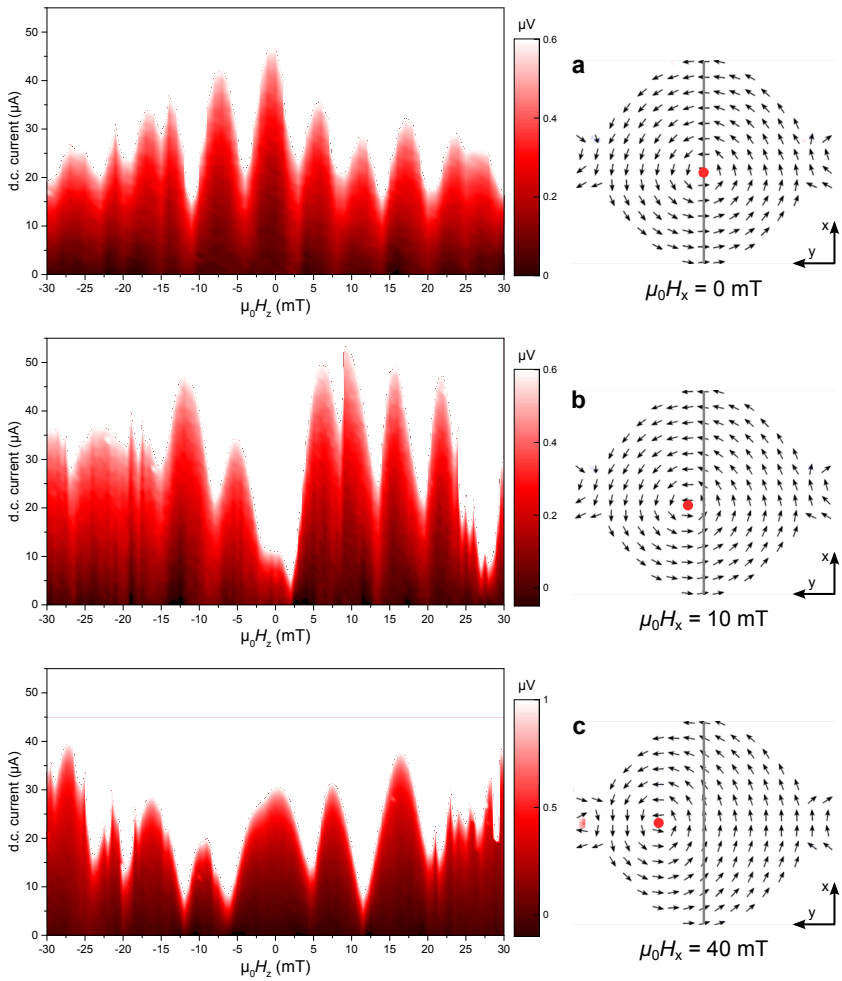

Figure 5.5: **Supercurrent interference with different magnetic patterns.** The left panel shows the interference patterns, measured by scanning H_z from +30 mT to −30 mT, in steps of 0.5 mT, while fixing H_x at 0 mT (**a**), 10 mT (**b**) and 40 mT(**c**) during a forward H_x sweep. The right panel shows the simulated magnetic patterns for the specified H_x fields. The grey line in the middle disk represents the junction barrier, and the red dot indicates the position of the vortex. At $H_x = 0$ (**a**) the core is located in the middle of the junction, which yields a double-slit interference pattern, with all lobes having the same width, and a maximum I_c at zero field. **b**, $H_x = 10$ mT breaks the symmetry of the system by slightly shifting the core from the centre. The interference pattern is similar to that of a 0-π SQUID: I_c is suppressed for $H_z \approx 0$, the lobes maintain a similar size and the pattern appears to be shifted with respect to $H_z = 0$. **c**, the core is displaced by over 100 nm from the centre. I_c shows an entirely different behaviour, and cannot be described by a two-channel transport.

ment setup. Firstly, the same $I_c(H_z)$ patterns could be reproduced, regardless of how we sweep H_z. For each H_x shown in Figure 5.5, we measured the interference pattern while sweeping H_z as 0 → +30 mT, +30 mT→ −30 mT and −30 mT→ +30 mT, in steps of 0.5 mT. The same SQI behaviour was found in all three patterns. Secondly, here we are only comparing the interference patterns with *each other*. Even if there is a finite error in the absolute value of the applied field, this would not change the interference patterns relative to each other. Lastly, and most importantly, for every triplet device we measure, there is also a control device (located on the same substrate), where the junction transport is carried out by singlet currents (for details on control experiments, see Section 4.4.4 and Figure 4.S5). Despite having the same Co structure, the singlet junctions exhibit none of the effects described above. These devices consistently yield a Fraunhofer pattern (single-slit), and exhibit no appreciable dependence on in-plane fields. While reconditioning the magnetization could in some cases shift the $I_c(H_z)$ maximum by up to ≈ 2.5 mT in *one* direction (most likely by switching the vortex polarity), the Fraunhofer pattern itself remains unchanged.

Figure 5.5 **c** shows the SQI pattern taken at H_x = 40 mT, where we find $I_c(0)$ to recover. At this point in the simulation, the core is over 100 nm away from the junction barrier (i.e. the trench). We find an unusual interference pattern, which itself appears to be a combination of different patterns. The central lobe is similar to that of Fraunhofer (i.e. twice as wide as the subsequent ones). Instead of decaying however, the supercurrent grows larger with the field. We are not aware of any system where a similar interference pattern has been observed, and hence can only speculate about its origin. Nonetheless, a crude inverse Fourier analysis of the pattern suggests the presence of three separate transport channels, with the smallest one located in the middle of the weak link.

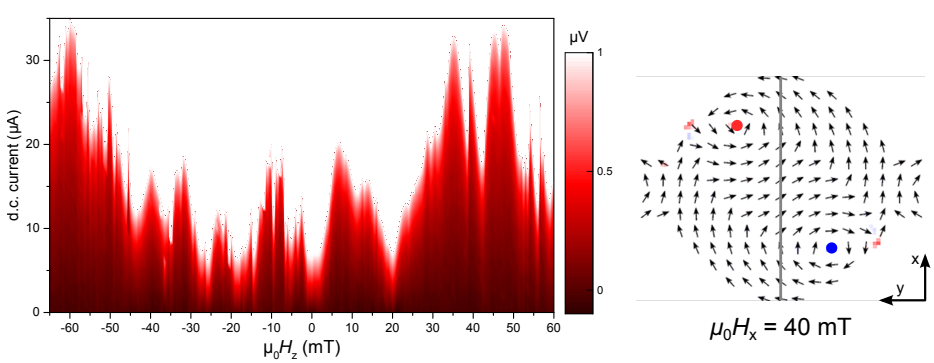

Figure 5.6: I_c behaviour at H_x = 40 mT, measured during the reverse H_x sweep. Micromagnetic simulations show that while reversing H_x from 150 mT, two vortices entre the disk at $mu_0 H_x \approx 40$ mT, as shown in right panel. Red and blue represent positive and negative polarities, respectively. In contract to the interference pattern measured during the forward H_x sweep (Figure 5.5 **c**), I_c is heavily suppressed within ±5 mT, but recovers as we increase the field beyond 30 mT in either directions.

We continue by magnetizing the system with $H_x \rightarrow 150$ mT, and then return the field back to $H_x = 40$ mT to measure a second $I_c(H_z)$ pattern (shown in 5.6). Our simulations show that following this particular field sweep sequence, the disk would be hosting two vortices instead of one, which should profoundly alter the nature of transport in our device. This is indeed the case, as we find an entirely different SQI pattern than the one in Figure 5.5 **c**. While initially I_c is heavily suppressed, it grows larger with the applied field up to 50 mT. We also observe a series of small features which may appear as stochastic discontinuities in some underlying interference pattern. Surprisingly however, we find these features to not be random, as almost every single peak was reproduced in forward and reverse field scans.

5.2.5. SUMMARY & OUTLOOK

Long-range spin-triplet correlations in ferromagnets form a novel platform to control various aspects of supercurrents including their amplitude, phase and spatial distribution. This however, relies on the ability to control the magnetic structure of a device, which so far has typically consisted of a ferromagnetic trilayer S/F'/F/F"/S, where F' and F" need to have non-collinear magnetizations with respect to F. Here we present an alternative to this, where the long-range triplet component is generated by the magnetic pattern of a ferromagnetic vortex. By reducing the number of required ferromagnets to one, this system sets a milestone for the utilization of spin-triplet supercurrents in functional devices.

In contrast to the trilayer system, here the long-range triplet component is induced by the in-plane gradient of the exchange field. We find these correlations to be suppressed by the out-of-plane magnetization of the vortex core, resulting in a two-channel interference pattern[4]. Depending on the position of the vortex core, the two channels can develop a phase difference. For small displacements of the core, we find interference patterns similar to that of a 0-π SQUID. More generally, depending on the position of the vortex with respect to the electrodes, we can yield widely different transport behaviours in the same device (e.g. see Figure 5.5).

In addition to the single vortex state, there are states with multiple vortices (up to three) which can be stabilized by proper conditioning of magnetization. Interference pattern from these states indicate the presence of multiple 0-π regions in our junction. A consequence of this is that there can be two (and possibly more) stable zero-field states with minimum and maximum $I_c(0)$ values (see Figure 5.4 **a**). As these states are defined entirely by the magnetic pattern of a strong ferromagnet (Co), they are highly stable. Even when warmed up and stored at room temperature for long periods (often weeks), upon cooling, we measure the same value of $I_c(0)$.

[4] there is however a distinct possibility for spontaneous currents to emerge *near* the vortex core, due to the non-coplanar magnetic texture. See Ref. [6] for more details.

This introduces a new direction for the realisation of non-volatile superconducting memory, where the bits are stored in the magnetic pattern of a *single* ferromagnet, and are read by measuring the I_c (or rather $I_c R_N$). Even more promising are the possibilities for "writing" the bits. So far we have used static magnetic fields to switch from one I_c state to another. However, magnetic vortices can be displaced and manipulated by pulses in the GHz regime, making this an ideal platform to implement magnetization dynamics for high-speed superconducting electronics.

REFERENCES

[1] H. Smilde, D. Blank, G. Gerritsma, H. Hilgenkamp, H. Rogalla, et al. d-wave–induced Josephson current counterflow in $YBa_2Cu_3O_7$/Nb zigzag junctions. *Physical Review Letters*, 88(5):057004, 2002.

[2] S. Scharinger, C. Gürlich, R. Mints, M. Weides, H. Kohlstedt, E. Goldobin, D. Koelle, and R. Kleiner. Interference patterns of multifacet 20×(0- π) Josephson junctions with ferromagnetic barrier. *Physical Review B*, 81(17):174535, 2010.

[3] C. Gürlich, S. Scharinger, M. Weides, H. Kohlstedt, R. Mints, E. Goldobin, D. Koelle, and R. Kleiner. Visualizing supercurrents in ferromagnetic Josephson junctions with various arrangements of 0 and π segments. *Physical Review B*, 81(9):094502, 2010.

[4] M. Silaev. Possibility of a long-range proximity effect in a ferromagnetic nanoparticle. *Physical Review B*, 79(18):184505, 2009.

[5] M. S. Kalenkov, A. D. Zaikin, and V. T. Petrashov. Triplet superconductivity in a ferromagnetic vortex. *Physical Review Letters*, 107(8):087003, 2011.

[6] M. Silaev. Double-slit Fraunhofer pattern as the signature of the Josephson effect between berezinskiĭ superconductors through the ferromagnetic vortex. *arXiv:1708.07467*, 2017.

6

LITTLE-PARKS OSCILLATIONS WITH HALF-QUANTUM FLUXOID FEATURES IN Sr_2RuO_4

Yasui, Yuuki and Lahabi, Kaveh and Anwar, Muhammad Shahbaz and Nakamura, Yuji and Yonezawa, Shingo and Terashima, Takahito and Aarts, Jan and Maeno, Yoshiteru

In a micro ring of a superconductor with a spin-triplet equal-spin pairing state, a fluxoid, a combined object of magnetic flux and circulating supercurrent, can penetrate as half-integer multiples of the flux quantum. A candidate material to investigate such half-quantum fluxoids is Sr_2RuO_4. We fabricated Sr_2RuO_4 micro rings using single crystals and measured their resistance behavior under magnetic fields controlled with a three-axes vector magnet. Proper Little-Parks oscillations in the magnetovoltage as a function of an axially applied field, associated with fluxoid quantization are clearly observed, for the first time using bulk single crystalline superconductors. We then performed magnetovoltage measurements with additional in-plane magnetic fields. By carefully analyzing both the voltages V_+ (V_-) measured at positive (negative) current, we find that, above an in-plane threshold field of about 10 mT, the magnetovoltage maxima convert to minima. We interpret this behavior as the peak splitting expected for the half-quantum fluxoid states

This chapter has been published in *Physical Review B* **96**, 180507(R) (2017)

Author contributions: The crystals were grown in the group of Y. Maeno at Kyoto University. Y. Yasui and Y. Nakamura prepared the crystals. K. Lahabi and Y. Nakamura micro-structured the crystals under the supervision of T. Terashima. Y. Yasui, Y. Nakamura and K. Lahabi conducted the measurements. S. Yonezawa supervised and supported the measurements. Y. Yasui and K. Lahabi analysed the results. M. S. Anwar took part in the discussion. Y. Maeno and J. Aarts directed the project. All authors discussed the results and contributed to the final manuscript.

6.1. INTRODUCTION

RECENTLY, it has been recognized that Majorana particles, which have unusual equivalence to their own antiparticles and have been long sought in elementary particle physics, can be realized as quasiparticle excitation in condensed-matter systems such as topological superconductors [1]. In particular, Majorana zero modes (MZMs), the zero-energy states of the Majorana branch, have attracted much attention since MZMs do not obey ordinary Abelian statistics and can be utilized for quantum computing [2, 3]. Thus, direct detection of MZMs has become a holy grail of current condensed matter physics [4, 5]. Half-quantum fluxoid (HQF) [6] in a spin-triplet superconductor or a superfluid is known to host such MZMs [7, 8].

An additional phase degree of freedom in a superconducting wave function is the key ingredient for the realization of HQF states. For a spin-singlet superconducting ring with wave function $\psi_S = |\Delta_S|e^{i\theta}$, the single-valuedness of ψ_S requires quantization $\Phi' = n\Phi_0$ (integer-quantum fluxoid, IQF) inside a closed path. Here, n is an integer, Φ' is the fluxoid, and $\Phi_0 = h/2e$ is the flux quantum with h the Planck constant and e the elementary charge. Note that, in a superconductor smaller than the penetration depth, the fluxoid, which contains an integration of the supercurrent along a closed path, is quantized, rather than the flux. For a spin-triplet equal-spin pairing (ESP) superconductor, the wavefunction $\psi_T = |\Delta_T|(-e^{i\theta_\uparrow}|\uparrow\uparrow\rangle + e^{i\theta_\downarrow}|\downarrow\downarrow\rangle)$ has two phase degrees of freedom. In an ESP ring, half-integer quantization $\Phi' = n'\Phi_0$ with $n' = \pm 1/2, \pm 3/2, \cdots$ is allowed even under the constraint of the single-valuedness of the wave function. Such a fluxoid state is called the HQF state.

One of the materials that can host the HQF is Sr_2RuO_4, which is a leading candidate spin-triplet ESP superconductor [9, 10]. This oxide has a layered perovskite structure and exhibits superconductivity below 1.5 K. Various experiments have provided firm evidence for the spin-triplet ESP state [11–18], but there still are several issues that cannot be understood within the current spin-triplet scenario [19–23]. Also, signatures of HQF have been observed in microstructured Sr_2RuO_4 rings using cantilever magnetometry [24]. Still, in order to come to Majorana braiding, electrical detection of the HQF state is required.

For this, small samples are necessary in order to reduce the spin-current energy of the HQF state, as pointed out by Chung *et al.* [25]. The role of the Zeeman field to lower the kinetic energy of a HQF state is discussed by Vakaryuk and Leggett [26]. Accordingly, a transition from IQF to HQF is expected to occur with increasing in-plane field, with free-energy minima for the HQF states appearing in the middle of neighboring IQF states [Fig. 6.1(a)]. There is a proposal for detection of HQF using perforated films [27]; here we use a simpler system of a ring shape. It should also be mentioned that a superconducting state can exist with an enhanced transition

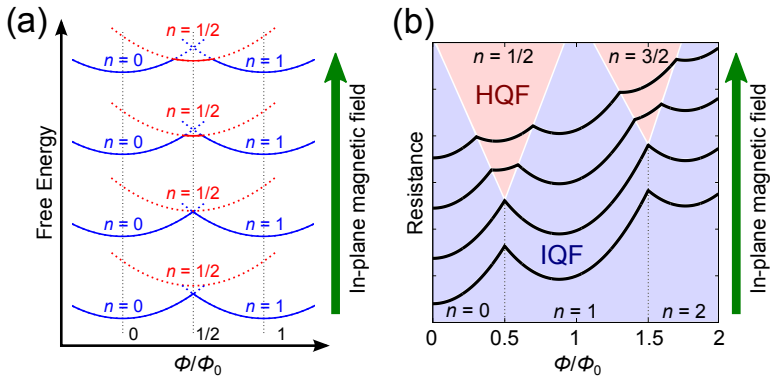

Figure 6.1: (a) Schematic profile of the free energies for IQF states and a HQF state. A HQF state may become energetically favorable under in-plane magnetic field; it is realized above a threshold in-plane field value. (b) Expected change of the magnetoresistance oscillations. Peak splittings with in-plane field are expected when HQF states are realized.

temperature, the so-called 3-K phase. This is observed in eutectic crystals [28–30] or in bulk crystals under uniaxial strain [31–33].

Fluxoid quantization can be investigated by measuring magnetoresistance oscillations as a function of a field applied along the axis of the ring in the regime of the resistive transition, known as the Little-Parks (LP) oscillations [34]. The LP oscillations originate from the oscillations in the free energy and hence in the transition temperature T_c, caused by field-induced supercurrents that flow to satisfy the quantization condition. Then the magnetoresistance curve should trace the field dependence of the free energy [Fig. 6.1]. Thus, a resistance peak in the LP oscillations, located at the border of two neighboring IQF states, should split when HQF states are realized, as shown in Fig. 6.1(b). There are indications that the order parameter in the 3-K phase is not ESP [33, 35]. However, the LP oscillations are robust, regardless of the pairing symmetry or the number of components of the order parameter.

Although techniques to detect the LP oscillations have been developed over the past 50 years, all reported experiments have been performed using superconducting films. To the best of our knowledge, there is no report of the observation of proper LP oscillations even for IQF in a ring made of bulk single crystals, including Sr_2RuO_4. For Sr_2RuO_4, although its superconducting thin films have been reported [36, 37], films with strong and homogeneous superconductivity are still virtually absent. Therefore, for LP experiments, techniques to make micro rings without using thin films are needed. Recently, Cai *et al.* reported observation of magnetoresistance oscillations in micro rings made of single-crystalline Sr_2RuO_4 [38, 39]. However, the oscillation amplitudes were substantially larger than the LP expectation.

Here, we report the first observation of proper Little-Parks oscillations in micro rings

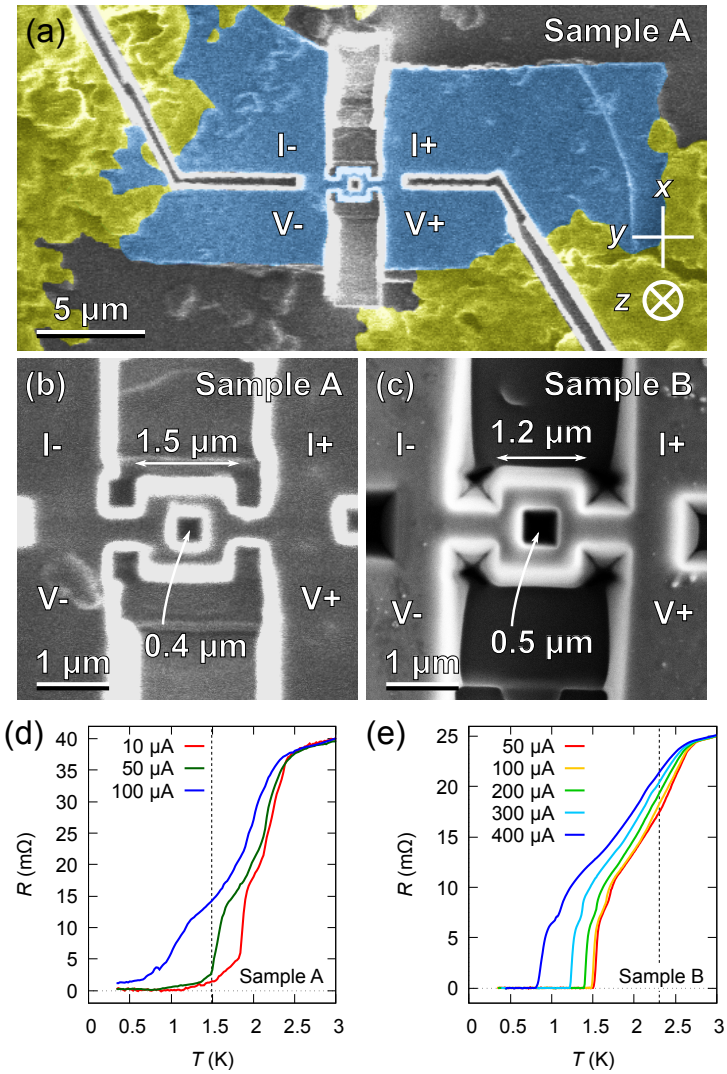

Figure 6.2: (a) False-colored scanning ion microscope (SIM) image of Sample A (yy075). The blue- and yellow-colored regions are the Sr_2RuO_4 crystal and the silver paint, respectively. (b) Magnified SIM image of Sample A. (c) Scanning electron microscope (SEM) image of Sample B (yy150). The thickness of Samples A and B are 1.3 and 2.0 μm, respectively. Resistance of (d) Sample A and (e) Sample B as functions of temperature. Both rings show superconducting transition above 1.5 K and several other transition steps. The dashed lines indicate the temperatures at which the magnetoresistance and magnetovoltage shown in Fig. 6.3 are measured.

of single-crystalline Sr_2RuO_4. With in-plane fields, we observed two different kinds of peak splittings of the LP oscillations: after careful examination of the raw voltage, we conclude that the splitting in small in-plane fields is extrinsic, originating from asymmetry in the current-voltage characteristics; whereas the splitting in larger in-

plane fields, observable also in the raw voltage, is intrinsic.

6.2. RESULTS AND DISCUSSION

In this study, Sr_2RuO_4 single crystals grown with the floating-zone method [40] were used for micro rings.Before the fabrication, T_c of the crystal C391, used for Sample B, was confirmed to be 1.50 K [Fig. S4] using AC susceptibility method (Quantum Design, PPMS adiabatic demagnetization refrigerator option) [41]. A 1-μm-thin crystal was selected among crushed single crystals, and it was placed on a $SrTiO_3$ substrate, which has a thermal contraction matching with that of Sr_2RuO_4. (For Sample A, however, a sapphire substrate with a smaller thermal contraction was used). The surface of the crystal was protected by evaporating a thin layer of SiO_2 after electrodes of high-temperature-cure silver paint (Dupont, 6836) are provided.To fabricate rings with a four-terminal configuration [Figs. 6.2(a)-(c)], the Ga-based focused ion beam (FIB) technique was used with a 20-pA and 30-kV beam. The rings were cooled down to 0.3 K with a ^{3}He refrigerator (Oxford Instruments, Heliox). To avoid influence of thermoelectric voltage, the resistance was measured under DC current with sign flip: We measure voltage under positive current $V_+ = V(+I)$ and under negative current $V_- = V(-I)$, and evaluate the resistance R as $R = (V_+ - V_-)/2I$. To investigate the field dependence, however, it is crucially important to examine V_+ and V_- individually since LP oscillations are not necessarily invariant under reflection, as seen below. In other words, it is essential to examine magnetovoltage rather than magnetoresistance. Temperature stability during a magnetotransport measurement is approximately 100 μK. This value is substantially smaller than the expected transition-temperature shift due to the LP oscillations, estimated to be around 10 mK. The magnetic field was applied with a three-axes superconducting vector magnet (1 T / 0.2 T / 0.2 T), allowing us to control the out-of-plane and in-plane fields independently. More details on the experimental method are described on the Supplemental Material [42].

Figures 6.2(d) and (e) show the temperature dependence of the ring resistance $R(T)$. Zero resistance due to superconductivity was observed in both rings. Note that the superconducting transitions start well above 1.5 K. This is a signature of the 3-K phase, which is induced in our rings probably by local strain, caused by the FIB process. Several transition steps are observed in both rings. Each step corresponds to the transition of a certain region of the device, as demonstrated in a LP experiment using a conventional superconductor [43]. Still, the correspondence is not entirely straightforward and we rather identify the contribution from the ring by finding the temperature regime where field-induced resistance oscillations occur. In Sample A this is around 1.5 K. In Sample B it is around 2.5 K, while the transitions below 2 K probably are connected to the neck part and the contact part of the structure [Fig. S6].

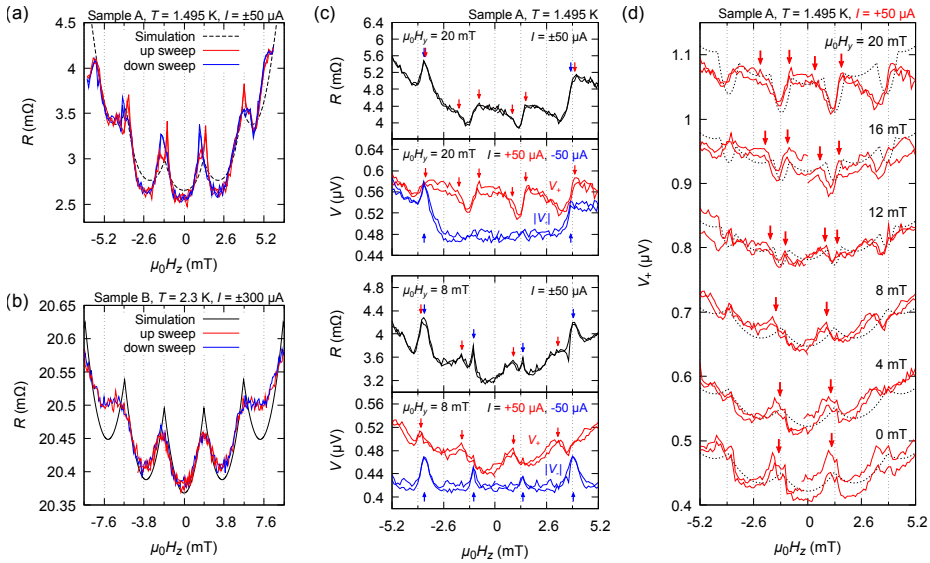

Figure 6.3: Magnetoresistance $R(H_z)$ of (a) Sample A and (b) Sample B without in-plane fields. Both oscillatory periods and amplitudes agree with those of simulations for the Little-Parks oscillations. (c) Comparison of resistance and voltage as functions of H_z for up-sweeps at 0.3 mT/min under constant in-plane fields H_y. At $\mu_0 H_y = 8$ mT, the difference in the peak positions in $V_+(H_z)$ and $V_-(H_z)$ results in apparent resistance-peak-splitting because the resistance is evaluated as $(V_+(H_z) - V_-(H_z))/2I$. For $\mu_0 H_y = 20$ mT, however, dips at $\mu_0 H_z = \pm 1.3$ mT are clearly observed even in the raw voltage V_+. Hence the HQF dips in the resistance is not an artifact originating from averaging. Note that for V_-, its absolute values $|V_-|$ are plotted with vertical offsets. (d) Effects of in-plane magnetic field H_y on the magnetovoltage $V_+(H_z)$ of Sample A, including the data shown in (c). Magnetovoltage peaks split above $\mu_0 H_y = 12$ mT as indicated with arrows, and the width of the splitting becomes wider with increasing H_y, as expected for HQF states. Measurements are repeated twice in each conditions to demonstrate good reproducibility. Each set of curves has a 0.1-μV offset for clarity. The dashed curves are guide to the eye.

The magnetoresistance of the rings in the regions of the resistive transitions is shown in Figs. 6.3(a) and (b). The measurements were performed at fixed temperatures indicated with dashed lines in Figs. 6.2(d) and (e). The samples were heated above 5 K before each measurement, then cooled under zero magnetic field. Periodic oscillations were observed with periods $\mu_0 \Delta H = 2.6$ mT and 3.8 mT for Samples A and B, respectively. From ΔH, we can estimate the area S that causes the oscillations by using the relation $\Phi_0 = \mu_0 \Delta H \cdot S$. As a result, we obtain $S_{\mathrm{SampleA}} = 0.80\ \mu\mathrm{m}^2$ and $S_{\mathrm{SampleB}} = 0.54\ \mu\mathrm{m}^2$, which agree well with the geometry of the rings.

Next, we quantitatively evaluate the oscillations. The shift of T_c due to the fluxoid quantization is given by [44]

$$\frac{T_c(H) - T_c(0)}{T_c(0)} = -\left(\frac{\pi \xi_0 w \mu_0 H}{\sqrt{3}\Phi_0}\right)^2 - \frac{\xi_0^2}{r_1 r_2}\left(n - \frac{\pi \mu_0 H r_1 r_2}{\Phi_0}\right)^2, \tag{6.1}$$

where ξ_0 is the coherence length at 0 K, r_1 is the inner radius, r_2 is the outer radius, and $w = r_2 - r_1$ is the width of a ring. In our calculation, $\xi_0 = 66$ nm (the coherence length along the ab-plane of Sr_2RuO_4 [10]), while we chose $2r_1 = 0.75\ \mu$m, $2r_2 =$

1.4 μm for Sample A, and $2r_1 = 0.7$ μm, $2r_2 = 1.0$ μm for Sample B. Note that the samples are somewhat "conical", with a smaller top and larger bottom. To convert the T_c shift to a resistance shift, we assume that the shape of a $R(T)$ curve does not change under magnetic field, and the curve shifts to the left by $T_c(0) - T_c(H_z)$. As presented in Figs 6.3(a) and (b) the obtained $R(H_z)$ simulations agree well with the experimental results without any adjustable parameters. We observed oscillations corresponding to $|n| \leq 5$ for Sample A and $|n| \leq 3$ for Sample B. This is because the parabolic component due to the Meissner effect (the first term in Eq. (1)) is dominant at a high field region, and the oscillation component (the second term in Eq. (1)) is not resolved. Though a modulation of the oscillatory period is known in a wide-arm ring [45], we do not observe such non-periodic oscillations. We emphasize again that we succeeded in observing the LP oscillations using a bulk single crystal unlike the other reported LP experiments using superconducting films [46]. Thus, the first conclusion of this paper is that the magnetoresistance oscillations observed in both Sr_2RuO_4 micro rings are the proper LP oscillations.

We then performed magnetotransport measurements with additional in-plane magnetic fields H_y (which is along the current direction). The magnetoresistance as well as the raw voltages V_+ and V_- for $\mu_0 H_y = 8$ and 20 mT are shown in Fig. 6.3(c). The out-of-plane magnetic field values were corrected for the misalignment of the rings with respect to the magnets. To be specific, the actual out-of-plane field H_z is given by $H_z = H_z^{\mathrm{magnet}} \cos\theta + H_y^{\mathrm{magnet}} \sin\theta + H_z^{\mathrm{remnant}}$, where the misalignment angle $\theta = 0.86°$ and the remnant field $H_z^{\mathrm{remnant}} = -0.3$ mT are chosen so that the peaks are located at the same $|H_z|$ value [1].

For $\mu_0 H_y = 8$ mT, the magnetoresistance $R(H_z)$ peaks appear split at $\mu_0 H_z = \pm 1.3$ mT, which correnpond to the transition fields between $n = 0$ and $n = \pm 1$ fluxoid states. However, this peak splitting is not observed in the magnetovoltage $V_+(H_z)$ or $V_-(H_z)$. Instead, the peaks for $V_+(H_z)$ and $V_-(H_z)$ emerge at different H_z. Notice that, the resistance is obtained from an average of V_+ and $-V_-$. As a result, the difference of the peak position in $V_+(H_z)$ and $-V_-(H_z)$ causes artifact peak splitting in the magnetoresistance. Thus, to find an intrinsic peak splitting originating from HQFs, not only $R(H_z)$ but also $V_+(H_z)$ and $V_-(H_z)$ data should be carefully examined: current-averaged resistance data may cause misinterpretation of experimental results.

For $\mu_0 H_y = 20$ mT the situation is different. In this case the splitting in $R(H_z)$ is also observed in $V_+(H_z)$ (see the top two panels of Fig. 6.3(c)). Thus, this splitting is not an artifact originating from the asymmetric peaks in $V_+(H_z)$ and $V_-(H_z)$. In the rest of this paper, we focus on this splitting in the magnetovoltage.

[1] In-plane field value is also corrected using $H_y = H_y^{\mathrm{magnet}} \cos\theta - H_z^{\mathrm{magnet}} \sin\theta$. The mixed component $\mu_0 H_z^{\mathrm{magnet}} \sin\theta$ is only 0.078 mT even at the highest H_z^{magnet} value, which is comparable with the geomagnetic field (~0.05 mT). Therefore, the in-plane magnetic field can be regarded as constant during the H_z sweep.

Figure 6.3(d) shows the $V_+(H_z)$ with 4-mT H_y steps. Under zero in-plane magnetic field, the oscillations are consistent with the ordinary LP magnetovoltage oscillations with a period corresponding to Φ_0. When the in-plane field is applied above 12 mT, the peaks in $V_+(H_z)$ clearly start to split. Furthermore, the width of the splitting becomes larger with increasing in-plane field. The increased splitting is consistent with the expectation that the free energy of a HQF state becomes smaller under the in-plane field, as shown in Fig. 6.1. Interestingly, the dips at $\mu_0 H_z = \pm 1.3$ mT for $\mu_0 H_y = 20$ mT are even deeper than the voltage bottoms of the IQF states. Within the HQF scenario, this suggests that the energy of HQF states can become smaller than that of IQF states. We emphasize that the results are well reproducible. The measurements were repeated twice in each condition, and the obtained curves precisely match each other. Magnetoresistance measurements with another in-plane field direction and on Sample B were also performed [42]. For Sample B we do not see signatures of the HQF state in the field range where we expect them, although some sort of splitting occurs above 150 mT.

It may be argued that, if several transition steps in $R(T)$ contribute to the $V_+(H_z)$ and $V_-(H_z)$, the voltages may exhibit a complicated shape resembling that of a HQF state. However, even with 20 mT in-plane field, the resistance is still lower than 6 mΩ as shown in the upper panel of Fig. 6.3(c). Figure 6.2(d) shows that the resistance corresponding to the lowest-temperature transition is $R < 10$ mΩ. Therefore, magnetoresistance measurements were always performed at the sharp transition region occurring around 1.5 K and the higher-temperature transitions do not contribute the magneto-transport.

Let us here compare our results with the previous cantilever magnetometry study by Jang *et al.* [24].Their measurements were performed at 0.6 K, much lower than T_c. In contrast, our experiment was conducted around T_c to measure finite resistance/voltage. Besides, the measurement current may interact with the circulating supercurrent in our measurements. In spite of these differences, additional features at $\pm\Phi_0/2$ are present in both experiments. Moreover, in both cases the HQF features are only observed with $\mu_0 H_y$ above around 10 mT.Together, the data suggest that the HQF states are very likely to be intrinsic to Sr_2RuO_4.

There are still issues to be resolved. First, hysteresis is observed in the H_z sweep [Figs. S6-S9]. Such hysteresis between fluxoid states may occur because of the metastable branches in the free energy (dotted parts of the curves in Fig. 6.1(a)). Nevertheless, a detailed mechanism for the asymmetric hysteresis especially at large H_y is still unclear. We comment here that similar hysteresis was also observed in the torque experiment [24].Second, the splittings of the magnetovoltage peaks for positive H_y are observed only in V_+ but not in V_-.Nevertheless, for negative H_y, peaks in V_- show splitting but not in V_+ [Figs. S6 and S7].This result ensures the expected symmetry under the concurrent inversion of magnetic field and current: $\boldsymbol{H} \to -\boldsymbol{H}$

and $\boldsymbol{I} \to -\boldsymbol{I}$, $V_{\pm}(\boldsymbol{H}) \simeq -V_{\mp}(-\boldsymbol{H})$. On the other hand, the dips in voltages are affected under y-direction field inversion: $H_y \to -H_y$, $V_{\pm}(H_z, H_y) \neq V_{\pm}(H_z, -H_y)$.Perhaps, one needs to consider the role played by the geometrical asymmetry, for example inhomogeneity in T_c or difference in the effective width between the positive- and negative-x halves of the ring.Finally, the question can be raised why we do not observe the large magnetoresistance oscillations seen by Cai *et al.* [38, 39].We have also investigated circular rings (rather than the square ones discussed here), and observed no LP oscillations but large amplitude magnetoresistance oscillations.A detailed comparison and its possible origin will be discussed in a subsequent paper.

In conclusion, we have observed the LP oscillations with expected amplitudes and periods in micro rings of Sr_2RuO_4. This is the first report of the LP oscillations using any bulk single-crystal superconductor. Furthermore, by applying in-plane magnetic fields, we observed splitting of the peaks of the LP magnetovoltage oscillations. The widening of the splitting with increasing in-plane field agrees with the expectation for the HQF state.

REFERENCES

[1] X.-L. Qi and S.-C. Zhang, *Rev. Mod. Phys.* **83**, 1057 (2011).

[2] D. A. Ivanov, *Phys. Rev. Lett.* **86**, 268 (2001).

[3] M. Stone and S. B. Chung, *Phys. Rev. B* **73**, 014505 (2006).

[4] V. Mourik, K. Zuo, S. M. Frolov, S. R. Plissard, E. P. A. M. Bakkers, and L. P. Kouwenhoven, *Science* **336**, 1003 (2012).

[5] S. Nadj-Perge, I. K. Drozdov, J. Li, H. Chen, S. Jeon, J. Seo, A. H. MacDonald, B. A. Bernevig, and A. Yazdani, *Science* **346**, 602 (2014).

[6] G. Volovik and V. Mineev, *JETP Letters* **24**, 561 (1976).

[7] N. Read and D. Green, *Phys. Rev. B* **61**, 10267 (2000).

[8] C. Kallin and J. Berlinsky, *Reports on Progress in Physics* **79**, 054502 (2016).

[9] A. P. Mackenzie and Y. Maeno, *Rev. Mod. Phys.* **75**, 657 (2003).

[10] Y. Maeno, S. Kittaka, T. Nomura, S. Yonezawa, and K. Ishida, *J. Phys. Soc. Jpn.* **81**, 011009 (2012).

[11] K. Ishida, H. Mukuda, Y. Kitaoka, K. Asayama, Z. Q. Mao, Y. Mori, and Y. Maeno, *Nature* **396**, 658 (1998).

[12] G. Luke, Y. Fudamoto, K. Kojima, M. Larkin, J. Merrin, B. Nachumi, Y. Uemura, Y. Maeno, Z. Mao, Y. Mori, H. Nakamura, and M. Sigrist, *Nature* **394**, 558 (1998).

[13] J. A. Duffy, S. M. Hayden, Y. Maeno, Z. Mao, J. Kulda, and G. J. McIntyre, *Phys. Rev. Lett.* **85**, 5412 (2000).

[14] J. Xia, Y. Maeno, P. T. Beyersdorf, M. M. Fejer, and A. Kapitulnik, *Phys. Rev. Lett.* **97**, 167002 (2006).

[15] S. Kashiwaya, H. Kashiwaya, H. Kambara, T. Furuta, H. Yaguchi, Y. Tanaka, and Y. Maeno, *Phys. Rev. Lett.* **107**, 077003 (2011).

[16] M. S. Anwar, S. R. Lee, R. Ishiguro, Y. Sugimoto, Y. Tano, S. J. Kang, Y. J. Shin, S. Yonezawa, D. Manske, H. Takayanagi, T. W. Noh, and Y. Maeno, *Nat. Commun.* **7**, 13220 (2016).

[17] M. Manago, K. Ishida, Z. Mao, and Y. Maeno, *Phys. Rev. B* **94**, 180507 (2016).

[18] M. Manago, T. Yamanaka, K. Ishida, Z. Mao, and Y. Maeno, *Phys. Rev. B* **94**, 144511 (2016).

[19] C. W. Hicks, J. R. Kirtley, T. M. Lippman, N. C. Koshnick, M. E. Huber, Y. Maeno, W. M. Yuhasz, M. B. Maple, and K. A. Moler, *Phys. Rev. B* **81**, 214501 (2010).

[20] S. Yonezawa, T. Kajikawa, and Y. Maeno, *Phys. Rev. Lett.* **110**, 077003 (2013).

[21] S. Yonezawa, T. Kajikawa, and Y. Maeno, *J. Phys. Soc. Jpn.* **83**, 083706 (2014).

[22] S. Kittaka, A. Kasahara, T. Sakakibara, D. Shibata, S. Yonezawa, Y. Maeno, K. Tenya, and K. Machida, *Phys. Rev. B* **90**, 220502 (2014).

[23] E. Hassinger, P. Bourgeois-Hope, H. Taniguchi, S. René de Cotret, G. Grissonnanche, M. S. Anwar, Y. Maeno, N. Doiron-Leyraud, and L. Taillefer, *Phys. Rev. X* **7**, 011032 (2017).

[24] J. Jang, D. G. Ferguson, V. Vakaryuk, R. Budakian, S. B. Chung, P. M. Goldbart, and Y. Maeno, *Science* **331**, 186 (2011).

[25] S. B. Chung, H. Bluhm, and E.-A. Kim, *Phys. Rev. Lett.* **99**, 197002 (2007).

[26] V. Vakaryuk and A. J. Leggett, *Phys. Rev. Lett.* **103**, 057003 (2009).

[27] V. Vakaryuk and V. Vinokur, *Phys. Rev. Lett.* **107**, 037003 (2011).

[28] Y. Maeno, T. Ando, Y. Mori, E. Ohmichi, S. Ikeda, S. NishiZaki, and S. Nakatsuji, *Phys. Rev. Lett.* **81**, 3765 (1998).

[29] M. S. Anwar, T. Nakamura, S. Yonezawa, M. Yakabe, R. Ishiguro, H. Takayanagi, and Y. Maeno, *Scientific Reports* **3**, 2480 (2013).

[30] Y. Ying, N. Staley, Y. Xin, K. Sun, X. Cai, D. Fobes, T. Liu, Z. Mao, and Y. Liu, *Nat. Commun.* **4** (2013).

[31] S. Kittaka, H. Taniguchi, S. Yonezawa, H. Yaguchi, and Y. Maeno, *Phys. Rev. B* **81**, 180510 (2010).

[32] C. W. Hicks, D. O. Brodsky, E. A. Yelland, A. S. Gibbs, J. A. N. Bruin, M. E. Barber, S. D. Edkins, K. Nishimura, S. Yonezawa, Y. Maeno, and A. P. Mackenzie, *Science* **344**, 283 (2014).

[33] A. Steppke, L. Zhao, M. E. Barber, T. Scaffidi, F. Jerzembeck, H. Rosner, A. S. Gibbs, Y. Maeno, S. H. Simon, A. P. Mackenzie, and C. W. Hicks, *Science* **355**, eaaf9398 (2017).

[34] W. A. Little and R. D. Parks, *Phys. Rev. Lett.* **9**, 9 (1962).

[35] M. S. Anwar, R. Ishiguro, T. Nakamura, M. Yakabe, S. Yonezawa, H. Takayanagi, and Y. Maeno, *Phys. Rev. B* **95**, 224509 (2017).

[36] Y. Krockenberger, M. Uchida, K. Takahashi, M. Nakamura, M. Kawasaki, and Y. Tokura, *Appl. Phys. Lett.* **97**, 2502 (2010).

[37] J. Cao, D. Massarotti, M. E. Vickers, A. Kursumovic, A. D. Bernardo, J. W. A. Robinson, F. Tafuri, J. L. MacManus-Driscoll, and M. G. Blamire, *Supercond. Sci. Technol.* **29**, 095005 (2016).

[38] X. Cai, Y. A. Ying, N. E. Staley, Y. Xin, D. Fobes, T. J. Liu, Z. Q. Mao, and Y. Liu, *Phys. Rev. B* **87**, 081104 (2013).

[39] X. Cai, Y. Ying, B. Zakrzewski, D. Fobes, T. Liu, Z. Mao, and Y. Liu, *arXiv:1507.00326*.

[40] Z. Mao, Y. Maeno, and H. Fukazawa, *Mater. Res. Bull.* **35**, 1813 (2000).

[41] S. Yonezawa, T. Higuchi, Y. Sugimoto, C. Sow, and Y. Maeno, *Rev. Sci. Instrum.* **86**, 093903 (2015).

[42] See Supplemental Material [url] for the details of device fabrication process and additional results to support the conclusion of the main paper, which includes Refs. [48–52].

[43] G. R. Berdiyorov, S. H. Yu, Z. L. Xiao, F. M. Peeters, J. Hua, A. Imre, and W. K. Kwok, *Phys. Rev. B* **80**, 064511 (2009).

[44] V. V. Moshchalkov, L. Gielen, C. Strunk, R. Jonckheere, X. Qiu, C. V. Haesendonck, and Y. Bruynseraede, *Nature* **373**, 319 (1995).

[45] M. Morelle, D. S. Golubović, and V. V. Moshchalkov, *Physical Review B* **70**, 144528 (2004).

[46] V. V. Moshchalkov and J. Fritzsche, *Nanostructured Superconductors* (World Scientific Publishing, 2011), and the references there in.

[47] In-plane field value is also corrected using $H_y = H_y^{\mathrm{magnet}} \cos\theta - H_z^{\mathrm{magnet}} \sin\theta$. The mixed component $\mu_0 H_z^{\mathrm{magnet}} \sin\theta$ is only 0.078 mT even at the highest H_z^{magnet} value, which is comparable with the geomagnetic field (~0.05 mT). Therefore, the in-plane magnetic field can be regarded as constant during the H_z sweep.

[48] R. Loetzsch, A. Lübcke, I. Uschmann, E. Förster, V. Große, M. Thuerk, T. Koettig, F. Schmidl, and P. Seidel, *Appl. Phys. Lett.* **96**, 1901 (2010).

[49] O. Chmaissem, J. D. Jorgensen, H. Shaked, S. Ikeda, and Y. Maeno, *Phys. Rev. B* **57**, 5067 (1998).

[50] M. Lucht, M. Lerche, H.-C. Wille, Y. V. Shvyd'Ko, H. Rüter, E. Gerdau, and P. Becker, *J. Appl. Cryst.* **36**, 1075 (2003).

[51] D. Batchelder and R. Simmons, *J. Chem. Phys.* **41**, 2324 (1964).

[52] A. P. Mackenzie, R. K. W. Haselwimmer, A. W. Tyler, G. G. Lonzarich, Y. Mori, S. Nishizaki, and Y. Maeno, *Phys. Rev. Lett.* **80**, 161 (1998).

7

Spontaneous emergence of Josephson junctions in single-crystal Sr_2RuO_4

Yuuki Yasui†, Kaveh Lahabi†, Victor Fernández Becerra, Muhammad Shahbaz Anwar, Shingo Yonezawa, Takahito Terashima, Milorad V. Milošević, Jan Aarts & Yoshiteru Maeno

This work is to be submitted for publication.

† These authors contributed equally to this work.

Author contributions: The crystals were grown in the group of Y. Maeno at Kyoto University. K. Lahabi FIB-structured the crystals that were prepared by Y. Yasui. Y. Yasui performed the transport measurements. M. S. Anwar took part in the discussion. S. Yonezawa and Y. Maeno supervised the measurements. K. Lahabi and Y. Yasui analysed the results. K. Lahabi formulated the discussion presented in Section 7.4. Y. Yasui modelled the Little-Parks oscillations. V. F. Becerra and M. V. Milošević (University of Antwerp) carried out the TDGL simulations; and aided with the theoretical input. K. Lahabi and Y. Yasui wrote the paper with inputs from all the authors.

7.1. GENERAL INTRODUCTION

THE OXIDE Sr_2RuO_4 stands out among the unconventional superconductors as one of the very few materials with spin-triplet pairing and broken time-reversal symmetry [1, 2]. The tetragonal crystal structure allows five unitary representations for a p-wave pairing symmetry [1, 3]. One of these is the chiral order parameter, of the form $p_x \pm i p_y$, which is strongly suggested by muon spin relaxation [4] and high-resolution polar Kerr effect measurements [5] (see Section 2.2.3).This equal-spin pairing state is attracting renewed attention due to the possibility that it can host Majorana bound states, which in turn are of interest for topological quantum computing [6–8]. A key property of the chiral state is its double degeneracy in the orbital degree of freedom, with important consequences such as the emergence of domains of different chirality and the existence of an edge current.

The major hurdle plaguing our understanding of Sr_2RuO_4 is that, although the chiral state seems probable, domains or edges currents have not been observed directly [9]. Indications for their existence however have been found in transport experiments, which utilize Ru inclusions to form proximity junctions between Sr_2RuO_4 and a conventional s-wave superconductor (see Figure 7.1**a-c**). These systems exhibit highly unconventional transport properties, which have been attributed to the presence of chiral domains [10, 11]. Typical examples of this are presented in Figure 7.1. A complication in the physics of Sr_2RuO_4 is that, by lifting the tetragonal crystal symmetry, the Ru inclusions, or uniaxial strain in general, can induce a different superconducting state [12, 13] with an enhanced $T_c \approx 3$ K. Recent studies suggest that this "extrinsic" phase (also known as the 3 K-phase) may have an even-parity order parameter, and is most likely non-chiral (i.e. single-component)[1] [14, 15]. The exact pairing symmetry of this state is yet to be determined, however, this means that transport experiments have so far been conducted on hybrids of S-Ru-Sr_2RuO_4(extrinsic)-Sr_2RuO_4(intrinsic)-Sr_2RuO_4(extrinsic)-Ru-S. While such hybrids are fascinating on their own merits, their capacity to directly inform us on the unspoiled chiral phase is limited.

More importantly, the vast majority of studies of the past two decades have been limited to bulk Sr_2RuO_4 crystals, typically hundreds of microns in dimension. This is mainly due to the absence of thin superconducting Sr_2RuO_4 films. The domains, however, are expected to be no more than a few microns in size, and to have an arbitrary arrangement (presumably pinned by random defects in the lattice) [16, 17]. Moreover, the time-dependent "telegraph noise" which is in observed in transport measurements suggests the domains are mobile [10, 11].

[1] In this chapter we refer to the superconducting phase at 1.5 K, which corresponds to the multi-component (i.e. chiral) order parameter proposed for pure Sr_2RuO_4 as intrinsic, and the possible single-component phase, characterized by a broad transition at $T \approx 3$ K (strain-induced), as extrinsic.

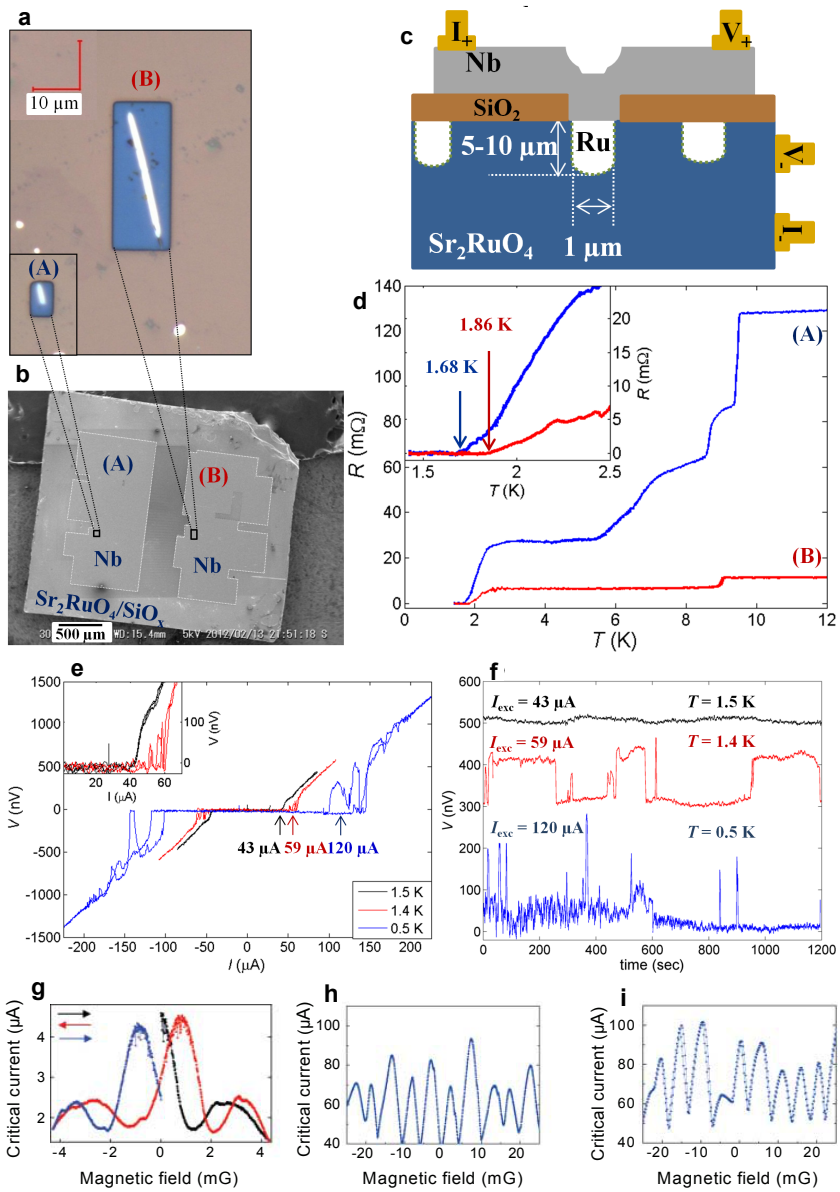

Figure 7.1: Examples from previous transport experiments. **a** Ru inclusions, used for making electrical contact with Sr_2RuO_4. **b** a typical Sr_2RuO_4 crystal used in transport experiments. The dimensions are of the order of a few millimeters. **c** schematic of a Sr_2RuO_4 proximity junction. **d** multistage $R(T)$ transitions, typical for Sr_2RuO_4 proximity junctions. The characteristic feature of these systems is the broad transition observed around 2.5-3 K, corresponding to the extrinsic phase that forms around Ru inclusions. **e,f** switching of voltage. The "telegraphic noise" appears under a d.c. current bias, and has been attributed to current-excited chiral domain wall (ChDW) motion (**a-f** reproduced from Ref. [10]). **g** example of a hysteretic interference pattern, suggesting field-induced ChDW motion. **h-i** change of interference pattern in the same device at different thermal cycles, suggesting the reconfiguration of ChDWs (**g-i** reproduced from Ref. [11]).

The stochastic arrangement of the domains, combined with the unavoidable presence of an extrinsic phase (around the Ru contacts), introduce an inherent uncertainty in the analysis of such experiments. This also means that theoretical calculations cannot predict a unique outcome for a given transport measurement. We avoid these restrictions by implementing a new approach to directly probe nanostructured Sr_2RuO_4 crystals with a homogenous phase, that can be either extrinsic or intrinsic. This enables us to examine each phase separately (in different samples), and compare their behaviour. We show that the use of high-quality nanostructures, combined with time-dependent Ginzburg-Landau (TDGL) simulations, provides a powerful tool for the study chiral of superconductivity in a controllable manner, where theoretical predictions can be directly verified by transport experiments.

7.2. INTRODUCTION

Mesoscopic structures of a chiral p-wave superconductor are expected to host multichiral states [18], where the two $p_x \pm i p_y$ chiral components of the order parameter segregate into domains, separated by a chiral domain wall (ChDW). On the other hand, the energy cost associated with a ChDW grows per area [17]. This makes mesoscopic structures a promising platform to verify, and potentially control the domains. Another remarkable aspect of a ChDW is that it can act as a Josephson junction [17] by locally suppressing the condensate between the two chiral states, as shown in Figure 7.2. What makes this particularly significant is that, depending on its orientation relative to the transport direction, a ChDW junction could have a nontrivial Josephson phase ϕ, where $0 < \phi < \pi$ [17].

Here we present the results of transport measurements on mesoscopic rings of Sr_2RuO_4, prepared by focused ion beam (FIB) milling of single crystals. Homogeneous structures with an intrinsic phase, characterized by a sharp transition at 1.5 K, show a distinct critical current oscillation—similar to that of the classical dc superconducting quantum interference device (SQUID), with two artificially prepared Josephson junctions. Despite the absence of conventional weak links, the oscillations persist over a surprisingly wide temperature range (well below T_c) while maintaining their overall shape. Interestingly, this behavior is entirely absent in structures that are in the extrinsic phase. These systems behave as standard superconducting loops: they exhibit conventional T_c oscillations (i.e. Little-Parks) which can only be observed near the transition [19]. We also present data from calculations of possible chiral configurations in the ground state of a p-wave superconducting ring, using the Ginzburg-Landau formalism. Experiments and calculations together make a convincing case for two chiral domain walls being present in the two arms of the ring, leading to the observed SQUID-like behavior.

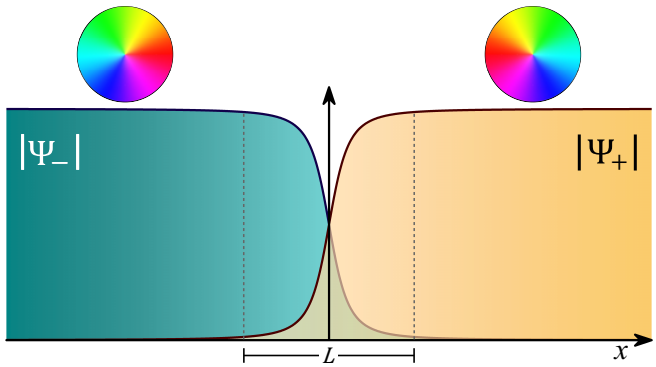

Figure 7.2: **Schematic of a chiral domain wall**. Ψ_- and Ψ_+ correspond to the chiral states $p_x - ip_y$ and $p_x + ip_y$, which meet at the ChDW. A Josephson junction is formed as the two chiral components overlap over a finite distance $L \propto \xi$, and induce a local suppression of the superconducting condensate. The colour wheels represent the orbital phase of each chiral component.

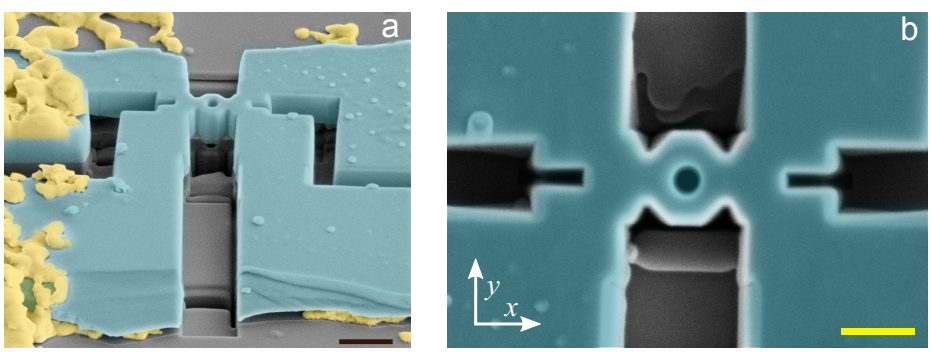

Figure 7.3: **Falsed-color scanning electron microscope image of the ring yy146.** **a** blue and yellow, respectively, represent the Sr_2RuO_4 crystal and the silver epoxy used for making electrical contact. The ring is connected to four transport leads, and is sculpted out of a 0.7 μm thick crystal by a Ga^+ focused ion beam. The surface of the crystal is protected by a 100 nm SiO_x layer. **b**, close-up of the ring. The outer radius is 1.1 μm, and the inner radius is at least 0.2 μm. The dark and yellow scale bars correspond to 2 μ m and 1 μ m, respectively.

7.3. RESULTS

7.3.1. BASIC TRANSPORT PROPERTIES

Single crystals of Sr_2RuO_4 were grown with the floating zone method [20] and structured into microrings using Ga-based FIB etching. Figure 7.3 show scanning electron microscope (SEM) images of such a ring (called yy146), with an inner radius r_{in} of 200 nm (minimum), an outer radius r_{out} of 550 nm, and a thickness of 700 nm.

The temperature-dependent resistance $R(T)$ of this ring, presented in Figure 7.4 **a**, shows a rather sharp superconducting transition.The high quality of the sample is

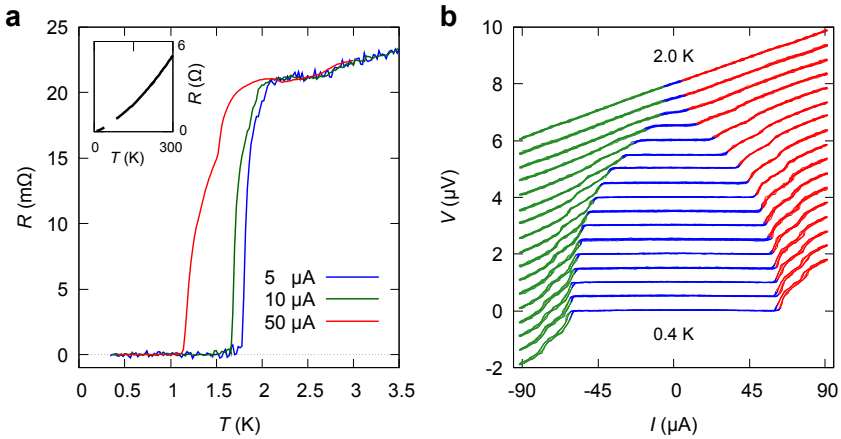

Figure 7.4: Basic transport properties of sample yy146. **a** resistance as a function of temperature R(T) measured with different d.c. currents. The insets show R(T) in a wider temperature range. The ratio of residual resistivity (RRR) is 238. **b** current-voltage ($I-V$) characteristics for the temperature range between 2 K and 0.4 K, measured in steps of 0.1 K. The colours green, blue and red correspond to voltages $V < -0.1$ μV, -0.1 μV $< V <$ 0.1 μV and 0.1 μV $< V$, respectively. The curves are offset from each other for clarity. At each temperature, the curve consists of multiple $I-V$ traces, measured while sweeping the d.c. bias in both directions as $0 \rightarrow I^+ \rightarrow I^- \rightarrow I^+$ in repeated scans.

evident by its particularly high residual resistivity ratio (RRR = 238). Comparing Figure 7.4 **a** with the $R(T)$ measured before structuring the crystal, we find that the ring maintains the same superconducting transition as the initial crystal (see Supplementary Figure 7.S1). We find no discernible changes in the overall transport properties of the material, as might have been introduced by microstructuring the crystal. A set of current-voltage ($I-V$) characteristics, taken at different temperatures, is shown in Figure 7.4 **b**. The critical current I_c develops around 1.7 K, and begins to saturate below 0.8 K. We find the hysteresis in $I-V$ around I_c to remain negligibly small, even at temperatures far below T_c.

7.3.2. INSIGHTS FROM ORDER PARAMETER SIMULATIONS

Before presenting the results of transport measurements in a magnetic field, we examine the expected chiral-domain configuration in our structure. This is accomplished by performing detailed time-dependent Ginzburg-Landau simulations, under the assumption of a chiral p-wave order parameter, for microrings with nanostructured transport leads (similar to the one used in our experiments). The simulations show that the ring can host single- or a multi-chiral domain states, depending on the parameters r_{in}/ξ and r_{out}/ξ, which correspond to the inner and outer radius of the ring, scaled by the (temperature-dependent) coherence length ξ.

In Figure 7.5 we present the key aspects of the simulations related to our particular structure. However, the complete phase diagram of various ground states was also

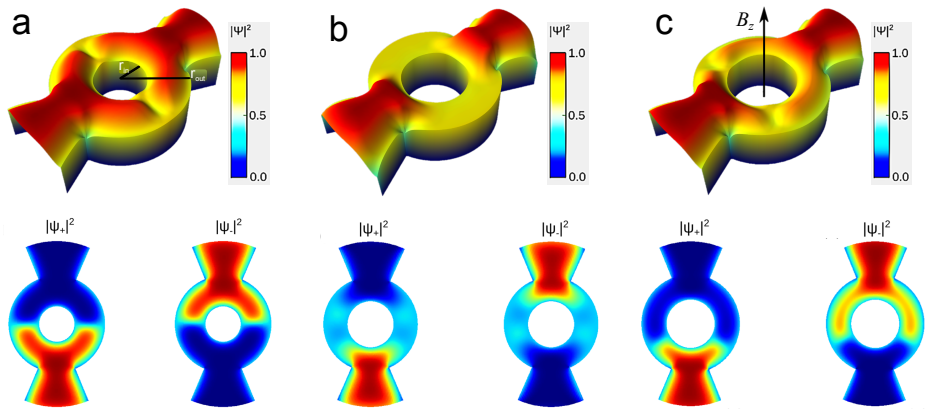

Figure 7.5: Ground state configurations of a chiral p-wave ring with nanostructured transport leads. The colourmap represents the Cooper pair density. The bottom panels shows the Cooper pair density for each chiral component separately. **a,b** simulated ground states in the absence of external fields, at temperatures $T \ll T_c$ and $T \approx T_c$, respectively. **a** corresponds to a state where the two chiral components are segregated by a single domain wall, while for **b** the chiral components are overlapping with each other, and are equally suppressed. **c** shows the behaviour of the chiral domain state in **a** under an applied out-of-plane magnetic field. In all three states the ring hosts a multi-domain configuration, where the suppression of the condensate results in the formation of a pair of parallel weak links, similar to a DC SQUID.

calculated as a function $(r_{in}/\xi, r_{out}/\xi)$. Figure 7.5**a** shows the simulated ground state of our ring for $T \ll T_c$, obtained by setting $r_{in}/\xi \approx 2.2$ and $r_{out}/\xi \approx 6.1$, while setting $\xi(T=0) \approx 66$ nm. This shows two distinct chiral domains, separated by a single ChDW in each arm of the ring. The ChDW extends over a length of the order of ξ. Within this region, the order parameter is reduced to about half of its amplitude in the banks, resulting in the formation of two parallel Josephson weak links.

The chiral states in the other temperature limit, where for $T \sim T_c$ is presented in Figure 7.5 **b**. This corresponds to a state where $\xi(T) \sim w$, where $w = r_{out} - r_{in}$. We see that the order parameter is suppressed over a significantly larger portion of the arms. While this may appear as an extended ChDW, it corresponds to a different state, which should be described as one of overlapping chiral domains. Intuitively, one can picture this as a mixed state, where the two chiral components are both present and equally suppressed over the entire ring. As they overlap with each other, their amplitudes are reduced to about a third of the original value in the transport leads. However, from the physics point of view, the suppression of $|\Psi|$ still produces a pair of stable weak links.

Figure 7.5 **c** shows the $T \ll T_c$ state in presence of a finite magnetic field applied along the ring axis ($\Phi = 2.4\Phi_0$). Pinned by the restricted dimensions, the ChDWs remain in the arms of the ring, though their positions are shifted away from the middle. This is because, depending on its direction, the applied field enlarges one chiral domain over the other. Nevertheless, the simulations show that a multi-domain state

with parallel weak links, formed by ChDWs, is stable in our ring while performing field-dependent measurements, to which we now turn.

7.3.3. CRITICAL CURRENT OSCILLATIONS

We examined the supercurrent interference properties of the ring by applying an out-of-plane magnetic field H_z. Figure 7.6 presents the I_c measured for positive I_c^+ and negative I_c^+ currents, at two different temperatures — representing $T \sim T_c$ and $T \ll T_c$ regimes. For both temperatures we observe distinct critical current oscillations, with the period corresponding to fluxoid quantization over the ring area. This distinct pattern strongly resembles that of the classical dc SQUID with two artificially prepared weak links. Figure 7.6 also shows $-I_c^-(-H)$ overlaid on its time-reversed counterpart $+I_c^+(+H)$ for comparison.

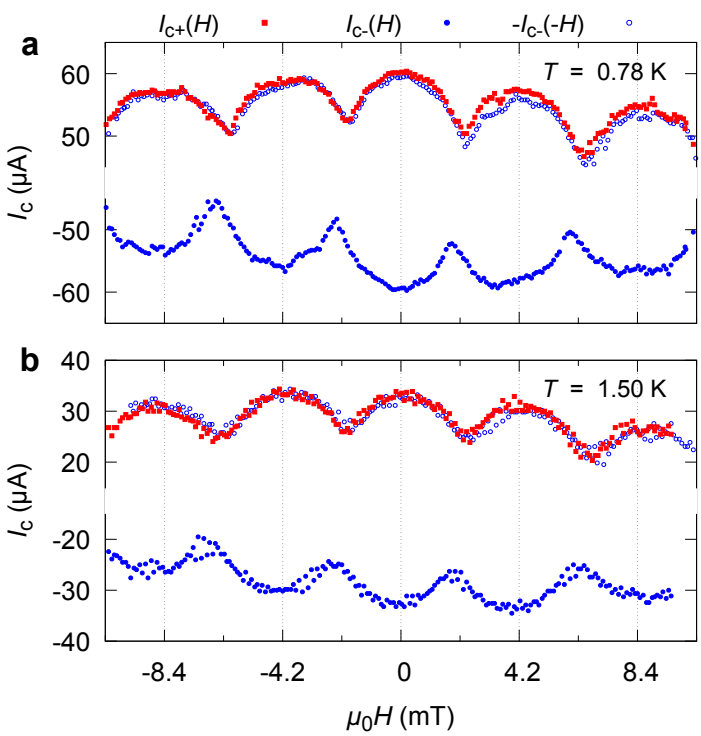

Figure 7.6: Critical current as a function of magnetic field for positive (I_c^+) and negative (I_c^-) d.c. bias measured at 0.78 K ($T = 0.45\ T_c$) **(a)**, and 1.5 K ($T = 0.85\ T_c$) **(b)**. $-I_c^-(-H)$ represents the time-reversed counterpart of $I_c^+(+H)$.

To demonstrate the robustness of the SQUID behaviour, in Figure 7.6 we plot the magnetoresistance signal, produced by the I_c oscillations over a wide range of tem-

peratures. These are measured by applying a constant d.c bias while sweeping the field. As the magnitude of $I_c(H_z)$ oscillates between $I_c < I$ and $I_c > I$, the system is driven out and back into the zero-voltage regime of the $I-V$ curve. This produces nonlinear variations in voltage, which we measure for $+I$ and $-I$ biases. We represent this as resistance, using the definition $R = [V(I) - V(-I)]/2I$.

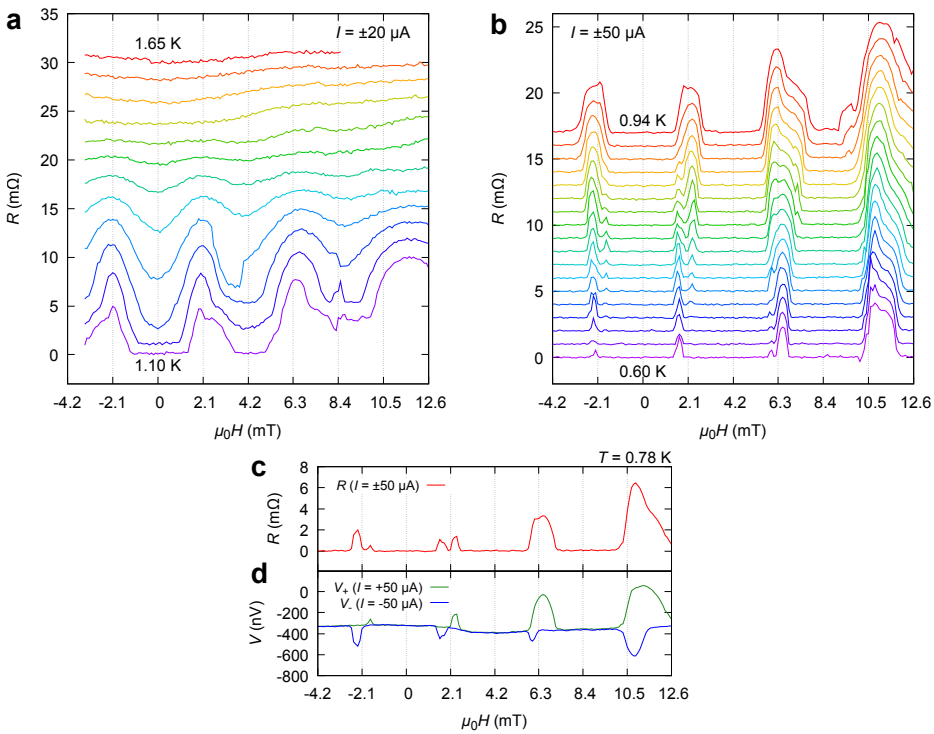

Figure 7.7: Magnetotransport over a wide range of temperatures. Non-linear variations in voltage, driven by (SQUID) I_c oscillations, result in a periodic large-amplitude magnetoresistance signal $R(H)$ (**a,b**) which appears with the onset of the transition, and continues to be present at temperatures far below T_c. The temperature steps are ≈ 50 mK, and the $R(H)$ traces are offset from each other for clarity. **c,d** show how the magnetovoltage from $I_\pm$ is converted to $R(H)$.

Figure 7.7**a,b** show the results collected over a broad range of temperatures. These reveal that the SQUID oscillations emerge together with I_c at the onset of the transition, and continue to be present for all $T < T_c$. In Figure 7.7**c** we account for the shape of $R(H)$, where in some cases the peaks can appear to be split or broadened. This is due to a slight difference in the values of $I_c^\pm$, which causes the peaks in $V(\pm I)$ to appear asymmetrically.

The magnetovoltage signal and field-dependent $I-V$ measurements are crucial for resolving an issue regarding previous reports of unconventional behaviour of Sr_2RuO_4 rings. Cai *et al.* have consistently observed magnetoresistance oscillations with unexpectedly large amplitude [21, 22]. Their reported magnetoresistance oscil-

lations are also stable over a wide range of temperatures, reaching far below T_c (see Figure 3a in Ref. [21]). As Figure 7.7 demonstrates however, if the magnetovoltage signal is divided by a constant dc bias, it produces the same type of magnetoresistance as the ones reported by Cai *et al.* . Hence, what appears as large-amplitude magnetoresistance is in fact the nonlinear variation of voltage, driven by an oscillating critical current.

7.3.4. RINGS WITH AN EXTRINSIC PHASE & T_C OSCILLATIONS

To verify that the observed behaviour is an inherent property of the intrinsic phase of Sr_2RuO_4, and a multicomponent order parameter, we examined a number of structures with a full or partial extrinsic phase. These are characterised by a noticeably broader transition, which begins near 3 K (see Figure 7.8**a**). We recently reported observations of Little-Parks (LP) oscillations in such structures [19], and here we show that those are of a completely different character than the I_c oscillations found in the a pure (bulk-like) intrinsic phase.

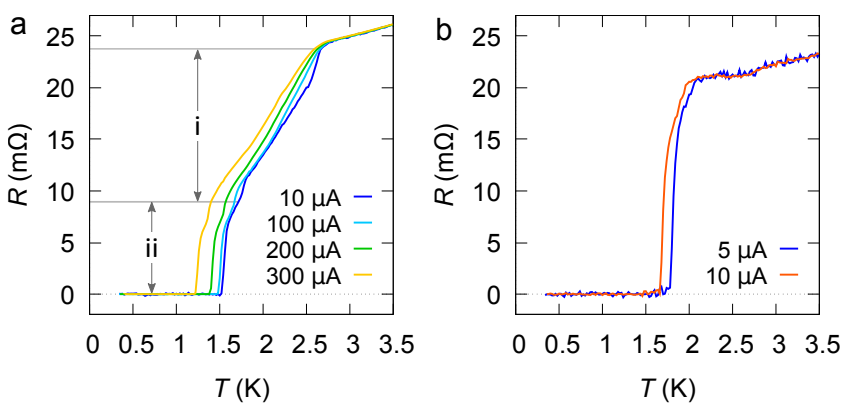

Figure 7.8: Comparing resistance transitions for the extrinsic & intrinsic phases of Sr_2RuO_4. **a** resistance transitions in sample yy150. The $R(T)$ curve is divided into two separate regimes. **i** corresponds to the superconducting transition in the loop itself, and also indicates the region where the Little-Parks oscillations are observed. **ii** shows the transition in the transport leads. The leads have a sharp transition around 1.5 K, which is associated with the intrinsic phase of Sr_2RuO_4. The ring itself however, exhibits a broad transition with an onset at 2.6 K. This is a clear characteristic of the extrinsic phase, which appears under uniaxial strain (e.g. see 7.1 **d**). **b** $R(T)$ measurements from sample yy146, shown here for comparison. The bulk-like transition corresponds to a structure with a homogenous intrinsic phase.

In particular, we compare the above data (taken from sample yy146) with those of a second ring called yy150. This ring was also fabricated from a bulk crystal with a T_c of 1.5 K. After structuring however, the ring was found to have an enhanced T_c, where the transition already starts at 2.6 K. As indicated in Figure 7.8**a**, the ring itself is predominantly in the extrinsic phase, which was most likely introduced by the fabrication process (probably due to a strain induced by FIB milling). Compared

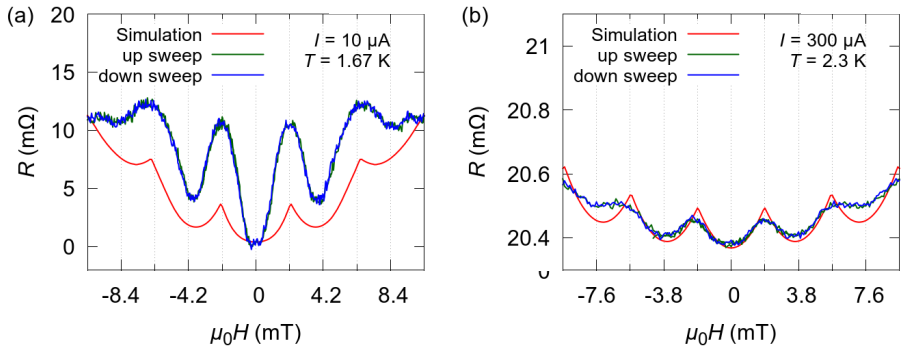

Figure 7.9: Simulated magnetoresistance for T_c oscillations. **(a)** sample yy146. The measurements signal is dominated by a large-amplitude magnetovoltage, driven by the (SQUID) I_c oscillations. **(b)** sample yy150. The absence of SQUID oscillations in a system with a dominant extrinsic phase allows us to observe the small-amplitude magnetoresistance signal produced by the Φ_0-periodic oscillations in T_c. The loop exhibits standard behaviour, and the oscillations can be modelled by the conventional Little-Parks effect.

to yy146 (RRR= 238), this ring has a smaller ratio of residual resistance RRR = 129. Nevertheless, the high RRR value still indicates strong and homogeneous metallicity.

In Figure 7.9, we show the $R(H_z)$ measurements for both rings, taken at temperatures within the resistive transition. In both rings we find fluxoid-periodic oscillations, which we compare with those simulated for the LP effect. This serves as a reference for the standard behaviour of a homogenous superconducting loop. The LP effect refers to the Φ_0-periodic suppression of T_c, which appears as a small magnetoresistance oscillation for measurements taken at the resistive transition of a superconducting loop [23]. The change of the transition temperature due to the LP oscillations is given by [24]:

$$\frac{T_c(B_z) - T_c(0)}{T_c(0)} = \left(\frac{\pi\xi(0)wB_z}{\sqrt{3}\Phi_0}\right)^2 - \frac{\xi^2(0)}{r_{in}r_{out}}\left(n - \frac{\pi r_{in}r_{out}B_z\pi}{\Phi_0}\right)^2 \tag{7.1}$$

where $\xi(0)$ is the coherence length at 0 K, n is an integer, r_{in} and r_{out} are the inner and outer radii of the ring, and $w = r_{out} - r_{in}$ is the width. The first term of Equation 7.1 represents the effect of the Meissner shielding, and the second term represents the effect of the fluxoid quantization. To convert the change of the transition temperature to the resistance variation, we assume that the $R(T)$ curve does not change its shape under magnetic field and shifts horizontally by$\Delta T_c = T_c(0) - T_c(B_z)$. The simulations in Figure 7.9 were obtained using $\xi(0) = 66$ nm as the coherence length of Sr_2RuO_4, and $2r_{in} = 0.55$ μm, $2r_{out} = 1.1$ μm for sample yy146, and $2r_{in} = 0.7$ μm, $2r_{out} = 1$ μm for yy150.

For sample yy150, both the period and the amplitude of the oscillations agree with

those of the simulation. It is therefore clear that the oscillations are the result of standard the LP effect, and are driven by T_c oscillations. In contrast, for sample yy146, the amplitude of the observed $R(H)$ oscillations is substantially larger than what T_c variations can produce. This is because the oscillations in yy146 are driven by $I_c(H)$. As shown in Figure 7.7, the I_c oscillations produce *non-linear* variations in voltage, which heavily dominate the signal resulting from T_c oscillations. Note that the LP oscillations correspond to a *linear* $I-V$ relation, whose slope gently attenuates by fluxoid quantization, resulting in a small variation of (ohmic) resistance.

The contrast in the behavior of the two systems can be demonstrated more directly by comparing their $I-V$ characteristics at low temperatures. These are presented in Figure 7.10 in the form of $I-V$ traces, and their first derivatives. Unlike sample yy146, the critical current oscillations are completely absent in yy150, the ring which showed standard LP oscillations. We found this behavior to be common for all the systems with a dominant extrinsic phase that were measured (see Supplementary Figure 7.S2). While these systems vary in shape and dimensions, they consistently showed standard T_c variations, which could only appear in the $R(H)$ measured at $T \approx T_c$, but no sign of SQUID oscillations at any temperature.

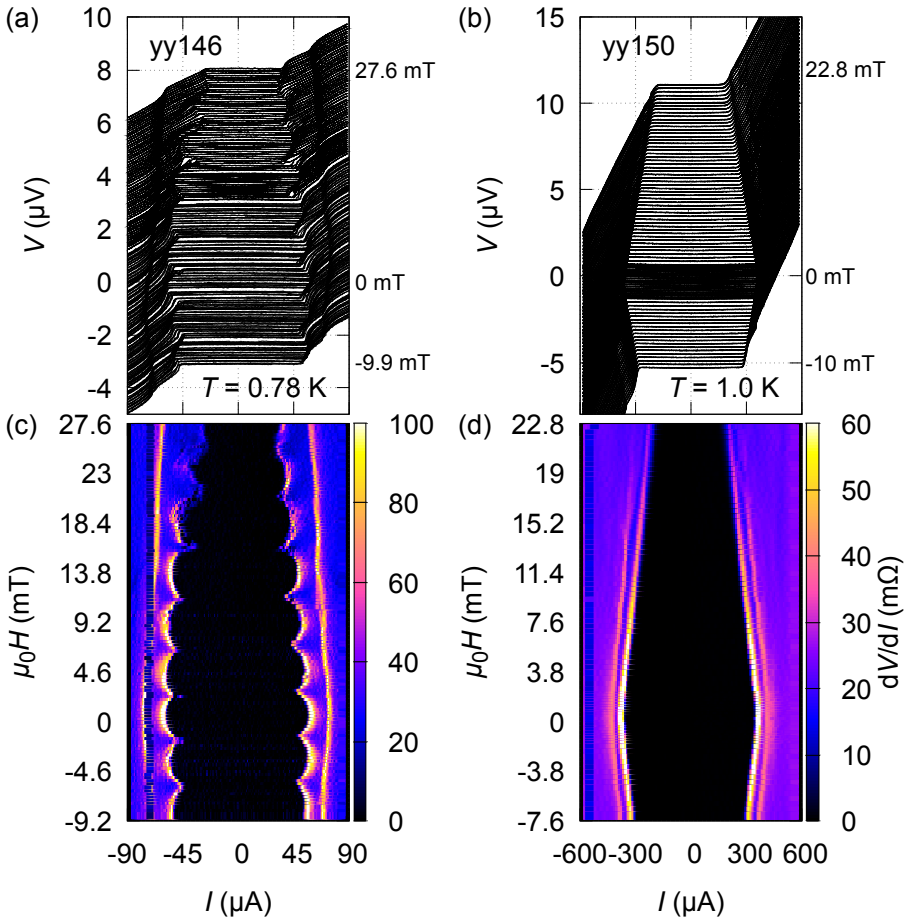

Figure 7.10: $I-V$ characteristics as a function of magnetic field: extrinsic vs. intrinsic phases. **a,b** $I-V$ traces measured while scanning $\mu_0 H_z$ in steps of 0.1 mT at $T \approx 0.45\ T_c$ for samples yy146 and yy150. **a** shows the SQUID oscillations of sample yy146, which represents the intrinsic phase of Sr_2RuO_4. **b** oscillations entirely absent in sample yy150, which has a predominantly extrinsic phase. **c,d** dV/dI plots obtained from the $I-V$ traces in **a,b**, demonstrating the contrast between the intrinsic and the extrinsic phase, corresponding to yy146 and yy150, respectively. **c** (**d**) shows the presence (absence) of the I_c oscillations in the intrinsic (extrinsic) phase found in yy146 (yy150).

7.3.5. ANOMALOUS CURRENT-VOLTAGE & IN-PLANE FIELDS

Figure 7.11**a** shows the anomalous $I-V$ characteristic of sample yy146, which occurs at 0.78 K for $\mu_0 H_z = 2$ mT, where we observe a clear asymmetry with respect to the applied current bias. While voltage variations show standard behaviour for positive bias, the $I-V$ traces split into two separate paths depending on the sweep direction of negative bias. This results in an unusual hysteresis, where the $-I(V = 0) \rightarrow -I(V \neq 0)$ transition occurs at smaller currents than it does when sweeping I as $-I(V \neq 0) \rightarrow -I(V = 0)$, which is a clear contradiction to the standard $I-V$ hysteresis. This unusual $I-V$ characteristic appears to be of a similar nature as the ones reported for the so-called φ-junction, where the Josephson energy has a bistable zero-voltage state with phases $+\varphi$ and $-\varphi$, where $0 < \varphi < \pi$ [25, 26]. A similar scenario can occur at the ChDW, depending on the relative configuration of the domains [17]. This is described in Section 7.4.2.

The unconventional $I-V$ characteristics can be enhanced by applying rather small in-plane fields ($H_{ab} < 3\% H_{c1}$). Figure 7.12 shows sets of $I-V$ traces taken while scanning the out-of-plane field. Prior to each set of measurement, the sample was cooled through T_c under a constant in-plane field in the x-direction. While the period and amplitude of the original $I_c(H_z)$ pattern (responsible for the SQUID behavior) remains mostly intact, the in-plane field introduces a series of unusual non-zero voltage states which occur at $I < I_c$. Unlike the previous reports of unconventional $I-V$ characteristics in (s-wave) superconductor-Sr_2RuO_4 hybrids (e.g. see Figure 7.1 **e**), the observed voltage anomalies are highly robust and stable. For a given combi-

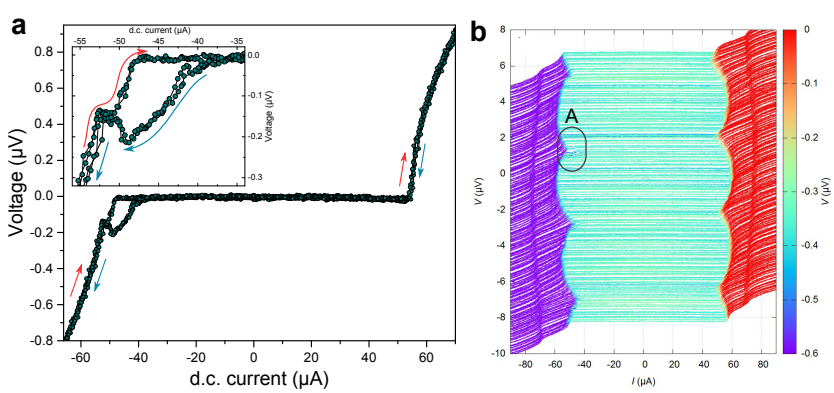

Figure 7.11: Anomalous $I-V$ characteristic in the absence of external in-plane fields. **a**, asymmetric step-like feature observed at $\mu_0 H_z = 2$ mT. Inset is the close up of the voltage transitions that occur at negative bias, with red and blue arrows indicating forward and reverse sweep directions of the applied current, respectively. The $I-V$ curve is measured by scanning I as $0 \rightarrow I^+ \rightarrow I^- \rightarrow I^+ \rightarrow I^-$ in two cycles. As shown here, the anomaly is highly stable and reproducible in repeated measurements. **b** shows individual $I-V$ curves taken over a wide range of out-of-plane fields, in steps of 0.1 mT. **A** indicates the region where the $I-V$ anomaly is observed.

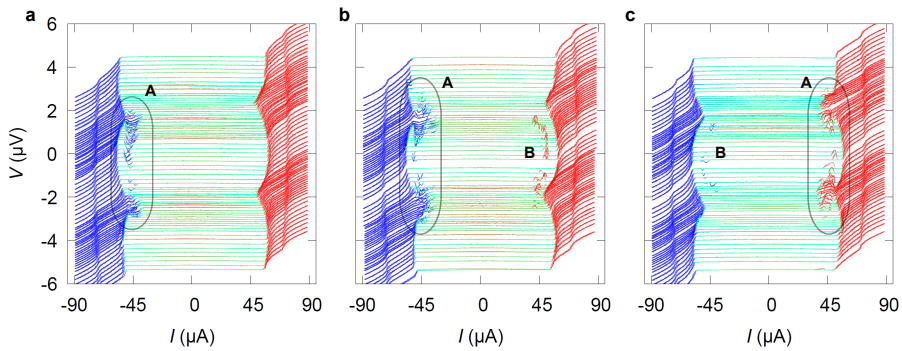

Figure 7.12: Anomalous $I-V$ characteristics & their relation with in-plane fields. Prior to each set of H_z scan, the sample is heated to its normal state and then cooled down to 0.78 K under a constant magnetic field, applied in x-direction. **a**, **b** and **c** correspond to field cooled measurements with $\mu_0 H_x = 0.5$ mT, 1 mT and -1 mT, respectively. The $I-V$ anomalies appear in two different forms, which are labelled as **A** and **B**. **A** appears at $I \approx I_c$, and is more pronounced near the minima of the interference pattern. **B** takes place on the opposite side of the $I-V$ curve, where there are no features near the $I_c(H_z)$ minima. These are isolated non-zero voltage peaks, which appear deep within the zero-voltage regime $I < I_c$. The anomalies show a direct relation with the sign and amplitude of H_x. As shown in **c**, switching the polarity of H_x reverses the order in which **A** and **B** appear.

nation of H_x and H_z, the same $I-V$ trace could be reproduced in multiple cooling cycles, with no discernable changes in the size or position of the voltage anomalies.

The anomalies also exhibit a direct relation with the sign and amplitude of the external in-plane field. For instance, at $\mu_0 H_x = 0, 0.5$ mT and 1 mT (Figures 7.11**b** & 7.12 **a,b**) the distortion of $I-V$ is highest near the I_c minima for $I < 0$ (labelled as **A**), while the anomalies remain minimal for I^+ (labelled as **B**). Remarkably, we find this asymmetric trend to be fully reversible by switching the sign of the in-plane field, as shown in Figure 7.11 for $\mu_0 H_x = -1$ mT.

The asymmetric interference patterns also indicate the breaking of time-reversal symmetry (TRS), as the condition $I_c^+(+H_z) = I_c^-(-H_z)$ is violated. We attribute this to the asymmetric orientation of the domains, which could induce an arbitrary phase difference across the ChDW. As for the role of in-plane fields, there are a number of possibilities related to spin polarization. These are discussed in Section 7.4.2.

7.4. DISCUSSION

7.4.1. MECHANISMS FOR OSCILLATORY $I_C(H)$

Before adopting ChDWs as the origin of the observed I_c oscillations, we consider other known mechanisms for such oscillations. In a homogenous loop, I_c can be modulated by the circulating persistent current I_p, which varies linearly with flux, and switches its direction every $\Phi_0/2$. This mostly results in a sawtooth-like modulation of I_c [27], which cannot account for the non-linear form of the patterns shown in Figure 7.6. Furthermore, the magnitude of I_p is inversely proportional to the kinetic inductance L_k, which depends on the penetration depth $L_k \propto \lambda^2(T)$. If the oscillations were driven by circulating currents, the amplitude of ΔI_c would grow larger by lowering the temperature, since $\Delta I_c \propto I_p \propto 1/\lambda^2(T)$ [27]. In contrast, Figure 7.6 shows that $\Delta I_c \approx 12\mu$A for both temperatures.

As we noted above, the large magnetoresistance found by Cai *et al.* in their Sr_2RuO_4 rings is also a form of I_c oscillation, which they attributed to current-excited vortices moving across the ring [21, 22]. Vortex motion can indeed result in magnetoresistance oscillations with considerably larger amplitude. However, as demonstrated by Berdiyorov *et al.* [28], the large-amplitude oscillations only occur over a finite temperature range. While increasing the measurement current could shift the oscillations to lower temperatures than Little-Parks, the range for large-amplitude oscillations remains relatively narrow, usually no more than 5% below T_c (e.g. see Figure 5b of Ref. [28] and Figure 2 of Ref. [29]). In contrast, the Sr_2RuO_4 rings with the intrinsic 1.5 K phase (including the ones reported by Cai *et al.*) consistently yield a large magnetoresistance signal for all $T < T_c$ (see Figure 7.7 and Figure 3a in Ref. [21]).

The observed I_c oscillations can be understood in terms of the quantum interference of macroscopic wavefunctions. With the exception of homogenous loops whose dimensions are smaller than $\xi(T)$ [30] (i.e. not applicable here since $r \lessapprox 4\xi(T)$ at $T =$ 0.78 K, such interference would require a pair of parallel Josephson junctions. These correspond to well-defined weak links where (at least) two macroscopic wavefunctions can overlap, and yield a *single-valued* current-phase relation (CPR). Weak links can be intrinsic to the material (e.g. cuprates, grain boundaries) or artificially prepared (e.g. bridges, proximity effect in SNS and SIS junctions). In either case, the suppression of the order parameter must be stable enough to produce a single-valued CPR [31]. We also note that the junctions responsible for the observed SQUID behaviour must be rather symmetric with respect to each other, since asymmetric I_c values could not produce the distinct cusp-shaped minima of the interference patterns in Figure 7.6.

Geometrical constrictions (e.g. bridges and nanowires) are known to serve as Josephson junctions, if their dimensions are comparable to ξ. It is well established that the

CPR of such Junctions is defined by the ratio of $\xi(T)$ to the length of the weak link, L. Since $\xi(T)$ varies with temperature, while L remains fixed, the CPR of such weak links is known to be strongly temperature dependent. Generally, lowering the temperature from T_c is known to transform a sinusoidal CPR into a sawtooth-like curve, which ultimately turns into multivalued relations for $L \gtrsim 3.5\xi(T)$ (corresponding to the nucleation of phase-slip centres) [31–33]. The multivalued CPR manifests itself as a hysteretic $I-V$ relation, which is a highly common characteristic of constriction junctions at $T \ll T_c$ [34, 35]. This is in direct contrast to the $I-V$ measurements presented in Figure 7.4 **b**, which show negligible hysteresis for temperatures as low as 0.2 T_c, where $L \gtrsim \xi(T)$. Furthermore, the patterns taken at $T = 0.45\ T_c$ and 0.85 T_c (Figure 7.6 **a** & **b**) have the same overall shape; which indicates that they most likely correspond to the same CPR. Whereas for constriction junctions, the oscillations would have been heavily deformed by the pronounced difference in $\xi(T)/L$. In case of ChDWs however, the size of the junction is determined by the coherence length (see Figure 7.2). This means that, instead of having a fixed value, L has a similar temperature dependence as $\xi(T)$. Therefore, compared to constriction junctions, the $\xi(T)/L$ ratio of a ChDW remains unaffected by lowering the temperature. This accounts for the lack of hysteresis in the $I-V$ (Figure 7.4 **b**), and the unperturbed shape of the interference patterns in Figure7.6.

In certain cases, phase-slip lines are also known to act as effective weak links. In a homogenous loop, fast moving kinematic vortices crossing the arms can dynamically form a pair of effective weak links, and operate as a SQUID. This mechanism however is highly temperature sensitive. As demonstrated in Refs. [36, 37], phase slippage can only yield a SQUID behaviour for a strictly narrow temperature range near T_c. Hence, it cannot account for the Sr_2RuO_4 rings, where the I_c oscillations remain unchanged for all $T < T_c$.

Lastly, we exclude the possibility of forming accidental proximity junctions by Ru inclusions, or any other normal metal. Apart from their apparent absence in the SEM images obtained while structuring the crystal, inclusions would have induced an extrinsic 3K-phase, which is absent in our ring and the ones measured by Cai *et al.* [21, 22]. Furthermore, the relative suppression of the superconducting gap in a normal metal weak link would cause it to have a lower T_c than the superconducting electrodes. This should appear as (at least) two distinct transitions in $R(T)$ measurements: one for the electrodes; and one for the proximized material in the weak link, which clearly is not the case here — as shown in Figure 7.4 **a** and Refs. [21, 22]. Tunnel junctions, which in some cases can form by grain boundaries or nanocracks, are also not applicable here. This is evident by the strong metallicity of the rings, and the exceptionally high values of RRR (Figure 7.4 **a**), which could not be produced in the presence of insulating barriers.

7.4.2. JOSEPHSON ENERGY OF A CHIRAL DOMAIN WALL

In this section we use the model developed by Sigrist and Agterberg (1999) [17] to describe the Josephson energy of ChDW as function of its orientation. The energy profile hosts stable and metastable states, whose phases are determined by the orientation of ChDW, and can take on *any* values between 0 and π. We consider how these states would appear in a sequence of bias current sweeps, and compare the expected outcome with our own $I-V$ measurements.

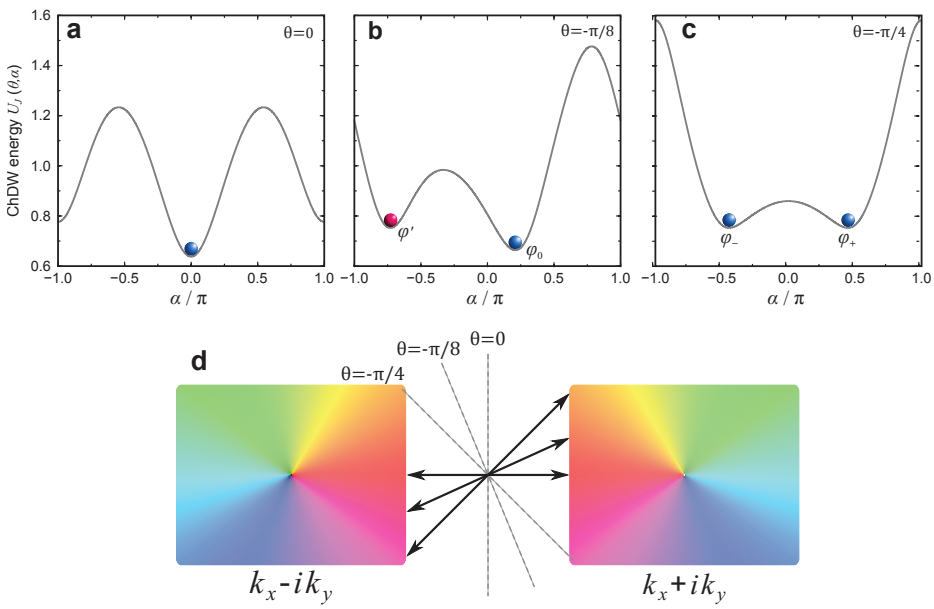

Figure 7.13: **Josephson energy of the chiral domain wall**. **a-c**, energy profiles of a chiral domain wall (ChDW) at various orientations relative to transport direction (θ). α is the phase difference between the two sides of the junction. **a**, $\theta = 0$, the junction has a stable phase at $\alpha = 0$ and a metastable phase at $\alpha = \pi$. **b**, $\theta = -\pi/8$. Compared to $\theta = 0$, the stable state (blue) has a higher energy, while the energy of the metastable state (red) is lowered. The junction has developed arbitrary phases φ_0 (stable) and φ' (metastable). **c**, as $\theta \to -\pi/4$ the two minima continue to approach in energy, and form a degenerate ground state at $\theta = -\pi/4$, with a Josephson phase $\pm\varphi$. All energy profiles correspond to zero bias current. The $U_j(\theta,\alpha)$ plots are adopted from Ref. [17]. **d**, phase variation across a ChDW. Two chiral domains (coloured boxes) are separated by a ChDW (the blank space in between) with an arbitrary orientation. Colours indicates the orbital phaseof the order parameter, which winds in a different direction for each domain. ChDW orientation is represented by the direction of the transport channel that connects the two domains (solid arrows). θ is defined as the angle between the ChDW plane and the normal to the transport direction (dashed line). If $\theta = 0$, the arrow connects the left and right domains via the same phase (red on both sides). As $\theta : 0 \to -\pi/4$, the orbital phase of the left domain is no longer equal to that of the right domain, giving rise to an arbitrary Josephson phase.

Sigrist *et al.* showed that, in addition to the usual phase difference between two sides of the weak link α, the Josephson energy of a ChDW would also be a function of the relative alignment of the two domains with respect to the direction of transport. This concept is illustrated in Figure 7.13, where θ represents the angle between transport

direction (represented by arrows in Figure 7.13 **d**) and the normal to the plane of ChDW. When the bias current is perpendicular to the ChDW ($\theta = 0$), $U_J(\alpha, 0)$ has one stable ground state at $\alpha = 0$, and one metastable state at $\alpha = \pi$. In this case the ChDW operates as a 0-junction, meaning that — in the absence of external flux — there is zero phase difference between the left and the right side of the junction. However, as we see in Figure 7.13 **b,c**, the two states change their energies depending on the orientation of ChDW.

Figure 7.13 **b** shows the energy of a system where the transport direction makes a $\theta = -\pi/8$ angle with the normal to the ChDW plane. This raises the energy of the stable state (previously at $\alpha = 0$), and lowers the energy of the metastable state. More striking however, is that the ground state has developed an arbitrary phase of φ_0, which is neither zero or π. The offset in the phase of the ground state has profound consequences on the physics governing the junction, as it means that there would be a finite flow of supercurrent in the *absence* of external bias or magnetic flux. This anomalous current breaks the symmetry between leftward and rightward transport across the junction, which is referred to as the chiral symmetry (not to be confused with the chirality of the order parameter). In this sense, a ChDW acts as the so-called φ_0-junction, whose energy profile has a single ground state with a phase offset of φ_0. The main difference here being the presence of an additional metastable state φ'.

As $\theta \to -\pi/4$, the two states of $U_J(\alpha, \theta)$ continue to approach in energy, and ultimately form a degenerate ground state at $\theta = -\pi/4$ (see Figure 7.13 **c**). This energy profile corresponds to that of the so-called φ-junction, which has a bistable zero-voltage state with phases $\alpha = \pm\varphi$. This has been realised in junctions with parallel 0 and π segments, which have been carefully tuned to yield a spatially averaged phase that is neither 0 nor π [25, 26]. A unique characteristic of the ϕ-junction is that the $I - V$ can exhibit two critical currents. In Ref. [26] the authors show that their junction can be prepared in either one of $+\varphi$ or $-\varphi$ states. Depending on the current sweep sequence, there would be a step on one side of the $I - V$ trace, corresponding to the transition from $\pm\varphi$ phase to $\mp\varphi$. For instance, if the system is in the $+\varphi$ state, sweeping the current with a positive bias would result in a single I_c^+ as the phase escapes $+\varphi$ (i.e. in Figure 7.13 **c**, the ball in $+\varphi$ begins to roll down the right side of the "washboard potential"). Now consider what happens when we bring the applied bias back to zero, and continue to sweep the current in the negative direction. As $I^+ \to 0$, the phase gets initially re-trapped in the $+\varphi$ minimum, which it escapes as we continue sweeping $I : 0 \to I^-$ (i.e. tilting the energy profile to the left) but gets trapped again by the $-\varphi$ minimum before it enters the dynamic regime (i.e. rolling down the left side of the washboard potential). This results in two zero-voltage states: first by retrapping at $+\varphi$, and then by the energy well at $-\varphi$. The second zero-voltage state manifests itself as a step in the $I - V$, which appears on the left-hand side of the trace (negative bias). If we now reverse this sequence by sweeping the bias as $I^- \to I^+$, the

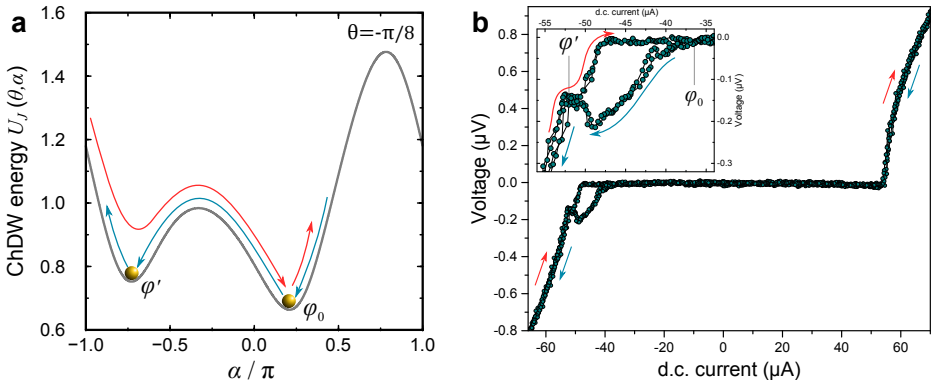

Figure 7.14: $I-V$ behaviour of a ChDW junction with an arbitrary orientation. **a**, Josephson energy of the ChDW for $\theta = -\pi/8$, in the absence of bias current $I = 0$ (adopted from Ref. [17]). Red and blue arrows represent forward reverse sweeps of bias current, respectively. In the absence of bias current, the phase is trapped at φ_0. Sweeping the current as $I : 0 \to I^+$ would result in a single I_c as the phase escapes φ_0 ($V \neq 0$). In the reverse sweep $I^+ \to 0$, the phase is retrapped at φ_0. Sweeping with a negative bias current would tip the energy profile to the left. The phase leaves the φ_0 minimum, but is subsequently trapped by the local minimum at φ', where it remains before entering the dynamic regime ($V \neq 0$). As we sweep the current back to zero, the phase is momentarily retrapped by the local minimum at φ', before making its way to the global minimum at φ_0. We used $\theta = -\pi/8$ to represent the $I-V$ characteristics of the entire class of $0 < |\theta| < \pi/4$. The magnitude of critical and retrapping currents would depend on the depth of the minima and the exact value of θ. However, φ_0 and φ' ensure that there will be multiple static regimes in the $I-V$ curve, and that they will not be symmetric with respect to the sign of I. **b**, $V(I)$ measured at $\mu_0 H_z = 2$ mT ($H_{ab} = 0$) by scanning I as $I^+ \to I^- \to I^+$ in multiple cycles. The same convention as **a** is used to indicate the sweep direction. By reasoning that if $\Delta V/\Delta I = 0$ (static phase), the phase must be trapped by a minimum of energy (either local or global), it is easy to see how this unusual $I-V$ can arise from an energy profile similar to the one depicted in **a**.

step would appear on the right-hand side of the $I-V$ (assuming damping is not too small). A clear example of such $I-V$ behaviour can be found in Ref. [25] (Fig. 4).

In order to have multiple zero-voltage states, there needs to be multiple minima in the energy profile of the junction. For instance, the asymmetric $I-V$ characteristic of the φ-junction does not apply to φ_0 junctions, where the Josephson energy has a single minimum. This brings us back to Figure 7.13 **b**, which represents the most general configuration of a ChDW, as it includes all orientations within $0 < |\theta| < \pi/4$ (as opposed to 7.13 **a,c**, which correspond to special angles $\theta = 0, \pm\pi/4$). For convenience however, we continue to use the example of $\theta = -\pi/8$ in the following discussion. What makes this type of $U_J(\alpha,\theta)$ so intriguing is that it contains elements of both φ_0- and φ-junctions. It is similar to the φ_0-junction, in a sense that there is only one ground state — with an arbitrary phase offset, but it also resembles the double-well energy profile of the φ-junction – due to its metastable state at φ'. As φ_0 and φ' states are not degenerate, it raises the question how the $I-V$ behaviour would be affected by this asymmetric energy profile.

In Figure 7.14 **a** we consider the same current sweep sequence as we did when describing the φ-junction above. Initially the system is in its ground state φ_0. Applying

a positive current bias (red arrow) would tilt the energy profile to the right, and produce a single I_c^+.[2] As we reverse the current back to zero (blue arrow) the phase is re-trapped at φ_0. This brings the junction back to its static regime, resulting in zero voltage. We then sweep the current with a negative bias (i.e. tilting the energy profile to the left), and the phase crosses-over from φ_0 to φ'. Once at φ', the phase remains static ($V = 0$) up to I_c^-.

So far the Josephson energy profile in Figure 7.14 **a** has produced the same $I - V$ characteristics as a φ-junction with a doubly degenerate ground state. There is a single critical current on one side of the $I - V$ (where the phase escapes φ_0), and two on the other side (one for $\varphi_0 \to \varphi'$, and another one when it leaves φ'). The distinction however becomes clear when we sweep the negative bias back to zero. In contrast to the φ-junction, the asymmetric structure of $U_J(\alpha,\theta)$ guarantees the φ_0 state to have a lower energy every time the bias is removed. Hence, depending on the energy difference between φ' and φ_0, which in turn depends on θ, the two critical currents would consistently appear one side of the $I - V$ (as opposed to the φ-junction, where they can switch to either side). For $-\pi/4 < \theta < 0$, this would be the left-hand side of the $I - V$ (negative bias), and for $0 < \theta < \pi/4$, the step would appear on the right-hand side, since $U_J(+\alpha, -\theta) = U_J(-\alpha, +\theta)$.

As Figures 7.14 **b** and 7.12 show, the $0 < |\theta| < \pi/4$ scenario provides a rather apt description of the observed $I - V$ anomalies. We now continue by examining how $\theta \neq 0$ can occur in our structure. First, we make a note that the $I - V$ anomalies only appear at low temperatures, where a single ChDW is expected to be crossing the arms of the ring, as shown in Figure 7.5 **a & c**. In this regime $T \ll T_c$, the ChDWs are small enough to have a well-defined position and orientation with respect to the ring, and each other. In contrast, for $T \approx T_c$, overlapping chiral domains cover the entire ring (Figure 7.5 **b**) with no specific alignment, which makes this picture consistent with the absence of $I - V$ anomalies at $T = 1.5$ K.

Time-dependent Ginzburg-Landau simulations show that, when subjected to a d.c. current bias, a ChDW tends to orient itself along the direction of the applied current [18]. In our experiments, the anomalies emerge from the minima of the $I_c(H_z)$ pattern (Figure 7.12), where the circulating current in the ring is at its maximum. As the circulating current is added to the measurement current in one arm, and subtracted from the other, it creates an imbalance in the currents experienced by the ChDW. At $\Phi \sim \Phi_0/2$ the difference in currents could be sufficient to have a finite impact on the orientation of the ChDW.

The applied field H_z could also be playing a role by changing the position of the ChDW in each arm, as shown in Figure 7.5 **c**. While this may not directly affect θ

[2] Note that the asymmetric profile in Figure 7.14 **a** corresponds to the zero bias state i.e. $U_J(\alpha, \theta = -\pi/8)$ is not "tilted" by some external bias. The role of bias currents is shown in the form of red and blue arrows, which the phase can follow.

(i.e. orientation with respect to transport direction), H_z can modify the orientation of ChDWs relative to each other. This situation is discussed in Ref. [38], which considers a ring with a pair of ChDWs radially crossing its wall. Modelling the arbitrary angle between the ChDWs as the bending of a single ChDW, the authors argue that such a system can host fractional vortices, including the half-quantum vortex (HQV) at $\Phi \approx n\,\Phi_0/2$. It is worth noting that this HQV is different from the one discussed in Chapter 6, which could exist even in the absence of ChDWs. The entire phase winding of this HQV is carried out by the orbital component of the chiral states. As there is no winding of spin phase, this type of HQV is not accompanied with a spin-polarization, which means that it can be stable even in the absence of external fields H_{ab}.

Lastly, we discuss the role of in-plane fields H_{ab} in our experiment. As shown in Figure 7.12 the $I-V$ anomalies show a direct dependence on the sign and magnitude of H_x. The anomalies grow larger with the field and, more importantly, their symmetry is determined by the direction of H_x. Figure 7.12 **c** ($\mu_0 H_{ab} = -1$ mT) shows the $I-V$ pattern can be mirrored by switching the field polarity. As described above, if a ChDW is oriented at θ, where $-\pi/4 < \theta < 0$, the step in the $I-V$ would occur for the negative current bias. This however would be reversed if the ChDW was to change its orientation as $-\theta \to \theta$, in which case the energy profile would be mirrored in the phase space i.e. $U_J(+\alpha, -\theta) = U_J(-\alpha, +\theta)$. For instance, if $\theta : -\pi/8 \to \pi/8$, the φ' phase in Figure 7.14 **a** would become the ground state, and φ_0 would be metastable.

While one could argue that the applied H_x may have modified the orientation of the ChDW, a coupling between H_{ab} and the chiral components would be rather unlikely [3]. There is however a distinct possibility for H_{ab} to couple to the spin of Cooper pairs. Spin-susceptibility experiments on Sr_2RuO_4 have demonstrated that an external H_{ab} would introduce an imbalance between $|\uparrow\uparrow\rangle$ and $|\downarrow\downarrow\rangle$ states, which results in a finite spin polarization [39, 40] [4].

The spin polarization can play a role in our experiments in a number of ways. Here, we mention two. The first one is concerned with stabilizing half-quantum vortices (HQVs) through Zeeman coupling – as described in Chapter 6. This is consistent with the fact that the $I-V$ anomalies emerge at $\Phi \approx \Phi_0/2$, and that they grow larger with H_x, as the field should lower the energy of the HQV states. This however does not account for the observed asymmetry of the anomalies. Also, the in-plane fields used here are at least an order of magnitude smaller than the ones used in previous reports on HQV (in both Ref. [41] and Ref. [19] the signatures of HQV appear for $H_{ab} > 8$ mT).

A more reasonable explanation is that H_{ab} modifies the Josephson energy of the

[3] In order to change the domain configuration, a magnetic field would need to couple to the orbital angular momenta of the domains, which are expected to lie along the c-axis of Sr_2RuO_4 lattice.

[4] Note that the spin-susceptibility measurements needed to apply H_{ab} fields that were 2 to 3 orders of magnitude larger than the fields used in our experiments.

ChDW by introducing a non-zero spin current. The energy profiles in Figure 7.13 were formulated for a system with no spins [17]. There is however no reason to assume these profiles would remain unchanged in presence of a finite magnetization. For instance, the magnetization induced by H_{ab} could potentially lower the energy of φ' relative to φ_0, and vice versa. However, there are currently no theoretical studies on the energy of a ChDW as a function of spin polarization. Such information could be rather valuable.

SUMMARY OF THE ANOMALOUS CURRENT-VOLTAGE BEHAVIOUR

To summarise, the current-voltage measurements show multiple zero-voltage states, which requires the Josephson energy profile U_J to have more than one minimum. The additional zero-voltage state, which appears as a step in the $I-V$ measurements, has a distinct asymmetry with respect to the *sign* of the bias current. Regardless of sweep direction for I, the step constantly appears on the same side of the $I-V$ (in the absence of H_{ab}). This exotic behaviour is accounted for by an asymmetric Josephson energy which has one global and one local minimum, corresponding to a stable φ_0 and a metastable φ' Josephson phase, respectively, where φ_0 and φ' can take on any values between 0 and π. While most unconventional for usual Josephson junctions, this is a strikingly apt description of the predicted ChDW energy [17], particularly if the ChDW plane is not precisely perpendicular to the transport direction. TDGL simulations of our ring, show this condition could be realised at $T \ll T_c$, where the ChDW is small enough to develop a well-defined orientation (as opposed to $T \approx T_c$, where overlapping chiral domains extend over the entire ring), as shown in Figure 7.5. This is also consistent with our measurements, where the $I-V$ anomalies appear at 0.78 K, but are absent at 1.5 K. As for the cause of ChDW misalignment, we discuss a number of possibilities, the most likely of which being the circulating currents.

The $I-V$ anomalies show a direct dependence on small in-plane fields. They grow larger with H_x amplitude, and their asymmetric form is mirrored (with respect to I) by switching the direction of H_x. We attribute this to field-induced spin-polarization of equal-spin triplet Cooper pairs. We expect this finite magnetization to modify the symmetry of the Josephson energy profile. Currently, we lack the theoretical framework that can describe transport across a spin-polarized ChDW. Regardless of this, the reversible nature of $I-V$ anomalies makes it very clear that the effect is not stochastic, and corresponds to a robust mechanism which is yet to be understood. Fortunately, with the use of order parameter simulations and controllable mesoscopic structures, there is a real possibility of this in the near future.

Lastly, we note that due to the absence of external components in our system (s-wave electrodes, Ru inclusions, 3 K-phase, etc.), the $I-V$ anomalies – and the breaking of time-reversal symmetry which they represent – could only correspond to the intrinsic order parameter of Sr_2RuO_4.

7.5. SUMMARY & OUTLOOK

The existence of a p-wave chiral order parameter in Sr_2RuO_4 would make this a rare exception to currently known superconductors. Establishing this requires irrefutable evidence of *chirality*, which is expected to reveal itself in the form of superconducting chiral domains with spontaneous edge currents. The search for chiral domains however, has proven to be a challenging endeavour. The present study implements a new approach to this by focusing on the properties of a *single* chiral domain wall (ChDW) in a mesoscopic crystal.

It has been proposed that by locally suppressing the order parameter, a ChDW would act as an unconventional Josephson junction. We investigate this by performing transport experiments on mesoscopic rings, structured entirely out of a single (and homogenous) Sr_2RuO_4 crystal. Order parameter simulations predict this system to a have multi-domain ground state, with a ChDW crossing the arms of the ring, where it forms a pair of parallel Josephson junctions.

Our transport measurements show a clear I_c oscillation, similar to that of a DC SQUID with two symmetric Josephson junctions. The oscillations emerge together with the superconducting transition, and are continuously present in all the measurements down to $T \ll T_c$. We evaluate this behaviour in the terms of conventional types of weak link (e.g. nano-bridges, phase-slip lines, proximity junctions etc.). Each case shows clear discrepancies, and fails to describe our observations. Furthermore, the SQUID oscillations are entirely absent in structures with a finite level of disorder or strain, indicated by the enhancement of $T_c \rightarrow 3$ K (i.e. the "extrinsic" phase of Sr_2RuO_4). These systems behave as standard superconducting loops, showing only T_c oscillations which appear in the form of small-amplitude magnetoresistance near T_c.

In addition to the abovementioned SQUID oscillations, we also observe anomalous current-voltage characteristics, which also represent the breaking of time reversal symmetry. More specifically, repeated current sweep measurements show two distinct critical currents that only appear on one side of the $I-V$ curve. Qualitatively, this striking behaviour can be described by the unusual energy profile of a ChDW, which is predicted to have two minima of different energies. This leads to one stable and one metastable phase for the junction, which would appear as a multistage $I-V$ when sweeping the bias current.

Together, these results make a compelling case for the presence of Chiral domains in the intrinsic state of superconducting Sr_2RuO_4. Combining order parameter simulations with mesoscopic structures also sets a milestone for the study and implementation of superconducting domains, allowing for detailed design and understanding of a system before the actual fabrication.

7.6. SUPPLEMENTARY FIGURES

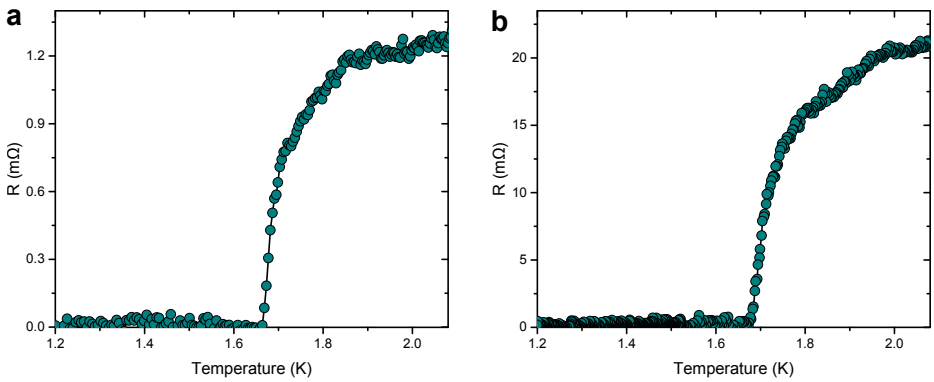

Figure 7.S1: **Superconducting transition of yy146: bulk crystal vs. structured microring**. Resistance as a function of temperature, measured before **a** and after **b** structuring with Ga^+ focused ion beam. The bulk crystal (**a**) and the ring (**b**) are measured using bias currents of 100 μA and 10 μA.

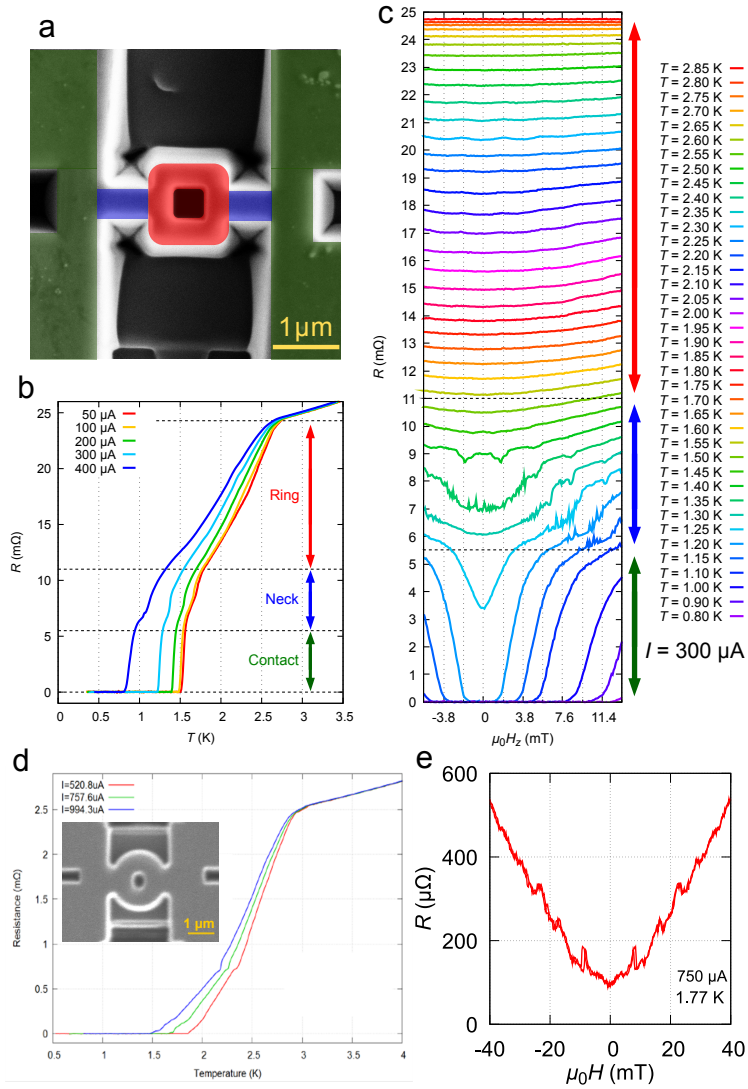

Figure 7.S2: **Rings with enhanced T_c.** Examples of rings where a finite level of disorder (i.e. stain) leads to the emergence of the "extrinsic" superconducting state in Sr_2RuO_4, characterised by the enhancement of $T_c \rightarrow 3\ K$. **a-c**, summary of transport properties of yy150 (discussed in the main text). **a**, False-colour scanning electron microscope image of the ring. This is an example of an inhomogeneous system, where the superconducting transition varies for different parts of the structure. This results in a multistage transition, which can be observed in the $R(T)$ measurements (**b**). The ring itself (red) corresponds to a broad transition with the onset at ≈ 3 K, which corresponds to the extrinsic phase of Sr_2RuO_4. In the bulk-like contacts (green), where disorder is minimal, we see a sharp transition near 1.5 K. **c**, magnetoresistance measurements at different temperatures. Little-Parks oscillations (discussed in the main text) appear in the first regime (red arrow), while the ring is still in the resistive state. SQUID oscillations are entirely absent at all temperatures. Other values of bias current (not shown here) produced the same effect. **d,e** transport measurements from yy147 (not in the main text). The crystal was not protected by the 100 nm SiO_x layer. As a result, the extrinsic phase emerges over the entire system, as indicated by the broad transition that begins at 3 K (**d**). No SQUID oscillations were found, only small amplitude magnetoresistance, driven by T_c variations (**e**).

REFERENCES

[1] A. P. Mackenzie and Y. Maeno. The superconductivity of Sr_2RuO_4 and the physics of spin-triplet pairing. *Reviews of Modern Physics*, 75(2):657, 2003.

[2] Y. Maeno, S. Kittaka, T. Nomura, S. Yonezawa, and K. Ishida. Evaluation of spin-triplet superconductivity in Sr_2RuO_4. *Journal of the Physical Society of Japan*, 81(1):011009, 2011.

[3] T. Rice and M. Sigrist. Sr_2RuO_4: an electronic analogue of ^{3}He ? *Journal of Physics: Condensed Matter*, 7(47):L643, 1995.

[4] G. M. Luke, Y. Fudamoto, K. Kojima, M. Larkin, J. Merrin, B. Nachumi, Y. Uemura, Y. Maeno, Z. Mao, Y. Mori, et al. Time-reversal symmetry-breaking superconductivity in Sr_2RuO_4. *Nature*, 394(6693):558, 1998.

[5] J. Xia, Y. Maeno, P. T. Beyersdorf, M. Fejer, and A. Kapitulnik. High resolution polar kerr effect measurements of Sr_2RuO_4: evidence for broken time-reversal symmetry in the superconducting state. *Physical Review Letters*, 97(16):167002, 2006.

[6] D. A. Ivanov. Non-Abelian statistics of half-quantum vortices in p-wave superconductors. *Physical Review Letters*, 86(2):268, 2001.

[7] S. D. Sarma, C. Nayak, and S. Tewari. Proposal to stabilize and detect half-quantum vortices in strontium ruthenate thin films: Non-Abelian braiding statistics of vortices in a $p_x + ip_y$ superconductor. *Physical Review B*, 73(22):220502, 2006.

[8] C. Nayak, S. H. Simon, A. Stern, M. Freedman, and S. D. Sarma. Non-Abelian anyons and topological quantum computation. *Reviews of Modern Physics*, 80(3):1083, 2008.

[9] A. P. Mackenzie, T. Scaffidi, C. W. Hicks, and Y. Maeno. Even odder after twenty-three years: the superconducting order parameter puzzle of Sr_2RuO_4. *npj Quantum Materials*, 2(1):40, 2017.

[10] M. Anwar, T. Nakamura, S. Yonezawa, M. Yakabe, R. Ishiguro, H. Takayanagi, and Y. Maeno. Anomalous switching in Nb/Ru/Sr_2RuO_4 topological junctions by chiral domain wall motion. *Scientific Reports*, 3:2480, 2013.

[11] F. Kidwingira, J. Strand, D. Van Harlingen, and Y. Maeno. Dynamical superconducting order parameter domains in Sr_2RuO_4. *Science*, 314(5803):1267–1271, 2006.

[12] Y. Maeno, T. Ando, Y. Mori, E. Ohmichi, S. Ikeda, S. NishiZaki, and S. Nakatsuji. Enhancement of superconductivity of Sr_2RuO_4 to 3 K by embedded metallic microdomains. *Physical Review Letters*, 81(17):3765, 1998.

[13] S. Kittaka, H. Yaguchi, and Y. Maeno. Large enhancement of 3-K phase superconductivity in the Sr_2RuO_4–Ru eutectic system by uniaxial pressure. *Journal of the Physical Society of Japan*, 78(10):103705, 2009.

[14] M. Anwar, R. Ishiguro, T. Nakamura, M. Yakabe, S. Yonezawa, H. Takayanagi, and Y. Maeno. Multicomponent order parameter superconductivity of Sr_2RuO_4 revealed by topological junctions. *Physical Review B*, 95(22):224509, 2017.

[15] A. Steppke, L. Zhao, M. E. Barber, T. Scaffidi, F. Jerzembeck, H. Rosner, A. S. Gibbs, Y. Maeno, S. H. Simon, A. P. Mackenzie, et al. Strong peak in T_c of Sr_2RuO_4 under uniaxial pressure. *Science*, 355(6321):eaaf9398, 2017.

[16] A. Bouhon and M. Sigrist. Influence of the domain walls on the Josephson effect in Sr_2RuO_4. *New Journal of Physics*, 12(4):043031, 2010.

[17] M. Sigrist and D. F. Agterberg. The role of domain walls on the vortex creep dynamics in unconventional superconductors. *Progress of Theoretical Physics*, 102(5):965–981, 1999.

[18] V. F. Becerra and M. Milošević. Multichiral ground states in mesoscopic p-wave superconductors. *Physical Review B*, 94(18):184517, 2016.

[19] Y. Yasui, K. Lahabi, M. S. Anwar, S. Yonezawa, T. Terashima, J. Aarts, and Y. Maeno. Half-quantum fluxoid features in the magnetotransport of Sr_2RuO_4 micro rings. *Bulletin of the American Physical Society*, 2018.

[20] Z. Mao, Y. Maenoab, and H. Fukazawa. Crystal growth of Sr_2RuO_4. *Materials Research Bulletin*, 35(11):1813–1824, 2000.

[21] X. Cai, Y. Ying, N. Staley, Y. Xin, D. Fobes, T. Liu, Z. Mao, and Y. Liu. Unconventional quantum oscillations in mesoscopic rings of spin-triplet superconductor Sr_2RuO_4. *Physical Review B*, 87(8):081104, 2013.

[22] X. Cai, Y. Ying, J. Ortmann, W.-F. Sun, Z.-Q. Mao, and Y. Liu. Magnetoresistance oscillations and the half-flux-quantum state in spin-triplet superconductor Sr_2RuO_4. *arXiv preprint arXiv:1507.00326*, 2015.

[23] W. Little and R. Parks. Observation of quantum periodicity in the transition temperature of a superconducting cylinder. *Physical Review Letters*, 9(1):9, 1962.

[24] V. Moshchalkov, L. Gielen, C. Strunk, R. Jonckheere, X. Qiu, C. Van Haesendonck, and Y. Bruynseraede. Effect of sample topology on the critical fields of mesoscopic superconductors. *Nature*, 373(6512):319, 1995.

[25] E. Goldobin, D. Koelle, R. Kleiner, and A. Buzdin. Josephson junctions with second harmonic in the current-phase relation: Properties of φ junctions. *Physical Review B*, 76(22):224523, 2007.

[26] H. Sickinger, A. Lipman, M. Weides, R. Mints, H. Kohlstedt, D. Koelle, R. Kleiner, and E. Goldobin. Experimental evidence of a φ Josephson junction. *Physical Review Letters*, 109(10):107002, 2012.

[27] S. Michotte, D. Lucot, and D. Mailly. Fluxoid quantization in the critical current of a niobium superconducting loop far below the critical temperature. *Physical Review B*, 81(10):100503, 2010.

[28] G. Berdiyorov, M. Milošević, M. Latimer, Z. Xiao, W. Kwok, and F. Peeters. Large magnetoresistance oscillations in mesoscopic superconductors due to current-excited moving vortices. *Physical Review Letters*, 109(5):057004, 2012.

[29] I. Sochnikov, A. Shaulov, Y. Yeshurun, G. Logvenov, and I. Božović. Large oscillations of the magnetoresistance in nanopatterned high-temperature superconducting films. *Nature Nanotechnology*, 5(7):516, 2010.

[30] H. Fink, V. Grünfeld, and A. López. Quantum-interference device without Josephson junctions. *Physical Review B*, 35(1):35, 1987.

[31] A. A. Golubov, M. Y. Kupriyanov, and E. Il'ichev. The current-phase relation in Josephson junctions. *Reviews of Modern Physics*, 76(2):411, 2004.

[32] A. Troeman, S. van der Ploeg, E. Il'ichev, H.-G. Meyer, A. A. Golubov, M. Y. Kupriyanov, and H. Hilgenkamp. Temperature dependence measurements of the supercurrent-phase relationship in niobium nanobridges. *Physical Review B*, 77(2):024509, 2008.

[33] A. Sivakov, A. Pokhila, A. Glukhov, S. Kuplevakhsky, and A. Omelyanchouk. Oscillations of critical superconducting current in thin doubly-connected Sn films in an external perpendicular magnetic field. *Low Temperature Physics*, 40(5):408–417, 2014.

[34] D. Hazra, L. M. Pascal, H. Courtois, and A. K. Gupta. Hysteresis in superconducting short weak links and μ-SQUIDs. *Physical Review B*, 82(18):184530, 2010.

[35] N. Kumar, T. Fournier, H. Courtois, C. Winkelmann, and A. K. Gupta. Reversibility of superconducting Nb weak links driven by the proximity effect in a quantum interference device. *Physical Review Letters*, 114(15):157003, 2015.

[36] A. Sivakov, A. Glukhov, A. Omelyanchouk, Y. Koval, P. Müller, and A. Ustinov. Josephson behavior of phase-slip lines in wide superconducting strips. *Physical Review Letters*, 91(26):267001, 2003.

[37] O. J. Sharon, A. Shaulov, J. Berger, A. Sharoni, and Y. Yeshurun. Current-induced SQUID behavior of superconducting Nb nano-rings. *Scientific Reports*, 6:28320, 2016.

[38] D. G. Ferguson and P. M. Goldbart. Penetration of nonintegral magnetic flux through a domain-wall bend in time-reversal symmetry broken superconductors. *Physical Review B*, 84(1):014523, 2011.

[39] K. Ishida, H. Mukuda, Y. Kitaoka, K. Asayama, Z. Mao, Y. Mori, and Y. Maeno. Spin-triplet superconductivity in Sr_2RuO_4 identified by ^{17}O Knight shift. *Nature*, 396(6712):658, 1998.

[40] J. Duffy, S. Hayden, Y. Maeno, Z. Mao, J. Kulda, and G. McIntyre. Polarized-neutron scattering study of the Cooper-pair moment in Sr_2RuO_4. *Physical Review Letters*, 85(25):5412, 2000.

[41] J. Jang, D. Ferguson, V. Vakaryuk, R. Budakian, S. Chung, P. Goldbart, and Y. Maeno. Observation of half-height magnetization steps in Sr_2RuO_4. *Science*, 331(6014):186–188, 2011.

SUMMARY

This thesis explores the phenomenon of triplet superconductivity, which refers to a condensate of equal-spin Cooper pairs (pairs of electrons with equal spin). While exceptionally rare in nature, triplet pairing of electrons can occur if either the temporal or spatial component of the superconducting wavefunction can be represented by an odd function. These are often referred to as odd-frequency and odd-parity triplets, respectively. We use hybrid magnetic devices to study the former, while the latter is investigated in mesoscopic structures of strontium ruthenate (Sr_2RuO_4).

TRIPLET CORRELATIONS IN MAGNETIC HYBRIDS

While odd-frequency (even parity) triplet superconductivity has not yet been found by itself in nature, long-range triplet correlations can be generated in carefully engineered superconductor-ferromagnet hybrids. These spin-polarized Cooper pairs have become the centrepiece of the newly emerging field of *superconducting spintronics*, a new generation of technology that consumes little power and dissipates little heat, with applications in a wide range of subjects including state-of-the-art sensors, superconducting logic circuits, quantum computing and non-volatile cryogenic memories. Usually the focus is on the spin-polarization of the triplets, which can potentially enable low-dissipation magnetization switching. However, the fundamental mechanism for generating triplet correlations can also provide an exceptional level of control over superconductivity. We demonstrate this by combining state-of-the-art micromagnetic simulations with transport experiments in mesoscopic devices. In Chapter 4 we describe how to design and fabricate Josephson junctions in which the pathway of spin-triplet supercurrents through the junction can be controlled. This is demonstrated using a disk-shaped Josephson junction, where the barrier is a cobalt layer which contains a magnetic vortex with a core in the centre. We show how the supercurrent pathways can be regulated by moving the vortex with an applied magnetic field.

Generating long-range triplet correlations in a ferromagnet requires some form of magnetic inhomogeneity at the interface with a superconductor; and so far this has been realised with the use of multiple (at least two) ferromagnetic layers which have non-collinear magnetization. In Chapter 4 this was done with nickel contacts on top of the cobalt layer. Controlling the magnetization of individual layers however is a highly challenging task. A simpler method would be to use the spin texture of a

single ferromagnet to realise the necessary magnetic inhomogeneity for generating triplets. This type of device, which we call the spin-textured Josephson junction, is described in Chapter 5, where we demonstrate how the triplet currents can be generated by the in-plane exchange field gradient of a ferromagnetic vortex in a cobalt disk. The devices show a remarkable capacity to control the phase, amplitude and spatial distribution of triplet supercurrent in a dynamic fashion.

The spin-textured junctions also have a promising potential as non-volatile superconducting memory elements. In this case, the maximum supercurrent which our junctions can sustain before leaving the zero-resistance state (also known as the critical current of the junction) depends on the configuration of the transport channels, which is determined by the position of the ferromagnetic vortex or vortices in the cobalt disk. In the absence of magnetic fields, there are a number of stable magnetic states in which the system can be prepared, each yielding a different value for the critical current (ranging from maximum to zero). We can therefore consider the value of zero-field critical current as a "bit", which the junction can store (e.g. 0 for minimum critical current and 1 for maximum). While it is necessary for the device to be in the superconducting state to access (or "read") the bit, the information is not lost when the system is warmed up to room temperature for extended periods of time.

ODD-PARITY IN Sr_2RuO_4

Sr_2RuO_4 is one the handful materials known to exhibit odd-parity triplet superconductivity. In this particular case the superconducting wavefunction is expected to have a non-zero orbital angular momentum ($L = \pm 1$), which can be thought of as the electrons of the Cooper pair having a relative orbital motion, rotating either clockwise or anticlockwise. This orbital motion results in a handedness or "chirality", where the two winding directions (left or right) constitute a twofold degenerate ground state for the superconducting condensate. An interesting consequence of this would be the emergence of chiral superconducting domains in the bulk Sr_2RuO_4 crystal, where the chiral states are segregated in space. Despite the efforts of the past two decades, a direct observation of such chiral domains is still lacking. In Chapter 7 we present a new approach to this, using transport experiments on high-quality mesoscopic structures of Sr_2RuO_4, where the domain configuration could be controlled by well-defined geometries, as shown by the theoretical simulations of the order parameter. In particular, we focus on the boundary between adjacent domains (the chiral domain wall), which acts as an unconventional Josephson junction due to the local suppression of the condensate. Chapter 7 examines this, using a mesoscopic ring prepared by structuring a single Sr_2RuO_4 crystal. Order parameter simulations predict this system to a have multi-domain ground state, with a domain wall crossing the arms of the ring, where it forms a pair of parallel Josephson junctions.

This is examined by our transport experiments, where we find distinct critical current oscillations when applying an axial magnetic field, similar to that of a DC SQUID with two symmetric Josephson junction.

One of the most fascinating aspects of a chiral domain wall junction is its Josephson energy profile as function of the phase difference of the condensate on both sides of the junction. Contrary to conventional junctions, the Josephson potential of a chiral domain wall has *two* minima with different energies as function of the phase difference φ , resulting in one stable (φ_0) and one metastable (φ') Josephson phase. Here φ_0 and φ' are determined by the orientation of the domain wall, and can take on *any* values between 0 and π. We describe how this multi-minima Josephson potential would manifest itself as a multistage current-voltage characteristic, similar to the ones in our transport measurements.

In addition to making a compelling case for the existence of chiral domains in Sr_2RuO_4, this study presents a new outlook on the potential use of chiral domain walls as Josephson junctions with adjustable ground state energy. The current across a Josephson junction is driven by the phase difference between the leads, mentioned above. Usually, the ground state of a junction has a phase of 0 or π, both of which correspond to zero transport across the junction. In a chiral domain wall however, the ground state of the junction can be offset by a phase that is different from zero or π. This provides the conditions for an anomalous supercurrent to flow from one lead to another (at zero bias), which would make this one of the very few cases where both time-reversal and chiral symmetries are broken. In addition to the promise of rich physics, such systems are highly desirable for their potential as superconducting phase batteries, rectifiers, and future applications in quantum computing.

SAMENVATTING

Dit proefschrift heeft als onderwerp triplet supergeleiding, waarmee een condensaat van Cooperparen bedoeld wordt dat bestaat uit elektronen met gelijk-gerichte spins. De supergeleidende golffunctie van een triplet is zodanig dat of het tijdsafhankelijke deel of het plaatsafhankelijk deel wordt gerepresenteerd door een oneven functie. Deze soorten triplet supergeleiding worden respectievelijk 'odd-frequency' en 'odd-parity' triplets genoemd. Wij gebruiken hybride magnetische structuren om de eerste type triplets te onderzoeken, en mesoscopische structuren gefabriceerd van het materiaal strontium ruthenaat (Sr_2RuO_4) om het tweede type te bestuderen.

TRIPLET CORRELATIES IN MAGNETISCHE HYBRIDES

Hoewel odd-frequency (even pariteit) triplet supergeleiding tot nu toe niet in de natuur is waargenomen, is het wel mogelijk om tripletcorrelaties met een grote correlatielengte te genereren in zorgvuldig ontworpen supergeleider-ferromagneet hybriden. Deze spin-gepolariseerde Cooperparen staan centraal in het nieuwe gebied van de *supergeleidende spintronica*. Dit gebied houdt de belofte in van een nieuwe generatie technologie gekarakteriseerd door een laag energieverbruik en laag warmteverlies, met toepassingen zoals state-of-the-art sensoren, supergeleidende circuits, kwantum computing en niet-vluchtig cryogeen geheugen. Normaliter ligt de focus daarbij op het spin-gepolariseerde karakter van de triplets, dat mogelijk kan worden gebruikt voor het met lage dissipatie schakelen van magnetisatie. Het fundamentele mechanisme voor het genereren van triplet-correlaties levert echter ook een uitzonderlijk niveau van controle over de supergeleiding zelf. We tonen dit aan door het combineren van state-of-the-art micromagnetische simulaties en transportexperimenten in mesoscopische preparaten. In Hoofdstuk 4 beschrijven we hoe zulke micromagnetische simulaties kunnen worden gebruikt om Josephson juncties te ontwerpen waarin het pad van de spin-triplet superstroom door de junctie beïnvloed kan worden. We gebruiken hiervoor een schijfvormige Josephson-junctie met een dunne kobalt laag als barrière. Deze schijfvormige laag bevat een magnetische vortex, met een kern in het midden. We tonen aan hoe de superstroomkanalen gecontroleerd kunnen worden door het verplaatsen van de vortex met het aanbrengen van een magnetisch veld.

Het injecteren van lange-afstand tripletcorrelaties in een ferromagneet vereist een bepaalde mate van magnetische inhomogeniteit aan het grensvlak van supergeleider

en ferromagneet. Tot nu toe werd dit gerealiseerd door middel van meerdere (minstens twee) ferromagnetische lagen met niet-collineaire magnetisatie. In Hoofdstuk 4 zijn hiervoor nikkel contacten op de kobalt schijf gebruikt. Het beheersen van de magnetisatie van de individuele lagen is echter een stevige uitdaging. Eenvoudiger zou zijn om de spintextuur van een enkele ferromagneet te implementeren. Dit type structuur, dat we de spin-getextureerde Josephson junctie noemen, wordt beschreven in Hoofdstuk 5. In dit hooftstuk demonstreren we hoe tripletstromen worden gegenereerd door de exchangeveld gradienten van een ferromagnetische wervel in een kobalt schijf. Deze structuren laten dynamische controle toe van de fase, amplitude, en ruimtelijke distributie van triplet superstromen.

De spin-getextureerde juncties zijn ook veelbelovend als niet-vluchtige supergeleidende geheugenelementen. De maximale superstroom die onze juncties aankunnen voor ze weerstand vertonen (de kritische stroom van de junctie) hangt af van de configuratie van de transport kanalen en wordt bepaald door de positie van de ferromagnetische wervel of wervels in de kobalt schijf. Er is een aantal stabiele magnetische 'nul-veld' configuraties waarin het systeem kan worden gebracht en elke toestand heeft een eigen kritische stroom (variërend van maximaal tot nul). De waarde van deze nul-veld kritische stroom kan dus gezien worden als een "bit" die de junctie kan opslaan (bv. 0 voor de minimumwaarde van de kritische stroom en 1 voor het maximum). Hoewel de structuur supergeleidend is om het bit te "lezen", gaat de informatie niet verloren wanneer het systeem gedurende langere tijd tot kamertemperatuur wordt opgewarmd.

'ODD-PARITY' IN Sr_2RuO_4

Sr_2RuO_4 is een van de weinige materialen die 'oneven-pariteit' triplet supergeleiding vertoont. In het specifieke geval van strontium ruthenaat is de verwachting dat de supergeleidende golffunctie een eindig baanimpulsmoment heeft. Dit kan worden beschouwd als een relatieve baanbeweging van de twee elektronen in een Cooperpaar, met de klok mee dan wel tegen de klok in. Het onderscheid tussen de draairichtingen wordt 'chiraliteit' genoemd, waarbij de chiraliteiten corresponderen met twee ontaarde grondtoestanden (grondtoestanden met gelijke energie). Een interessante consequentie hiervan is het bestaan van zogeheten supergeleidende chirale domeinen in bulk Sr_2RuO_4 kristallen, die van elkaar gescheiden zijn door domeinwanden. Ondanks het experimentele werk van de laatste twee decennia, zijn deze domeinwanden nog nooit waargenomen. In Hoofdstuk 7 presenteren we een nieuwe experimentele aanpak waarbij gebruik gemaakt wordt van hoge-kwaliteit mesoscopische structuren van strontium ruthenaat. In deze structuren kan de domeinconfiguratie op een goed gecontroleerde manier gemaakt worden, zoals blijkt uit theoretische simulaties van de supergeleidende ordeparameter. In het bijzonder richten we ons op de domeinwand tussen twee naburige domeinen,

die gedrag vertoont van een onconventionele Josephson-junctie door de lokale onderdrukking van het supergeleidende condensaat. Het type structuren dat gebruikt wordt in Hoofdstuk 7 zijn mesoscopische ringen gefabriceerd uit een enkel Sr_2RuO_4 kristal. Simulaties van de ordeparameter in de ring voorspellen een grondtoestand met meerdere domeinen, waarbij een domeinwand gevonden kan worden in beide armen van de ring. Hierdoor ontstaan Josephson-juncties op de locaties van de domeinwanden. Door het bestuderen van dit systeem met behulp van transportmetingen, vinden we kritische stroom-oscillaties vergelijkbaar met die van een DC SQUID (een 'Superconducting Quantum Interference Device') met twee symmetrische Josephson-juncties.

Een van de meer fascinerende aspecten van de chirale domeinwand-juncties is het gedrag van de Josephson-energie als functie van het faseverschil van het condensaat aan beide kanten van de junctie. In tegenstelling tot klassieke Josephson-juncties vertoont de Josephson-energie als functie van het faseverschil φ: van een chirale domeinwand-junctie *twee* ongelijke minima: één daarvan is een globaal minimum en daarmee stabiel (φ_0), terwijl het andere metastabiel is (φ'). Hierbij worden φ_0 en φ' bepaald door de oriëntatie van de domeinwand ten opzichte van de stroomrichting en kunnen ze waardes aannemen variërend van 0 tot π. We beschrijven hoe deze Josephson energie met twee minima zich manifesteert in een stroom-spannings karakteristiek met meerdere spannings-stappen, zoals wij vinden in onze transportmetingen.

Naast het leveren van overtuigend bewijs voor het bestaan van chirale domeinwanden in Sr_2RuO_4, presenteren we een nieuw vooruitzicht op het gebruik van chirale domeinwanden als Josephson-juncties met aanpasbare grondtoestandsenergie. De stroom die door de Josephson-junctie loopt wordt gedreven door het het eerder genoemde faseverschil tussen de contacten. In klassieke Josephson-juncties is dit faseverschil intrinsiek 0 of π (beide resulteren in afwezigheid van stroom door de junctie). In het geval van de chirale domeinwand is het faseverschil echter een arbitraire waarde tussen 0 en π. Hierdoor kan er een superstroom door de junctie lopen zonder dat er een spanningsverschil is aangelegd. Dit maakt dit een van de weinige bekende gevallen waarin zowel tijdomkeer-symmetrie als chirale symmetrie gebroken is. Naast een belofte voor interessante fysica in deze systemen, bieden ze mogelijke toepassingen voor kwantumcomputers en als fasebatterij of gelijkrichter.

ACKNOWLEDGEMENTS

As I write this I cannot help feeling exceptionally fortunate for having had the pleasure of working with so many wonderful individuals throughout my PhD. I would like to begin by thanking my promoter, Jan Aarts, for giving me the opportunity to join his research and grow as a scientist. In particular, I am grateful for his continuous support and guidance, for his knowledge and experience, which he shared with great humility and patience, for many stimulating discussions, which are some of the most enjoyable highlights of my PhD, and finally for his gracious nature which prevailed even in the most stringent of circumstances. I would also like to express my deepest gratitude to the guidance I received from Dr. Paul Alkemade from the Kavli Nanolab (Delft), for his support, valuable suggestions and encouragement throughout the years. By sharing his skills and expertise on focused ion beams, I was able to apply this elegant technique as the foundation of the various devices used in my research.

In the early stages of my PhD I had the great fortune of learning from some of my former colleagues. Amongst these, I am truly thankful to Amrita Singh, with whom I worked on the CrO_2 devices, to Stefano Voltan, who never hesitated to offer his assistance, to Gaurav Nanda for the encouragements and sharing his knowledge of focused ion beams, and to Daan Boltje for his continuous support and friendship throughout the years. I am also grateful to my former undergraduate students (in chronological order) Peter Sterk, Ewout Beukers, Menno Pleijster, Louis Maduro, Brin Verheijden, Willem Tromp, Remko Fermin and Michel Hubert, who made substantial contributions to my research. To say that they taught me more than I could teach them would not be an overstatement.

I am also thankful to Marcel Hesselberth for the technical support and valuable insights, to Federica Galli for providing assistance with the vector magnet and first-class humour during coffee, and to Douwe Scholma and Thomas Mechielsen for ensuring the smooth running of the lab. I also want to mention Christiaan Pen and Ruud van Egmond, from the FMD, for their prompt and effective solutions, and Peter van Veldhuizen, from the ELD, for his assistance with the electronics. I would like to thank Hozanna Miro for her continuous support with the dual-beam in Delft. Special thanks to Daniëlle Duijn and Ellie van Rijsewijk, who played an invaluable role in my PhD by their effective handling of administrative issues, while being exceptionally patient and understanding.

My gratitude goes to Srijit Goswami for kindly taking the time to discuss my results and sharing his valuable insights on Josephson junctions and SQUIDs, to Johannes Jobst for his helpful suggestions and useful feedback, and to Aymen Ben Hamida, for his continuous assistance and exchange of ideas. My PhD could not have been a rich experience without the simulating conversations with Milan Allan, Tjerk Oosterkamp, Jan van Ruitenbeek and Sense Jan van der Molen, for which I am truly grateful. I am also thankful to Eric Eliel for his time and constructive feedback.

I would like to acknowledge Jacob Linder, Morten Amundsen and my good friend Ali Ouassou from Trondheim, for their theoretical contribution to the multilayer disk junctions. Their prompt and pragmatic approach to problems was highly refreshing, and I thoroughly enjoyed our collaboration.

During my PhD I was fortunate enough to have a long-lasting and fruitful collaboration with Yoshi Maeno's group at Kyoto University, with whom I share the credits for the work on Sr_2RuO_4. In particular, I am thankful to Yuuki Yasui for his hard work and many thought-provoking discussions, Shahbaz Anwar and Shingo Yonezawa for sharing their valuable insights and Yuji Nakamura for his efforts during the early stages of the project. My sincere gratitude goes to Yoshi Maeno for his continuous support and helpful discussions throughout our collaboration. I am humbled by the warm hospitality I received during my visits to Japan. Furthermore, I would like to thank my collaborators in Antwerp, Milorad Milošević and Victor Fernández Becerra, for their theoretical input and insightful conversations about the chiral order parameter.

The Leiden institute, LION, has been an inspiring and pleasant work environment, and I have many people to thank for that, especially Nikita Lebedev, Irene Battisti, Gesa Welker, Chunhai Yin, Kumar Prateek, Chris Smiet, Sasha Vrbica and Daniël Geelen. I would also like to acknowledge the Van der Zalm family, who never failed to brighten up my day.

Lastly, I would like to thank my family who made great many sacrifices just to provide me with the opportunity to pursue a career in science. I am particularly grateful to Bijan Keshmiri, whose support played a crucial role in the continuation of my studies.

LIST OF PUBLICATIONS

- A. Singh, S. Voltan, **K. Lahabi** and J. Aarts. Colossal proximity effect in a superconducting triplet spin valve based on the half-metallic ferromagnet CrO_2, *Physical Review X*, **5**(2), 021019, 2015.
- S. Voltan, C. Cirillo, H. J. Snijders, **K. Lahabi**, A. García-Santiago, J. M. Hernández, C. Attanasio and J. Aarts. Emergence of the stripe-domain phase in patterned permalloy films, *Physical Review B*, **94**(9), 094406, 2016.
- A. Singh, C. Jansen, **K. Lahabi** and J. Aarts. High-quality CrO_2 nanowires for dissipation-less spintronics, *Physical Review X*, **6**(4), 041012, 2016.
- Y. Yasui, **K. Lahabi**, M. S. Anwar, Y. Nakamura, S. Yonezawa, T. Terashima, J. Aarts, and Y. Maeno. Little-Parks oscillations with half-quantum fluxoid features in Sr_2RuO_4 micro rings, *Physical Review B*, **96**(18), 180507, 2017.
- **K. Lahabi**, M. Amundsen, J. A. Ouassou, E. Beukers, M. Pleijster, J. Linder, P. Alkemade and J. Aarts . Controlling supercurrents and their spatial distribution in ferromagnets, *Nature Communications*, **8**(1), 2056, 2017.
- Y. Yasui*, **K. Lahabi***, V. F. Becerra, M. S. Anwar, S. Yonezawa, T. Terashima, M. V. Milošević, J. Aarts and Y. Maeno. Spontaneous emergence of Josephson junctions in homogeneous rings of single-crystal Sr_2RuO_4, *under review*, 2018.
- **K. Lahabi**, R. Fermin, M. Hubert, A. B. Hamida and J. Aarts. Generating spin-triplet supercurrents with a ferromagnetic vortex, *to be submitted*.
- A. Singh*, **K. Lahabi***, L. Maduro and J. Aarts. Controlling spin-triplet supercurrent with domain-walls in a CrO_2 nanowire, *to be submitted*.
- **K. Lahabi**, Y. Yasui, V. F. Becerra, M. S. Anwar, S. Yonezawa, M. V. Milošević, J. Aarts and Y. Maeno. Signatures of an asymmetric Josephson potential in chiral domain wall junctions, *to be submitted*.
- **K. Lahabi** and J. Aarts. Spin-textured Josephson junctions, *Patent application pending*.

* These authors contributed equally.

Curriculum Vitae

I was born in September 1987 in Iran. In January 2004 I moved to England to continue my studies. Upon completing my A-levels at Lincoln Christ Hospital School, Lincoln, I was granted admission to Bristol University in the fall of 2006. In the third year of my undergraduate degree I was offered a full-time internship at MHS electronics, Swindon, to investigate the dynamics of photoresist on a rotating silicon wafer. For my final year Bachelor's project I worked on localised electromagnetic modes in photonic crystal cavities. I graduated from Bristol in 2010 with an upper-second class Bachelor of Science (honours) in Physics with Industrial Experience.

In 2011 I was awarded the full Science at Leuven Scholarship from KU Leuven, Belgium, where I studied Master of Physics. My Master's project was on the interplay between ferromagnetism and superconductivity in epitaxially grown multilayers. I graduated magna cum laude in 2013. Soon after, I started my PhD under the supervision of Prof. Jan Aarts (Leiden) and Dr. Paul Alkemade (TU Delft).